DOPPLER-FREE OPTICAL-OPTICAL DOUBLE RESONANCE POLARIZATION SPECTROSCOPY ON THE STRUCTURE AND DYNAMICS OF ALKALI METAL DIATOMIC MOLECULES

笠原, 俊二

(Degree)
博士（理学）

(Date of Degree)
1993-03-31

(Date of Publication)
2007-09-26

(Resource Type)
doctoral thesis

(Report Number)
甲1211

(JaLCDOI)
https://doi.org/10.11501/3092491

(URL)
https://hdl.handle.net/20.500.14094/D1001211

博　士　論　文

DOPPLER-FREE OPTICAL-OPTICAL DOUBLE RESONANCE POLARIZATION SPECTROSCOPY ON THE STRUCTURE AND DYNAMICS OF ALKALI METAL DIATOMIC MOLECULES

（ドプラーフリー光・光二重共鳴偏光分光法による
アルカリ金属二原子分子の構造とダイナミックスに関する研究）

平　成　5　年　　3　月

神戸大学大学院自然科学研究科

笠　原　　俊　二

TABLE OF CONTENTS

LIST OF TABLES

LIST OF FIGURES

Chapter 1. INTRODUCTION

Spectroscopy is very useful to study the molecular structure and dynamics. In recent years the investigation and development of lasers changed conventional spectroscopy. The high intensity and high spectral resolution of lasers have opened a new class of spectroscopic techniques which allow investigation of the structure of atoms and molecules in much more detail. Information on the molecular structure and on the interaction of molecules with their surrounds can be derived in various ways from the absorption and emission spectra generated when electromagnetic radiation interacts with matter.[1]

Wavelength measurements of spectral lines allow the determination of energy levels of the molecular system. The intensity is proportional to the transition probability which measures how strongly the two levels of a molecular transition are coupled. Since the transition probability depends on the wave functions of both levels, intensity measurements are useful to verify the spatial charge distribution of excited electrons. The natural linewidth of a spectral line, which can be resolved by special techniques, allows mean lifetimes of excited molecular states to be determined. Measurements of the Doppler width yield the velocity distribution of the emitting or absorbing molecules and with it the temperature of the sample. From pressure broadening and pressure shifts of spectral lines, information about collision processes and interatomic potentials can be extracted. The hyperfine structure of spectral lines yields information about the interaction between the nuclei and the electron cloud and

allows nuclear magnetic dipole moments or electric quadrapole moments to be determined.

These examples represent only a small selection of the many possible ways by which spectroscopy provides tools to explore the microworld of atoms and molecules. The amount of information which can be extracted from spectrum depends essentially on the attainable spectral resolution and on the detection sensitivity that can be achieved.

The spectral resolution was in principle limited by the Doppler width of lines in the conventional absorption and emission spectra, although the laser linewidth might have been much smaller. The Doppler-free techniques allow fully to resolve the spectrum. The basic principle of most Doppler-free techniques relies on a proper selection of a subgroup of molecules with velocity components v_z in the direction of the incident monochromatic wave, which fall into a small interval Δv_z around $v_z=0$. This selection can be achieved either by mechanical apertures which select a collimated molecular beam, or selective saturation within the velocity distribution of absorbing molecules caused by strong pump, and a successive probing of this selective "hole burning" by a monochromatic tunable probe wave. However, even if all lines completely resolved by using the Doppler-free spectroscopic techniques, the unambiguous assignment of a large number of lines in a band system with overlapping bands may be greatly impeded when the level density is high or the perturbations cause irregular shifts of the line positions. In such cases an optical-optical double resonance (OODR) techniques provides powerful ways to study the excited molecules. These techniques yield

simplified spectra, since only transitions can be detected which start either from a selected lower (v", J") level or an upper (v', J') level labeled by a known pump transition (v', J') ← (v", J").

We have used the technique of the Doppler-free OODR polarization spectroscopy to study excited states of Alkali metal diatomic molecules. Alkali metal diatomic molecules have allowed electronic transitions in visible region, and the dissociated atoms have the radiative transition (such as the D_1 and D_2 lines) also in the visible region. Hence, alkali metal diatomic molecules are appropriate to study excited states, perturbation, and the dissociation dynamics.

The energy levels and wave function of a rotating diatomic molecule may be worked out by diagonalizing the energy matrices. The angular momentum are defined as follows:

L — total electronic orbital angular momentum

S — total electronic spin angular momentum

J — total angular momentum (**J=R+L+S**)

N — total angular momentum excluding electronic spin (**N=J-S**)

R — rotational angular momentum.

The total electronic orbital and total electronic spin angular momentum **L** and **S** makes the projections Λ and Σ along the internuclear axis (z), respectively. The total angular momentum **J** makes the projection M along the laboratory-fixed Z axis and the projection $\Omega=\Lambda+\Sigma$ along the internuclear axis (z). In Hund's coupling case (a) and (b), the molecular electronic state can be represented by $^{2S+1}\Lambda_{\Omega}$. In the case (a), the **L** and **S** are strong-

ly coupled to the internuclear axis, and in the case (b), the **S** is weakly coupled (or uncoupled) to the internuclear axis. In this representation, according as $\Lambda = 0, 1, 2, 3, \cdots$, the corresponding molecular state is designated a Σ, Π, Δ, Φ, $\cdots$, state.

The basis functions for a rotating diatomic molecules may be written as a product of an electronic orbital part $|\Lambda\rangle$, an electronic spin part $|S\Sigma\rangle$, a vibrational part $|v\rangle$, and a rotational part $|J\Omega M\rangle$:

$$|\Lambda\rangle|S\Sigma\rangle|v\rangle|J\Omega M\rangle, \tag{1.1}$$

The Hamiltonian for a rotating diatomic molecule in the absence of an external field can be written as

$$H = H_e + H_v + H_r, \tag{1.2}$$

where H_e is the electronic part, H_v is the vibrational part, and H_r is the rotational part. The rotational level energies and wave function of the diatomic molecules can be obtained by solving the secular equation composed of the matrices for a H in terms of the basis set $|\Lambda\rangle|S\Sigma\rangle|v\rangle|J\Omega M\rangle$.

The term energy $E_{v,J}$ (in cm^{-1}) for a singlet state (S=0) of the diatomic molecule is simply expressed as

$$E_{v,J} = E_v^o + B_v[J(J+1) - \Lambda^2] - D_v[J(J+1) - \Lambda^2]^2 + H_v[J(J+1) - \Lambda^2]^3 + \cdots, \tag{1.3}$$

where Λ is 0 for a $^1\Sigma^+$ state, ±1 for a $^1\Pi$ state, ±2 for a $^1\Delta$ state, $\cdots$; B_v is the rotational constant, D_v is the centrifugal distortion constant, and E_v^o is the energy of the vibrational state v:

$$E_v^o = T_e + G_v, \tag{1.4}$$

where T_e is the minimum energy of the corresponding potential energy curve, and G_v is the vibrational energy. By using Eq.

(1.3), the molecular constants can be determined from observed spectral lines.

In chapter 3, from the V-type OODR polarization spectrum, the determination of the molecular constants and the RKR potential energy curve of the NaK $B^1\Pi$ state will be discussed. Remarkable line broadening were observed for transitions to $B^1\Pi(v', J')$ level higher than the dissociation energy to $Na(3s^2S_{1/2}) + K(4p^2P_{1/2})$ atoms. This is identified as originating from the predissociation, and the mechanism will be studied. From the 2-step OODR polarization spectrum, several $^1\Sigma^+$, $^1\Pi$, and $^1\Delta$ states of the NaK molecule were observed in the energy regions 33016~33674 cm^{-1} and 34449~34717 cm^{-1}. The assignments and the determination of the molecular constants of these highly excited states will be discussed in chapter 4.

In chapter 5, the molecular constants and the RKR potential curve of the $D^1\Sigma_u^+$ state of the Cs_2 molecule will be reported. The V-type OODR polarization spectroscopy was used in order to confirm the assignment. The perturbation and predissociation of the $D^1\Sigma_u^+$ state was found. The predissociation of the $D^1\Sigma_u^+$ state will be studied from the Cs_2 molecular beam experiment by monitoring separately the molecular fluorescence and the D_2 or D_1 atomic emission.

Chapter 2. SPECTROSCOPIC METHOD

2.1 Doppler-free Polarization Spectroscopy

In this section a brief summary of the Doppler-free polarization spectroscopy is described. A more detail description of this technique and its theoretical background can be found in Ref. 1~5. The output of a single mode dye laser is split into a weak, linearly polarized probe beam and a stronger pump beam which can be either circularly or linearly polarized. Both beams travel in opposite directions through the sample cell placed between two crossed polarizers. Assume the laser is tuned to a transition (v', J') ← (v", J") between a level (v", J") in a ground state and a level (v', J') in a excited state. Each rotational level with angular momentum J consists of (2J+1) degenerate magnetic sublevels (J, M). If the pump beam is sufficiently strong to saturate the transition (v', J') ← (v", J"), the lower M" sublevels will be partly depleted while the population N(v', J', M') of the upper levels will be increased correspondingly. The degree of saturation depends on the transition probability A(J',M' ← J",M") which generally differs for different M values. This M-selective optical pumping process leads to a partial orientation of the sample molecules. The molecular gas, which had been isotropic without the pump, now becomes optically birefringent and dichroic. If the probe beam and the pump beam can be absorbed by the molecules which have same velocity component, the polarization of the probe beam passed through the sample cell is being altered from a linear to slightly elliptical polarization. Then, the transmission of the probe beam can

pass through the second polarizer, and a signal will be detected. The important point is that this signal shows a Doppler-free line profile, as can be seen from the following arguments:

When a monochromatic wave with frequency ω and wave vector $\mathbf{k}$ passes in +z direction through a gas of molecules with a thermal velocity distribution $N(v_z)$, the wave experiences absorption if ω lies within the frequency range of a Doppler-broadened absorption line centered at ω_0. However, out of all molecules in the absorbing level (v", J"), only a small subgroup with velocity components $v_z = (\omega-\omega_0)/k$ can absorb the wave because only those molecules are Doppler shifted into resonance with the laser wave. Since the pump wave and the probe wave travel into opposite direction, both waves will interact with different velocity subgroups around $v_z = +(\omega-\omega_0)/k$ or $v_z = -(\omega-\omega_0)/k$, respectively, as long as $\omega \neq \omega_0$, but with the same subgroup of molecules (with velocity components around $v_z=0$) if $\omega=\omega_0$.

A more detail analysis yields the results[1-5], that for a circularly polarized pump beam, the probe intensity $I(\omega)$ transmitted through the second polarizer can be written as

$$I(\omega) = I_0 \left[\xi + \theta^2 + b^2 - \frac{1}{2}\theta L\Delta\alpha \frac{\chi}{1+\chi^2} - \frac{1}{2} bL\Delta\alpha \frac{1}{1+\chi^2} + \left(\frac{1}{4} L\Delta\alpha\right)^2 \frac{1}{1+\chi^2} \right], \qquad (2.1)$$

where ξ is the extinction ratio of the completely crossed polarizers; θ is the uncrossing angle, i. e., the angular deviation from complete crossing; b is a constant term which takes into account the nonnegligible birefringence of the sample cell windows; L is the length of the absorption path; $\chi = (\omega-\omega_0)/\gamma$ is the

normalized frequency detuning, where γ is the homogeneous linewidth of the molecular transition; and $\Delta\alpha = \alpha^{+}(\omega_0)-\alpha^{-}(\omega_0)$ gives the change of the absorption coefficient at the line center ω_0 caused by the M-selective saturation, where $\alpha^{+}(\omega_0)$ and $\alpha^{-}(\omega_0)$ is the absorption coefficient of a right and a left circularly polarized component of the probe beam.

For a linearly polarized pump beam, of which polarization is chosen to be 45° against the probe polarization, the probe intensity transmitted through the second polarizer can be written as

$$I(\omega) = I_0 \left[\xi + \theta^2 + b^2 - \frac{1}{2}\theta L\delta\alpha \frac{1}{1+\chi^2} - \frac{1}{2} bL\delta\alpha \frac{\chi}{1+\chi^2} + \left(\frac{1}{4} L\delta\alpha\right)^2 \frac{1}{1+\chi^2}\right], \qquad (2.2)$$

where $\delta\alpha = \alpha^{z}(\omega_0)-\alpha^{x}(\omega_0)$ gives the change of the absorption coefficient at the line center ω_0, where $\alpha^{z}(\omega_0)$ and $\alpha^{x}(\omega_0)$ is the absorption coefficient of a parallel and a perpendicular linearly polarized component of the probe beam against to the polarization of the pump beam. In this situation, it is best to take the axis of quantization along the direction of the pump polarization. In Eq. (2.1) and (2.2), the first three terms represent background intensity, and the term of $\chi/(1+\chi^2)$ and $1/(1+\chi^2)$ represents, respectively, dispersion shaped signal and Lorentzian profile.

In order to estimate the relative intensity of the polarization signal, it is necessary to calculate the difference in absorption coefficient $\Delta\alpha$ and $\delta\alpha$ of the two components of the probe beam. Assume the pump transition $(J'=J_1) \leftarrow (J''=J)$ and the probe transition $(J'=J_2) \leftarrow (J''=J)$ share a common lower level (v",

J). For a circularly polarized pump beam, $\Delta\alpha$ is given by

$$\Delta\alpha = \Sigma_M n_M [\sigma^+(J_2,M_2 \leftarrow J,M) - \sigma^-(J_2,M_2 \leftarrow J,M)], \quad (2.3)$$

where $\sigma^+(J_2,M_2 \leftarrow J,M)$ and $\sigma^-(J_2,M_2 \leftarrow J,M)$ are, respectively, the absorption cross sections for a right and left circularly polarization, which are proportional to the squares of the transition dipole moment. n_M is the number density in the (J, M) level pumped by a right circularly polarized pump beam, and it is given by

$$n_M = \frac{N_0}{2J+1} \left(1 - \frac{I_{pp}}{S}\right), \quad (2.4)$$

where N^0 is the total equilibrium number density of the J level in the absence of the pump beam, I_{pp} is the intensity factor of the pump beam, and S is the saturation parameter of the cw laser;

$$S = \frac{\hbar\omega_1}{\sigma(J_1,M_1 \leftarrow J,M)} \left(\frac{1}{\gamma_0} + \frac{1}{\gamma_1}\right)^{-1}, \quad (2.5)$$

where γ_0 and γ_1 are the homogeneous widths of lower and upper levels, respectively.

From Eq.(2.3)~(2.5), $\Delta\alpha$ can be written as

$$\Delta\alpha = -\frac{1}{2} \alpha_0 \frac{I_{pp}}{S} \zeta^C(J_1 \leftarrow J, J_2 \leftarrow J). \quad (2.6)$$

Here $\alpha_0 = N_0\sigma(J_2 \leftarrow J)$ is the unsaturated absorption coefficient for the probe transition. The numerical factor ζ^C (subscript C represents for a circularly polarized pump beam), which is called polarization factor, can be calculated from a sum of the Clebsch-Gordan coefficients over all the M levels.

For a linearly polarized pump beam, $\delta\alpha$ is given by

$$\delta\alpha = \Sigma_M n_M [\sigma^z(J_2,M_2 \leftarrow J,M) - \sigma^x(J_2,M_2 \leftarrow J,M)], \quad (2.7)$$

where $\sigma^z(J_2,M_2 \leftarrow J,M)$ and $\sigma^x(J_2,M_2 \leftarrow J,M)$ are, respectively, the absorption cross sections for a parallel and a perpendicular to the pump polarization. Proceeding as before, the difference in absorption coefficients can be written as

$$\delta\alpha = -\frac{1}{2}\alpha_0 \frac{I_{pp}}{S} \zeta^L(J_1 \leftarrow J, J_2 \leftarrow J). \tag{2.8}$$

The factor ζ^L is the polarization factor for a linearly polarized pump beam. Under the assumption that γ_0 is much larger than γ_1, the calculated values of ζ^C and ζ^L are tabulated in Table I.

For the normal Doppler-free polarization signal, the both of pump and probe beam come from the same laser, we have only transition with $J_1=J_2$, which correspond to the diagonal elements of Table I. For large J values associated with molecules, the polarization factors ζ^C approach the limit 3/2 for $\Delta J=\pm 1$ and 0 for $\Delta J=0$, and the factors ζ^L approach 3/10 for $\Delta J=\pm 1$ and 6/5 for $\Delta J=0$. These results show that only P lines (for $\Delta J=-1$) and R lines (for $\Delta J=+1$) can be detected for a circularly polarized pump beam, and Q lines (for $\Delta J=0$) are strongly detected than P or R lines for a linearly polarized pump beam. It can be seen that Q lines can be clearly distinguish from P and R lines from the choice of pump polarization.

2.2 Doppler-free Optical-Optical Double Resonance Polarization Spectroscopy

In this section a brief summary of the Doppler-free OODR polarization spectroscopy,[4] which is application of OODR technique to polarization spectroscopy, is described. A more detail description of OODR techniques, often called three-level laser

Table I. The J dependence of the polarization factor $\zeta^{C,L}(J_1 \leftarrow J, J_2 \leftarrow J)$.

$\zeta^{C}(J_1 \leftarrow J, J_2 \leftarrow J)$ (circularly polarized pump)

	probe transition		
	R: $J_2=J+1$	Q: $J_2=J$	P: $J_2=J-1$
pump transition			
R: $J_1=J+1$	$\frac{3J}{2(J+1)}$	$-\frac{3}{2(J+1)}$	$-\frac{3}{2}$
Q: $J_1=J$	$-\frac{3}{2(J+1)}$	$\frac{3}{2J(J+1)}$	$\frac{3}{2J}$
P: $J_1=J-1$	$-\frac{3}{2}$	$\frac{3}{2J}$	$\frac{3(J+1)}{2J}$

$\zeta^{L}(J_1 \leftarrow J, J_2 \leftarrow J)$ (linearly polarized pump)

	probe transition		
	R: $J_2=J+1$	Q: $J_2=J$	P: $J_2=J-1$
pump transition			
P: $J_1=J+1$	$\frac{3J(2J-1)}{10(J+1)(2J+3)}$	$-\frac{3(2J-1)}{10(J+1)}$	$\frac{3}{10}$
Q: $J_1=J$	$-\frac{3(2J-1)}{10(J+1)}$	$\frac{3(2J+3)(2J-1)}{10J(J+1)}$	$-\frac{3(2J+3)}{10J}$
R: $J_1=J-1$	$\frac{3}{10}$	$-\frac{3(2J+3)}{10J}$	$\frac{3(J+1)(2J+3)}{10J(2J-1)}$

spectroscopy of coupled transitions can be found in Ref. 6-8.

This method uses two independent lasers. Assume laser 1, called the pump laser, is stabilized onto the center frequency of a transition $(v_1, J_1) \leftarrow (v, J)$. Due to selective M sublevel pumping, molecules in these levels with velocity components within a small interval $v_z = 0 \pm \gamma/k$ are partly oriented (see previous section). The linearly polarized beam of a second laser 2, called the probe laser, passes in the opposite direction through the sample cell. When the probe laser is tuned through the molecular absorption spectrum, the polarization is altered if the frequency of the probe laser coincides with a center of the Doppler profile of a transition $(v_2, J_2) \leftarrow (v, J)$ or $(v_2, J_2) \leftarrow (v_1, J_1)$, which shares either the lower or the upper common level with the pump transition, respectively. Then, the probe beam can pass through the second polarizer, and a signal will be detected. The important point is that these signals represent transitions which start from a known level and which can be therefore assigned much easier, anticipating that the pump transition is already known.

In order to confirm that the pump laser stays on the center frequency of a selected transition, a small fraction of the pump laser output is split of and is sent as a linearly polarized "extra" probe beam through the sample cell, and the normal Doppler-free polarization signal is monitored by using only pump laser. From this signal, one can select any desired line and stabilize the pump laser onto its center of the Doppler profile of the pump transition. Thus, the OODR polarization signal can

be obtained without either Doppler broadening or Doppler shift.

The various types of signals, which can be detected by the OODR polarization spectroscopy, is shown in Fig. 1. Here a lower and upper level of the pump transition are assumed to (v, J) and (v_1, J_1) level, respectively, and a upper level of the probe transition to (v_2, J_2) level. The schemes of Fig. 1(a), (b), and (c) show the three-level system cases. The type of Fig.1(a) is called V-type double resonance, where the lower level (v, J) is shared by the pump and probe transition. The type of Fig. 1(b) is called Λ-type double resonance, the upper level (v_1, J_1) is shared by the pump and probe transition, the induced fluorescence (v_1, J_1) $\rightarrow$ (v_2, J_2) can be observed. The type of Fig. 1(c) is the stepwise excitation. Only this transition among the OODR transition can be used to study highly lying levels. The schemes of Fig. 1(d) and (e) show the four-level system cases. In these two cases, the pump and probe transition is not directly coupled, but indirectly coupled by either a radiative transition [Fig. 1(d)] or non-radiative transition [Fig. 1(e)]. These different types of the OODR transition can be distinguished by the form and sign of the OODR polarization signals.

For the V-type OODR transition, the polarization factor $\zeta^{C,L}(J_1 \leftarrow J, J_2 \leftarrow J)$ is given by the nondiagonal elements in Table I (for $J_1 \neq J_2$), and one can see that the sign of the signals is different between P and R lines when a circularly polarized pump beam tune to a P or R transition line. This allows to distinguish P lines from R lines and from Q lines.

For the Λ-type OODR transition and stepwise excitation, the difference in absorption coefficient $\Delta\alpha$ (or $\delta\alpha$) is given by

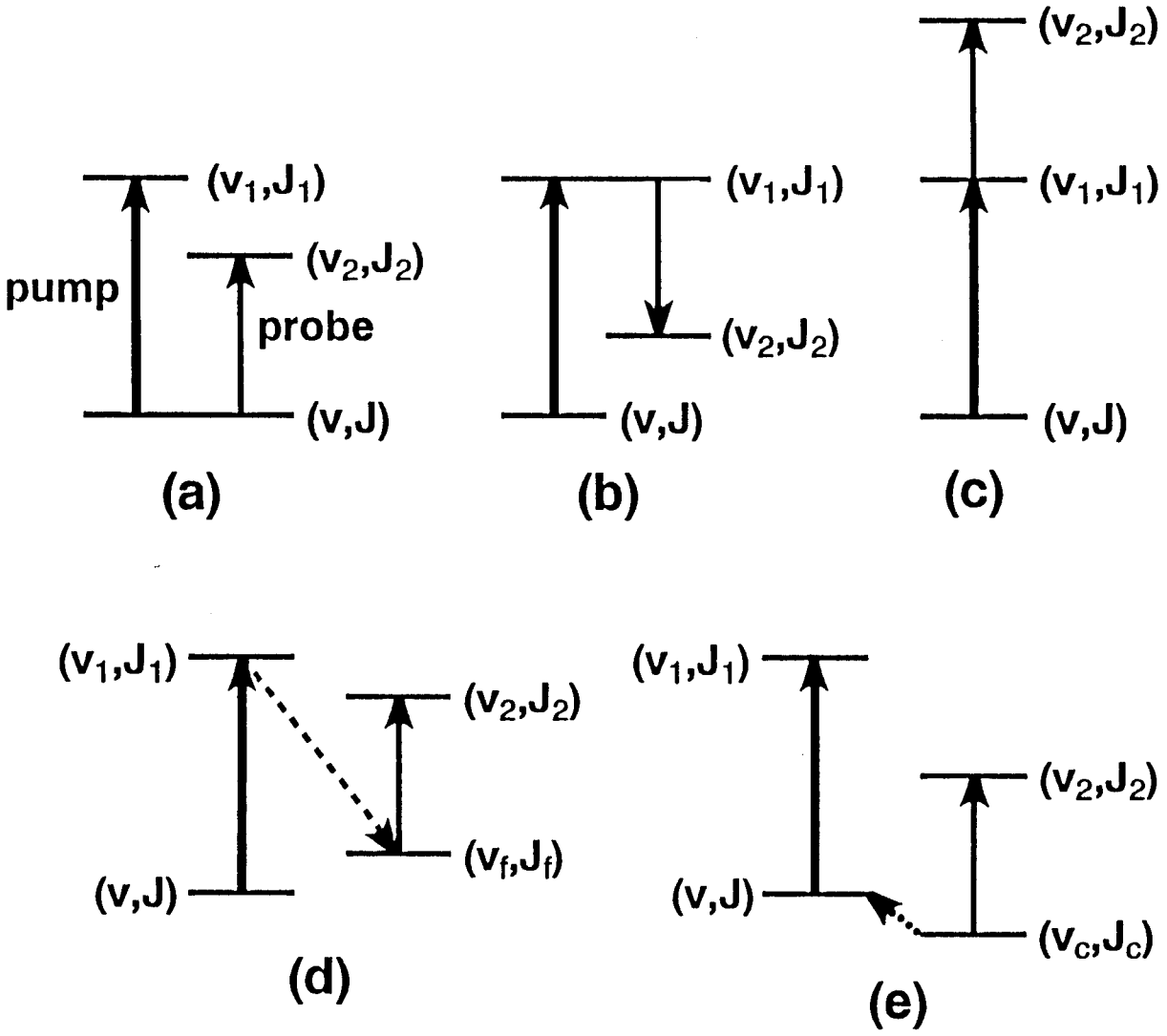

Fig. 1. Different double resonance schemes for the OODR polarization spectroscopy. (a)~(c) : three-level system; (d) and (e) : four-level system. The broken line in (d) represents a radiative transition, and the dotted line in (e) represents a non-radiative transition.

$$\Delta\alpha \text{ (or } \delta\alpha) = \frac{1}{2}\,\alpha_0\,\frac{I_{pp}}{S}\,\zeta^{C \text{ (or } L)}(J_1 \leftarrow J, J_2 \leftarrow J_1). \qquad (2.9)$$

The polarization factor $\zeta^{C,L}(J_1 \leftarrow J, J_2 \leftarrow J_1)$ is tabulated in Table II. Note that the factor $\zeta^{C,L}(J_1 \leftarrow J, J_2 \leftarrow J_1)$ is described with J_1 which is the rotational quantum number of a common level shared by the pump and probe transition. In case of the stepwise excitation, the OODR technique is very useful to study highly lying levels, which cannot accessible to direct one photon transition. A modified OODR polarization technique, called "polarization labeling", where the second laser is a broadband dye laser has been used to study highly excited states.[8-10] From the results in Ref. 8 and 9, Eq. (2.9) can be rewritten as

$$\Delta\alpha \text{ (or } \delta\alpha) = \frac{F}{(2J+1)(2J_1+1)}\,S(\Lambda_1, J_1 \leftarrow \Lambda, J) \cdot S(\Lambda_2, J_2 \leftarrow \Lambda_1, J_1) \cdot \zeta^{C(\text{or } L)}(J_1 \leftarrow J, J_2 \leftarrow J_1), \qquad (2.10)$$

where F is a factor independent on the angular momentum, and the $S(\Lambda_1, J_1 \leftarrow \Lambda, J)$ factors, called Hönl-London factors, represent the line strength for a pump and probe transitions. The Hönl-London factor $S(\Lambda_1, J_1 \leftarrow \Lambda, J)$ is tabulated in Table III. Eq. (2.10) is useful for the assignment of the electronic states excited by OODR stepwise excitation, because the information of Λ, which represents the projection of the electronic orbital angular momentum along the internuclear axis, is given by the S factors. In the case of the NaK molecule, the assignment of the electronic states which were observed by using the 2-step OODR polarization spectroscopy will be discussed in Chapter 4.

Table II. The J dependence of the polarization factor $\zeta^{C,L}(J_1 \leftarrow J, J_2 \leftarrow J_1)$.

$\zeta^{C}(J_1 \leftarrow J, J_2 \leftarrow J_1)$ (circularly polarized pump)

	probe transition		
	R: $J_2=J_1+1$	Q: $J_2=J_1$	P: $J_2=J_1-1$
pump transition			
R: $J=J_1-1$	$\frac{3}{2}$	$-\frac{3}{2J_1}$	$-\frac{3(J_1+1)}{2J_1}$
Q: $J=J_1$	$\frac{3}{2(J_1+1)}$	$-\frac{3}{2J_1(J_1+1)}$	$-\frac{3}{2J_1}$
P: $J=J_1+1$	$-\frac{3J_1}{2(J_1+1)}$	$\frac{3}{2(J_1+1)}$	$\frac{3}{2}$

$\zeta^{L}(J_1 \leftarrow J, J_2 \leftarrow J_1)$ (linearly polarized pump)

	probe transition		
	R: $J_2=J_1+1$	Q: $J_2=J_1$	P: $J_2=J_1-1$
pump transition			
R: $J_1=J-1$	$\frac{3}{10}$	$-\frac{3(2J_1+3)}{10J_1}$	$\frac{3(J_1+1)(2J_1+3)}{10J_1(2J_1-1)}$
Q: $J=J_1$	$-\frac{3(2J_1-1)}{10(J_1+1)}$	$\frac{3(2J_1+3)(2J_1-1)}{10J_1(J_1+1)}$	$-\frac{3(2J_1+3)}{10J_1}$
P: $J=J_1+1$	$\frac{3J_1(2J_1-1)}{10(J_1+1)(2J_1+3)}$	$-\frac{3(2J_1-1)}{10(J_1+1)}$	$\frac{3}{10}$

Table III. Hönl-London factor $S(J_1,\Lambda_1 \leftarrow J,\Lambda)$ of a molecular spectral line.

	$\Lambda_1=\Lambda+1$	$\Lambda_1=\Lambda$	$\Lambda_1=\Lambda-1$
$J_1=J+1$	$\frac{(J+\Lambda+2)(J+\Lambda+1)}{4(J+1)}$	$\frac{(J+\Lambda+1)(J-\Lambda+1)}{J+1}$	$\frac{(J-\Lambda+2)(J-\Lambda+1)}{4(J+1)}$
$J_1=J$	$\frac{(J+\Lambda+1)(J-\Lambda)(2J+1)}{4J(J+1)}$	$\frac{(2J+1)\Lambda^2}{J(J+1)}$	$\frac{(J-\Lambda+1)(J+\Lambda)(2J+1)}{4J(J+1)}$
$J_1=J-1$	$\frac{(J-\Lambda-1)(J-\Lambda)}{4J}$	$\frac{(J+\Lambda)(J-\Lambda)}{J}$	$\frac{(J+\Lambda-1)(J+\Lambda)}{4J}$

Chapter 3. HIGH RESOLUTION LASER SPECTROSCOPY UP TO THE DISSOCIATION LIMIT OF THE $^{23}Na^{39}K$ $B^1\Pi$ STATE, AND PREDISSOCIATION NEAR THE DISSOCIATION LIMIT

The $B^1\Pi$ state of the alkali metal diatomic molecules is correlated with separated atoms in the $^2S_{1/2}$ and $^2P_{3/2}$ states. The $B^1\Pi_u$ state of homonuclear molecules has a potential barrier caused by a repulsive long-range resonant dipole interaction.[12] Chawla et al.[13] determined the shape of the Na_2 $B^1\Pi_u$ state potential barrier by measuring the rotation-vibration line energies and linewidths of the quasibound levels using the technique of modulated gain spectroscopy. Heinze et al.[14] determined the K_2 $B^1\Pi_u$ state potential barrier. There is no resonant dipole interaction in heteronuclear molecules, and the NaK $B^1\Pi$ state is expected to dissociate to $Na(3s^2S_{1/2})$ + $K(4p^2P_{3/2})$ atoms without a potential hill near the dissociation limit. Barrow et al.[15] obtained the molecular constants of the $B^1\Pi$ state of v'=0~14 by analyzing the laser induced dispersed fluorescence spectra detected by a Fourier-transform spectrometer and the dye laser excitation spectra. Katô et al.[16] observed the $B^1\Pi$ - $X^1\Sigma^+$ transition with the technique of the Doppler-free polarization spectroscopy, and determined the molecular constants of the $B^1\Pi$ state of v'=0~16.

In order to observe the high vibrational levels near the dissociation limit and determine the long-range potential energy curve, the high resolution spectrum of the $B^1\Pi$ - $X^1\Sigma^+$ transition was measured by the Doppler-free OODR polarization spectroscopy. The transition lines up to the v'=43 level, which was estimated

to be 1.8 cm^{-1} below the dissociation limit, were observed. The molecular constants of the $B^1\Pi$ state, and the RKR potential energy curve were determined. Remarkable line broadenings were observed for the transitions to the $B^1\Pi(v', J')$ levels higher than the dissociation energy to $Na(3s^2S_{1/2}) + K(4p^2P_{1/2})$ atoms. This is identified as originating from the predissociation, and the mechanism will be discussed in chapter 3.4.

3.1 Experimental

From the calculated Franck-Condon factors between a potential of the $B^1\Pi$ state extrapolated up to the dissociation limit and the RKR potential of the $X^1\Sigma^+$ state,[17] it can be seen that the high vibrational levels near the dissociation limit of the $B^1\Pi$ state can be excited effectively from the $X^1\Sigma^+(v"=4)$ level. However, the transition lines from v"=4 are overlapped with the strong lines from v"=0 and 1. Using the technique of the Doppler-free OODR polarization spectroscopy, the transitions from the $X^1\Sigma^+(v"=4)$ level to high vibrational levels close to the dissociation limit of the $B^1\Pi$ state could be observed. The excitation scheme is shown in Fig. 2.

The experimental arrangement for a Doppler-free OODR polarization spectroscopy is shown in Fig. 3. The output of a single-mode ring dye laser 1 (Coherent CR699-21, linewidth 500 kHz, Kiton Red dye) was split into a circularly polarized strong pump beam and a linearly polarized weak "extra" probe beam. Two beams passed in opposite directions through a heat pipe. Only a small fraction of the linearly polarized probe beam, which passes a linear polarizer P1, reaches a photomultiplier PM1 (Hamamatsu

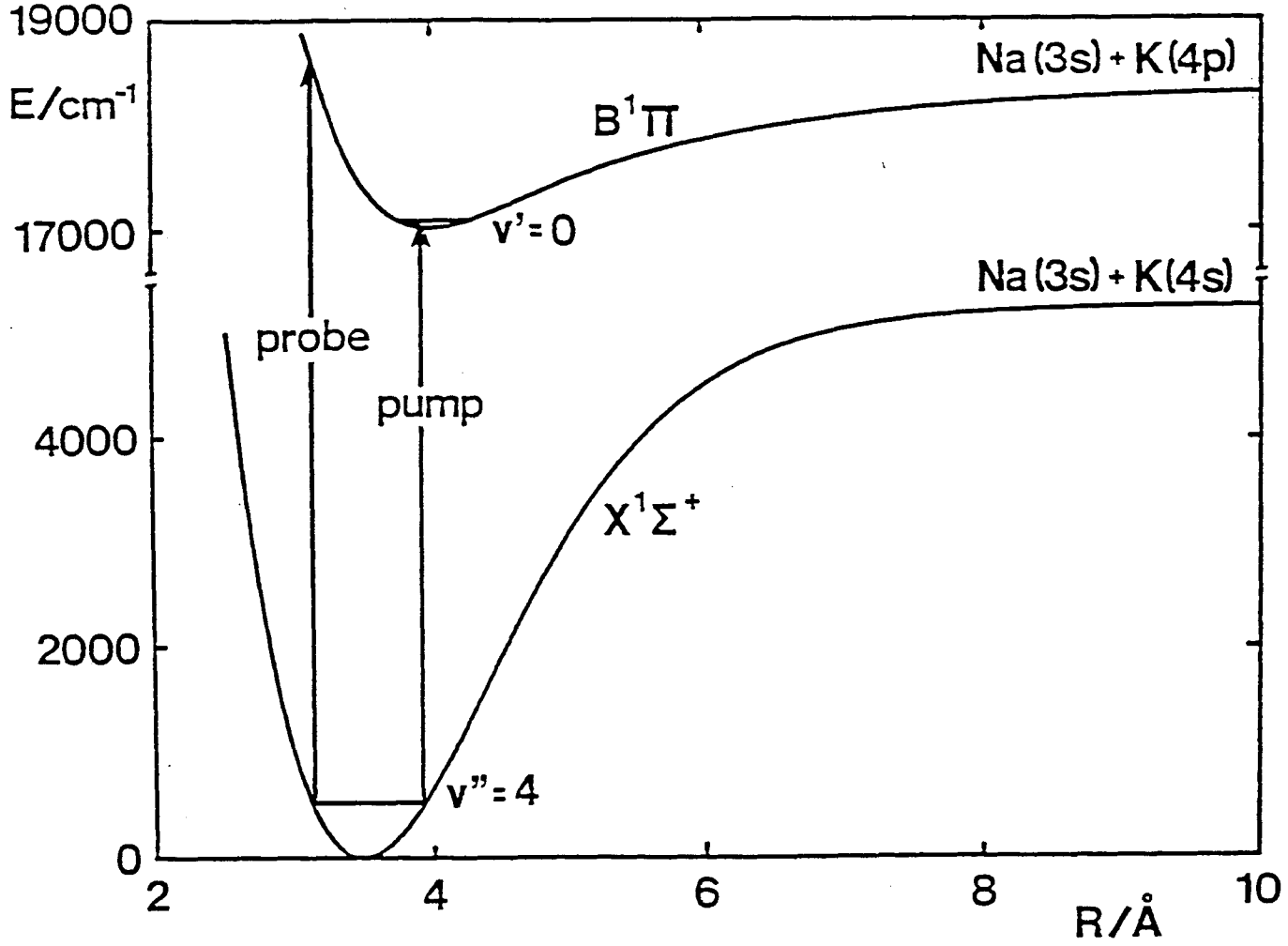

Fig. 2. A scheme of the V-type OODR polarization spectroscopy to study high vibrational levels close to the dissociation limit of the $B^1\Pi$ state.

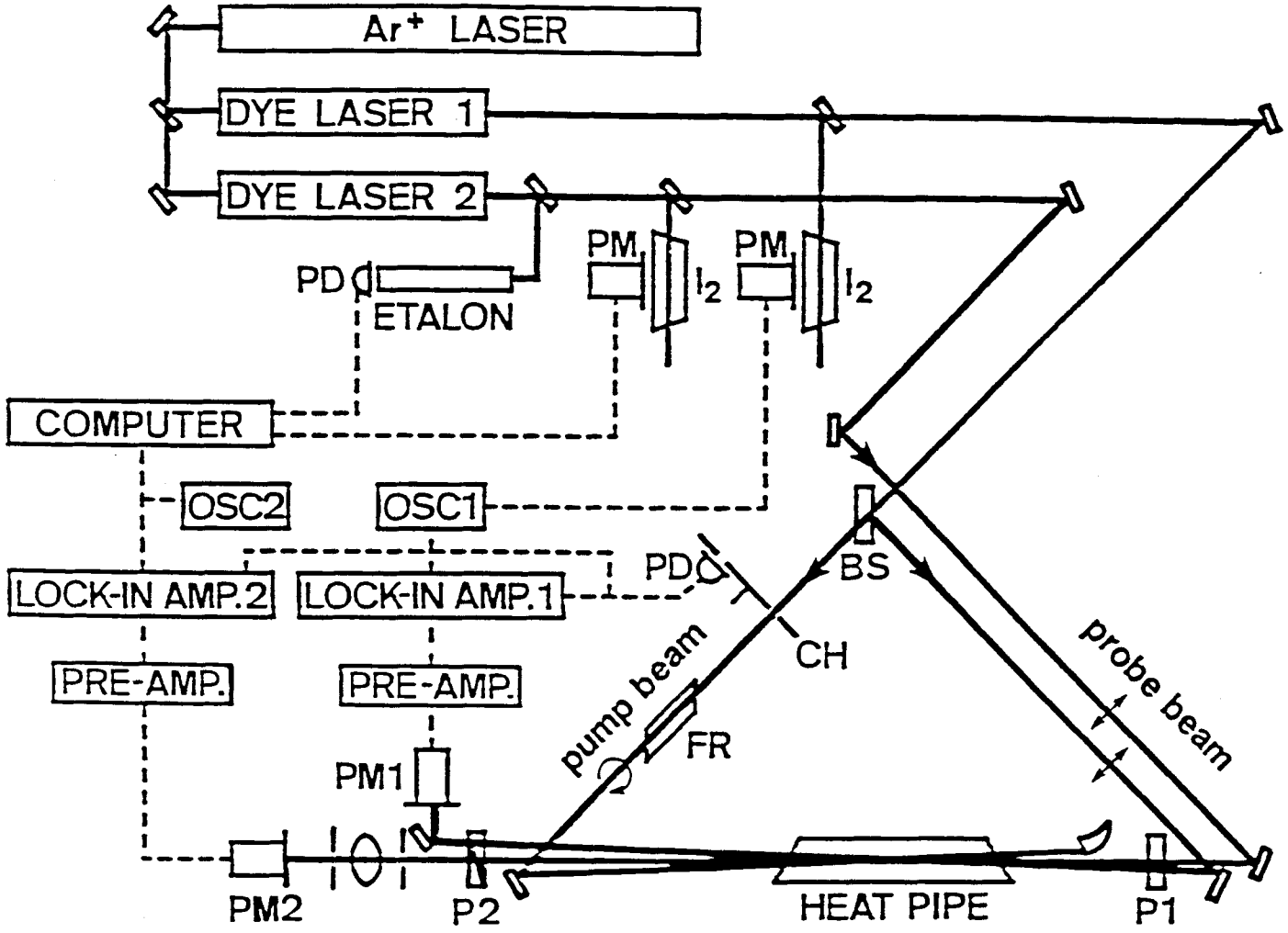

Fig. 3. Experimental setup for OODR polarization spectroscopy. BS : beam splitter, CH : chopper, FR : λ/4 Fresnel rhomb, P1 and P2 : linear polarizers, PM1 and PM2 : photomultipliers, OSC1 and OSC2 : oscilloscopes, and PD : photodiode.

R636) after passing through a crossed linear polarizer P2. The pump beam was modulated by a chopper (3kHz), and the output of the normal Doppler-free polarization signal was detected by a lock-in amplifier 1 (PAR model 128A). The pump beam is fixed to a center of Doppler-free line of a known transition $B^1\Pi(v'=0, J') - X^1\Sigma^+(v''=4, J'')$. A linearly polarized probe beam (dye laser 2; Coherent CR699-29, linewidth 500 kHz, Rhodamine 6G dye, power of 10 mW), which passes a linear polarizer P1, is propagated in the opposite direction to the pump beam through the heat pipe. Then, the probe beam passes the crossed linear polarizer P2 and reaches a photomultiplier PM2 (Hamamatsu R712). The signal output was detected by a lock-in amplifier 2 (EG&G model 5210). By choosing the polarization of the pump beam, either Q lines or P and R lines can be observed predominantly. In case of the observing P and R lines, the pump beam was circularly polarized with a $\lambda/4$ Fresnel rhomb retarder (FR). In case of the observing Q lines, the pump beam was linearly polarized at 45° against to the polarization of the probe beam. When a large number of lines are overlapped, the Doppler-free OODR polarization spectroscopy is very useful to detect selectively a series of transitions from a chosen level. Due to its high sensitivity, very weak absorption lines can be detected.

NaK vapor was produced by heating a 1:4 mixture of sodium and potassium in a stainless steel heat pipe. The heat pipe oven was operated at 550 K with Ar as buffer gas of 0.4 Torr. The continuous scanning of the laser wavelength and data processing were carried out by a microcomputer. The absolute wavenumbers of the observed spectral lines were calibrated by the fluorescence

excitation spectrum of iodine, and the fringe patterns of a confocal etalon (FSR = 150 MHz) were used as a frequency marker. The linewidth of the spectral line was sensitive to the vapor pressure and the laser power.

3.2 Determination of the Molecular Constants of the $B^1\Pi$ State

The selection rules for a transition involving a change in electronic, vibrational, and rotational state are[18]

$$\Delta J = 0, \pm 1 \text{ (except } J=0 \not\leftrightarrow J=0) \tag{3.1}$$

$$+ \leftrightarrow - \text{ (e } \leftrightarrow \text{ f for } \Delta J = 0, \text{ e } \leftrightarrow \text{ f and f } \leftrightarrow \text{ f for } \Delta J = \pm 1) \tag{3.2}$$

$$g \leftrightarrow u. \tag{3.3}$$

In Hund's case (a) and (b),

$$\Delta\Omega = 0, \pm 1 \tag{3.4}$$

$$\Delta S = 0. \tag{3.5}$$

For a $^1\Pi$ - $^1\Sigma^+$ transition, the allowed transitions are three branches, P, Q, and R. With a circularly polarized pump beam, only P and R transitions are detected in the OODR polarization spectrum, and the signs are different in P and R transitions. Hence, the assignments are easy and can be accurate. A part of the OODR polarization spectrum and the normal polarization spectrum are shown in Fig. 4. In the normal polarization spectrum [Fig. 4(C)], the intensities of the transitions from the $X^1\Sigma^+$ (v"=0 and 1) levels were strong, but the transitions from the $X^1\Sigma^+$(v"=4, J"=17) level were not detected with appreciable intensity. In the OODR polarization spectrum [Fig. 4(B)], the P and R transitions from the selected $X^1\Sigma^+$(v"= 4, J"=17) level were observed predominantly, where the $B^1\Pi$(v'=0, J'=18) - $X^1\Sigma^+$(v"=4,

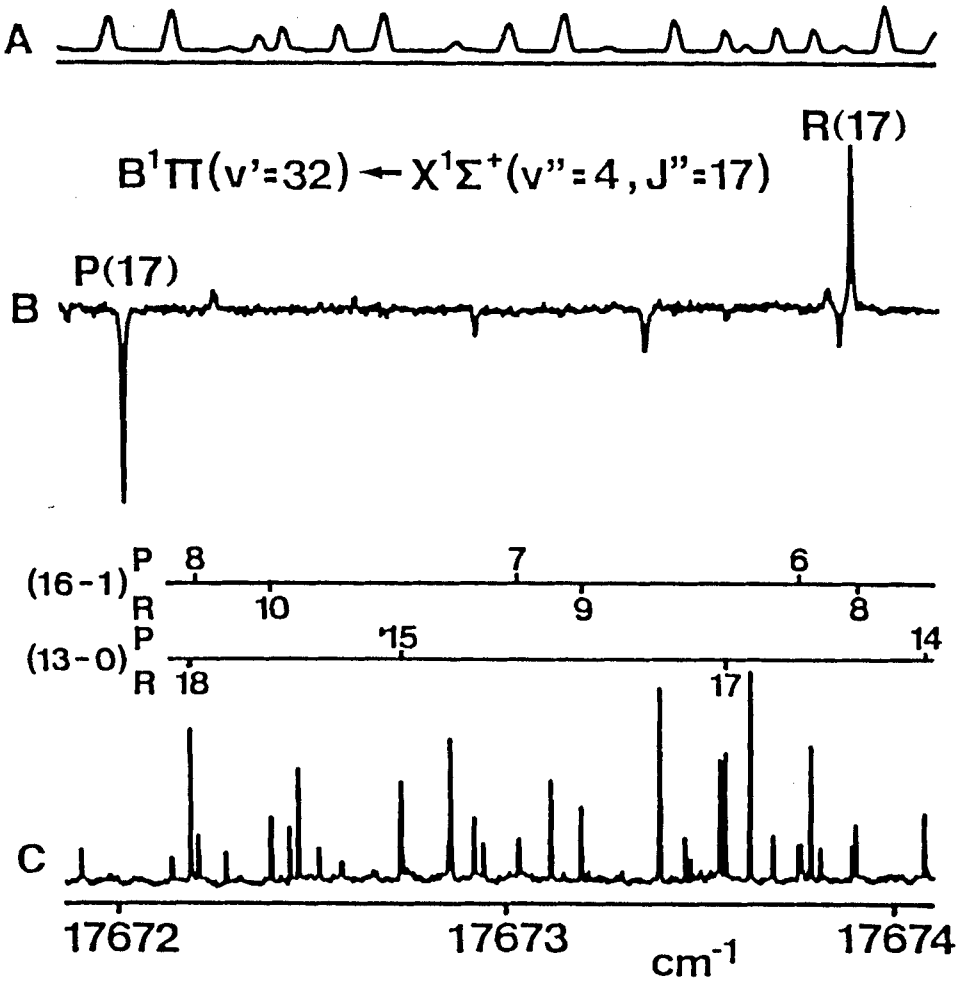

Fig. 4. Top (A) is the fluorescence excitation spectrum of I_2 for calibration of the absolute wavenumber. The second (B) is a part of the OODR-polarization spectrum, where the $B^1\Pi(v'=0, J'=18) - X^1\Sigma^+(v"=4, J"=17)$ transition is used as the pump transition. Bottom (C) is the normal polarization spectrum and a part of the assignments.

J"=17) transition at 16476.1728 cm^{-1} was chosen as the pump transition by a circularly polarized pump beam. The extra lines of weak intensity are the transitions from the pumped $B^1\Pi$(v'=0, J'=18) level and the collisionally depopulated $X^1\Sigma^+$ (v"=4, J") levels. When the $B^1\Pi$(v'=0, J'=18) - $X^1\Sigma^+$(v"=4, J"=17) transition was chosen as the pump transition, the probe laser was scanned from 17250 to 17755 cm^{-1}. The $B^1\Pi$(v', J'=16 and 18) - $X^1\Sigma^+$(v"=4, J"=17) transitions up to the v"=43 level could be observed, and the observed lines are listed in Table IV.

The term energy $E_{v,J}$ is expressed in Eq. (1.3) and (1.4). From the Eq. (1.3), the energy separation between the R(J) and P(J) lines is given by

$$E_{v,J+1} - E_{v,J-1} = (4J+2)B_v - 2(J^2+J+1)(4J+2)D_v + \cdots. \quad (3.6)$$

For J=17, the higher order terms can be neglected, but the terms up to D_v cannot be neglected.

At first, we have approximated the value of D_v by

$$D_v = \sum_{i=0,\cdots,3} Y_{i2}(v+1/2)^i, \quad (3.7)$$

where the Dunham coefficients Y_{i2} were determined for v'=0-16 in Ref. 16. From a pair of P(17) and R(17) lines, which are listed in Table IV, we calculated the values of B_v and E_v^o for v'=15-43. The values for v'=15 and 16 were in good agreement with the values reported in Ref. 16. The E_v^o and B_v values for v'=16-43 and the values for v'=0-15 in Ref. 16 were taken together as input data of least-squares fitting, which yielded the Dunham coefficients Y_{ij}(i=0 and 1):[19]

Table IV. Observed lines (in units of cm^{-1}) of the $^{23}Na^{39}K$ $B^1\Pi$ (v', J'=16 and 18) - $X^1\Sigma^+$(v"=4, J"=17) transitions measured by the OODR polarization spectroscopy. Pump beam is fixed to the $B^1\Pi$(v'=0, J'=18) - $X^1\Sigma^+$(v"=4, J"=17) transition at 16476.1728 cm^{-1}.

	Probe transitions	
v'	$B^1\Pi$(v', 16) - $X^1\Sigma^+$(4, 17)	$B^1\Pi$(v', 18) - $X^1\Sigma^+$(4, 17)
15	17262.1180	17265.6801
16	17298.1477	17301.5988
17	a	a
18	17365.5094	17368.7598
19	17396.5714	17399.7272
20	17426.0677	17429.1222
21	17454.0121	17456.9759
22	17480.4105	17483.2287
23	17505.7997	17508.4941
24	17529.2262	17531.8889
25	17551.4083	17553.9799
26	a	a
27	17591.7914	17594.2435
28	17610.4232	17612.6948
29	17627.5589	17629.7409
30	17643.6550	17645.7304
31	17658.3327	17660.0983
32	17672.0339	17673.8876
33	17684.2674	17686.0351
34	17695.0490	17696.6299
35	17705.0780	17706.5818
36	17713.3327	17714.7392
37	17720.1784	17721.4058
38	17726.1100	17727.1912
39	17730.9772	17731.9473
40	17734.5880	17735.4286
41	17737.2491	17737.9418
42	17739.0423	17739.5765
43	17740.0896	17740.4112

[a] Unlisted ones are strongly perturbed lines or weak and undetected lines.

Table V. Molecular constants E_v^o and B_v for v'=16-43 of the $^{23}Na^{39}K$ $B^1\Pi$ state. All values are in units of cm^{-1}. The values for v'=0-16 are given in Table I of Ref. 16.

v	E_v^o	$10^2 B_v$	
16	17861.1958	4.98702	
17	—	—	
18	17929.3469	4.67080	
19	17960.7753	4.53557	
20	17990.6638	4.39081	
21	18018.9592	4.26133	
22	18045.9211	4.05344	
23	18071.7892	3.87687	
24	18095.3378	3.83196	
25	18117.8719	3.70233	
26	—	—	
27	18158.7149	3.53340	
28	18178.0436	3.27682	
29	18195.5239	3.15032	
30	18212.0298	2.99998	
31	18227.9033	2.55977	a)
32	18241.2582	2.68909	
33	18253.8189	2.57006	
34	18265.3165	2.30795	
35	18275.6352	2.20369	
36	18284.2559	2.07180	
37	18291.7836	1.82406	
38	18298.2670	1.62404	
39	18303.5555	1.47117	
40	18307.6503	1.29771	
41	18310.8655	1.09869	
42	18313.2527	0.88530	
43	18315.1014	0.59602	

a) The anomalous value may be originating from the perturbation.

Table VI. Dunham coefficients for the $^{23}Na^{39}K$ $B^1\Pi$ state. All values are in units of cm^{-1}. The value of T_e, Y_{i0}(i=0 to 4), Y_{i1}(i=0 to 3), and Y_{i2}(i=0 and 1) were fixed to the values derived in Ref. 16.

T_e	16992.7446	Y_{01}	7.23853×10^{-2}
Y_{00}	-0.0430	Y_{11}	-1.17799×10^{-3}
Y_{10}	71.4630	Y_{21}	-1.3502×10^{-5}
Y_{20}	-1.15092	Y_{31}	-4.7933×10^{-7}
Y_{30}	-1.0613×10^{-2}	Y_{41}	4.82977×10^{-8}
Y_{40}	9.9950×10^{-4}	Y_{51}	-6.88606×10^{-10}
Y_{50}	-1.42656×10^{-5}	Y_{61}	-1.13984×10^{-11}
Y_{60}	-8.67783×10^{-7}	Y_{71}	2.09534×10^{-13}
Y_{70}	4.74996×10^{-8}	Y_{02}	-2.89859×10^{-7}
Y_{80}	-9.30786×10^{-10}	Y_{12}	-1.93901×10^{-8}
Y_{90}	6.67343×10^{-12}	Y_{22}	6.45399×10^{-10}
		Y_{32}	-7.75355×10^{-12}
		Y_{42}	9.91847×10^{-13}
		Y_{52}	-3.46351×10^{-14}

$$E_v^o - T_e - B_v = \sum_{i=0,\cdots,9} Y_{i0}(v + 1/2)^i, \quad (3.8)$$

$$B_v = \sum_{i=0,\cdots,7} Y_{i1}(v + 1/2)^i, \quad (3.9)$$

where the values of T_e, Y_{i0}(i=0-4), and Y_{i1}(i=0-3) were fixed to those in Ref. 16. From the Dunham coefficients Y_{i0} and Y_{i1} obtained above, the rotationless potential curve of the $B^1\Pi$ state is constructed up to the v'=43 level by the Rydberg-Klein-Rees (RKR) method.[19,20] We noticed that the inner wall of the RKR potential increases at v'≥40. We made a correction, and the method is described in the next section. For the corrected RKR potential curve, the values of E_v^o, B_v, and D_v are calculated by a computational method described by Hutson.[21] The obtained value of D_v was slightly different from the value of D_v approximated by Eq. (3.7). Hence, by using the new D_v value, we have calculated again the E_v^o and B_v values from a pair of P(17) and R(17) lines in Table IV, and the results are listed in Table V. From the new E_v^o and B_v values for v'=16-43 and those for v'=0-15, we have calculated the Dunham coefficients, and the results are listed in Table VI.

3.3 Long-range potential of the $B^1\Pi$ state

From the Dunham coefficients Y_{i0} and Y_{i1}, the rotationless potential curve of the $B^1\Pi$ state was constructed up to v'=43 by the RKR method.[20,21] Let us denote the outer and inner turning points of a vibrational level v as $R_+(v)$ and $R_-(v)$, respectively. The inner wall of the calculated RKR potential bent over at v'≥40 and the inner turning point $R_-(v')$ increased with v'. At v'=42 and 43, the inner wall increased abruptly. Such a nonphysical

inner-wall behavior in the RKR inversion procedure was discussed by Wells, Smith, and Zare.[23] They showed that the RKR procedure was very sensitive to the errors in the B_v values, but relatively insensitive to the G_v values. The distance between the outer and inner classical turning points of a vibrational level v, $R_+(v) - R_-(v)$, is given by the Klein action integral f, which is calculated from the G_v values. We modified the inner-wall by a repulsive potential:[24] $V(R) = A/R^{12} + B$, where R is the internuclear distance. The constants A and B were determined by fitting to the inner turning points of v' =30 to 34; $A = 3.85547 \times 10^9$ $cm^{-1}Å^{12}$ and $B = -1450.79$ cm^{-1} for the RKR potential calculated from the Dunham coefficients in Table VI. The outer turning points were adjusted by adding the distance $R_+(v) - R_-(v)$ to the extrapolated inner turning points. The resulting RKR turning points are listed in Table VII, and are shown in Fig. 5.

Many theoretical studies on the long-range interactions of alkali metals[12,25-28] and the experimental studies by the crossed beam technique[29,30] have been reported. The long-range interaction energy between Na(3s) and K(4p) atoms may be expressed as[28]

$$V(R)^{int} = - \frac{C_6}{R^6} - \frac{C_8}{R^8} - \frac{C_{10}}{R^{10}} - \cdots, \qquad (3.10)$$

where C_6, C_8, and C_{10} are constants. These constants can be determined by analyzing outer RKR turning points in the long-range.[31,32] According to the criterion proposed by LeRoy,[31] the inverse-power expansion of interaction energy is valid for $R \geq 2[(\langle r_A^2 \rangle)^{1/2} + (\langle r_B^2 \rangle)^{1/2}]$, where $\langle r_X^2 \rangle$ is the expectation value of the square of the radius of the outermost electrons on atom X. For Na(3s) + K(4s), the value of $2[(\langle r_{Na}^2 \rangle)^{1/2} +$

Table VII. RKR-extrapolated potential of the $^{23}Na^{39}K$ $B^1\Pi$ state. R_- and R_+ are, respectively, inner and outer turning points of each vibrational level v. R_e is the equilibrium internuclear distance.

v	$V(R)/cm^{-1}$	R_-/Å	R_+/Å
		R_e = 4.0134 Å	
-0.25	17.7507	3.8929	4.1489
0.	35.3995	3.8467	4.2103
1.00	104.5311	3.7402	4.3790
2.00	171.2929	3.6735	4.5105
3.00	235.6649	3.6229	4.6286
4.00	297.6453	3.5818	4.7402
5.00	357.2477	3.5470	4.8686
6.00	414.4992	3.5168	4.9556
7.00	469.4370	3.4903	5.0623
8.00	522.1065	3.4668	5.1696
9.00	572.5591	3.4457	5.2779
10.00	620.8503	3.4267	5.3879
11.00	667.0383	3.4095	5.4997
12.00	711.1827	3.3940	5.6138
13.00	753.3433	3.3798	5.7305
14.00	793.5799	3.3669	5.8499
15.00	831.9514	3.3551	5.9723
16.00	868.5156	3.3443	6.0981
17.00	903.3294	3.3344	6.2273
18.00	936.4479	3.3252	6.3603
19.00	967.9254	3.3168	6.4974
20.00	997.8143	3.3091	6.6388
21.00	1026.1658	3.3019	6.7849
22.00	1053.0292	3.2953	6.9360
23.00	1078.4516	3.2892	7.0926
24.00	1102.4776	3.2836	7.2552
25.00	1125.1485	3.2785	7.4243
26.00	1146.5016	3.2739	7.6007
27.00	1166.5694	3.2699	7.7854
28.00	1185.3787	3.2663	7.9795
29.00	1202.9500	3.2633	8.1846
30.00	1219.2966	3.2608	8.4026
31.00	1234.4244	3.2589	8.6361
32.00	1248.3322	3.2574	8.8885
33.00	1261.0122	3.2563	9.1642
34.00	1272.4524	3.2552	9.4689
35.00	1282.6387	3.2542	9.8107
36.00	1291.5601	3.2533	10.2008
37.00	1299.2149	3.2526	10.6542
38.00	1305.6190	3.2520	11.1919
39.00	1310.8181	3.2514	11.8416
40.00	1314.9014	3.2510	12.6368
41.00	1318.0209	3.2507	13.6009
42.00	1320.4140	3.2505	14.6841
43.00	1322.4316	3.2503	15.6318

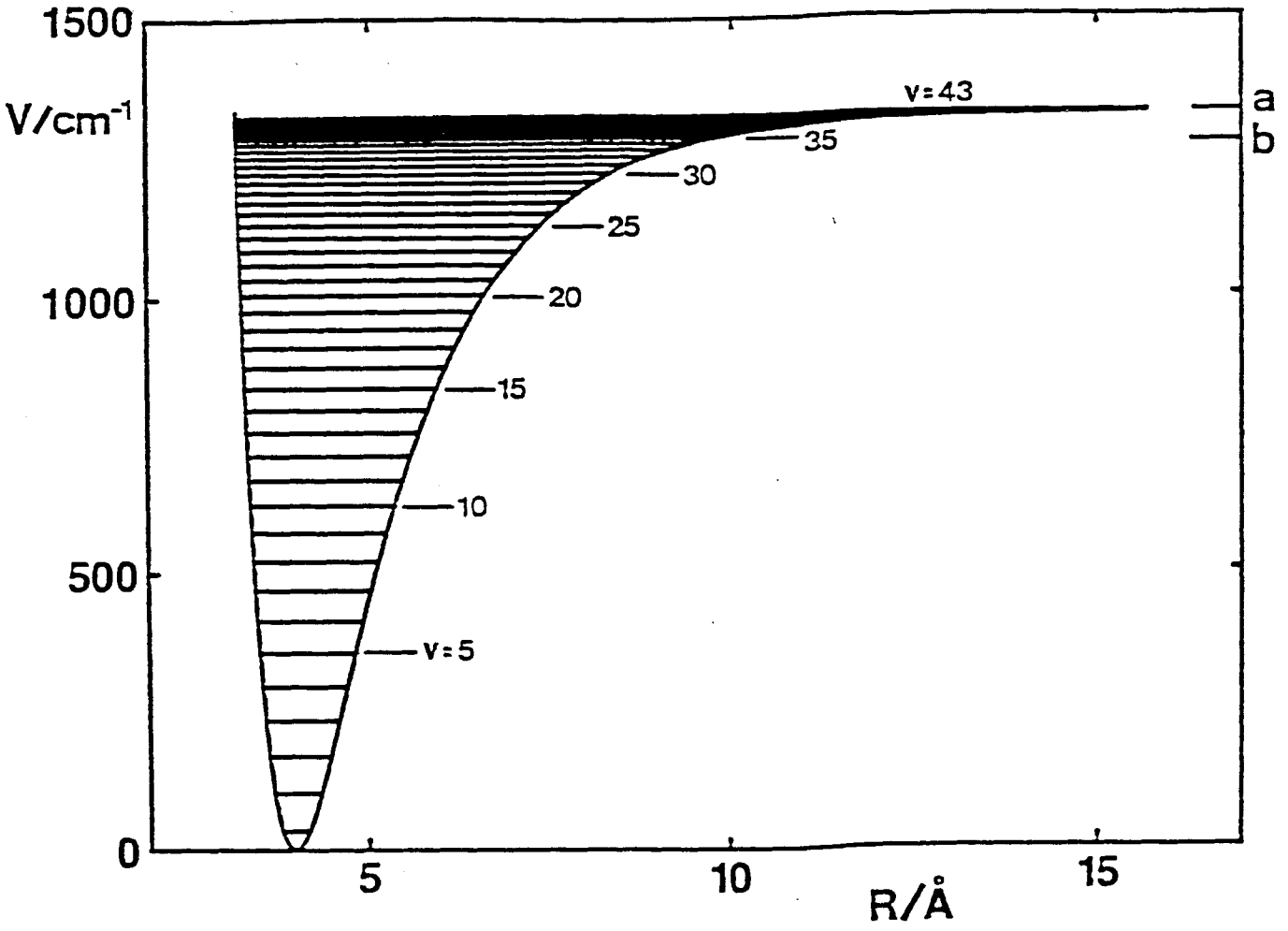

Fig. 5. The rotationless RKR potential energy curve of the NaK $B^1\Pi$ state. The horizontal lines show the observed vibrational levels. The dissociation limit to $Na(3s^2S_{1/2}) + K(4p^2P_{3/2})$ atoms is shown as a. The dissociation limit to $Na(3s^2S_{1/2}) + K(4p^2P_{1/2})$ atoms is shown as b.

$(\langle r_K^2 \rangle)^{1/2}]$ is reported to be 10.8 Å.[6] The vibrational energy G_v is plotted against the $[R_+(v)]^{-6}$, and it is shown in Fig. 6. The plot is linear in the limit of large $R_+(v)$ and the constant C_6 is determined to be 37.4×10^6 $cm^{-1}Å^6$ from the slope. In the same way, we can determine the constant C_8 from a plot of $G_v - C_6/[R_+(v)]^6$ against $[R_+(v)]^{-8}$. However, an appreciable deviation from the linear fit in Fig. 6 is observed only at $[R_+(v)]^{-6} > 10^{-6}$ $Å^{-6}$, where the inverse-power expansion of interaction energy becomes invalid. Hence, the interaction energy of higher order than the C_6/R^6 term is expected to be small at R≥10 Å and cannot be derived from the present data. Bussery and Aubert-Frécon[28] calculated the long-range coefficients by a perturbation model, and obtained $C_6 = 35.7 \times 10^6$ $cm^{-1}Å^6$ and $C_8 = -0.51 \times 10^8$ $cm^{-1}Å^8$. They neglected the effect of spin-orbit interaction (we shall discuss about this effect in the next section), but these values are in fairly good agreement with our results.

For long-range potentials expressed as

$$V(R) = D_e - \frac{C_n}{R^n}, \tag{3.11}$$

where D_e is the dissociation energy, LeRoy and Bernstein[23] derived the relation

$$\frac{dG_v}{dv} = K_n[D_e - G_v]^{(n+2)/2n}, \tag{3.12}$$

where K_n is a constant proportional to $C_n^{-1/n}$. For n=6, it can be written as

$$(\Delta G_v)^{3/2} = (K_6)^{3/2}[D_e - G_v], \tag{3.13}$$

where $\Delta G_v = G_{v+1} - G_v$. The values of $(\Delta G_v)^{3/2}$ are plotted against G_v for the observed high v levels of the $B^1\Pi$ state in

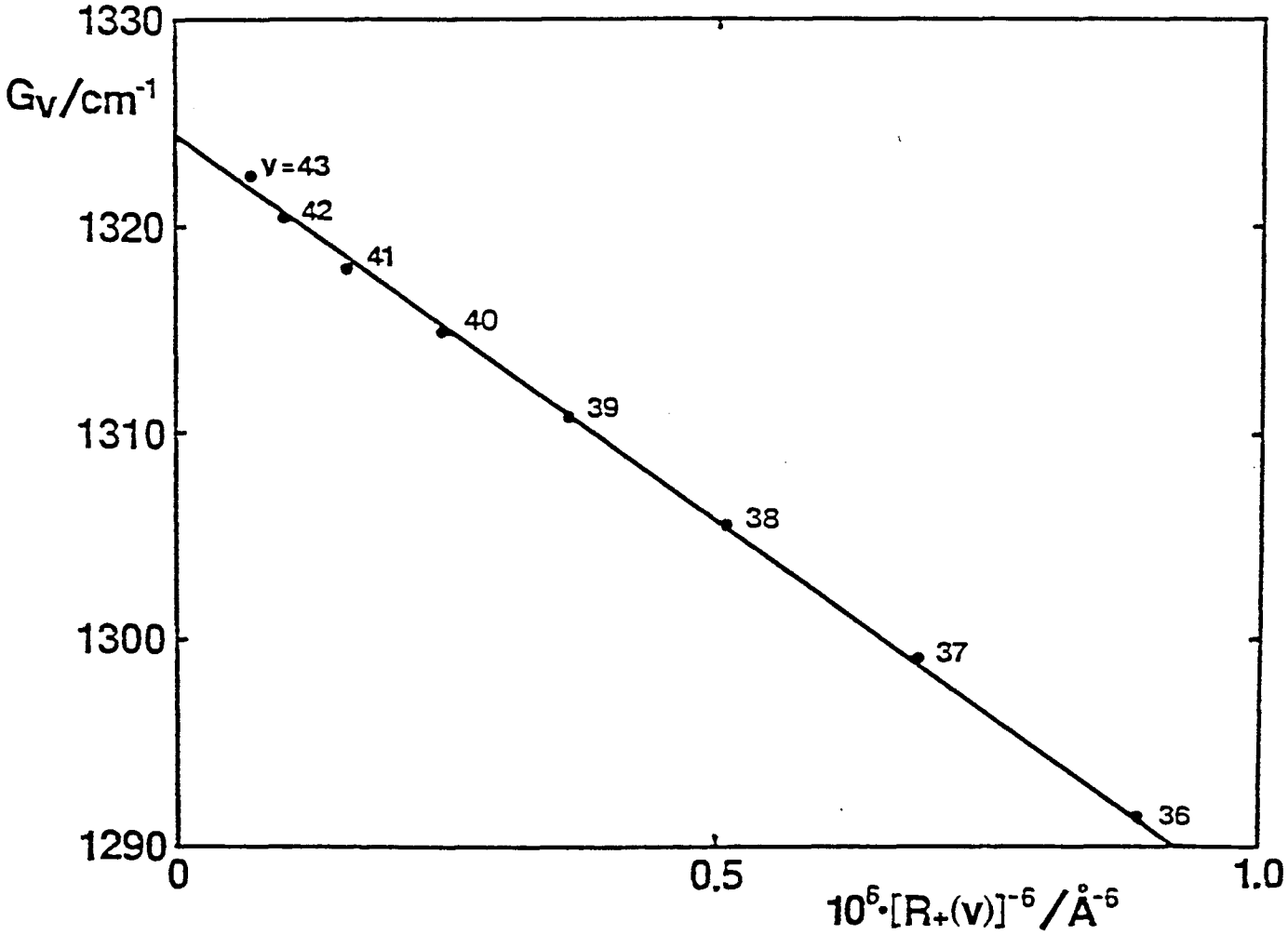

Fig. 6. Plots of G_v for high v levels in the $B^1\Pi$ state against $[R_+(v)]^{-6}$, where $R_+(v)$ is the outer turning point of a vibrational level v.

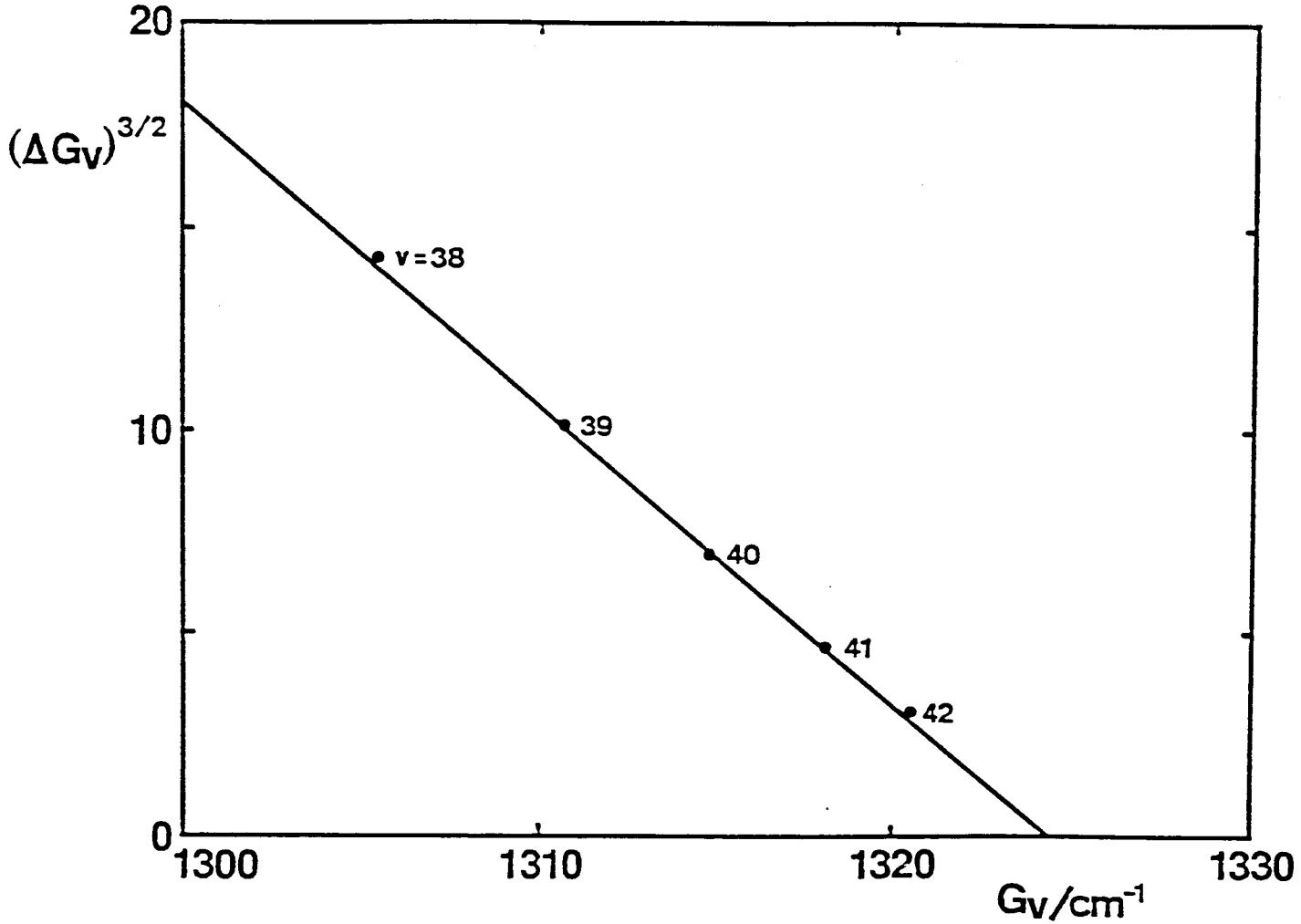

Fig. 7. LeRoy-Bernstein plot; $(\Delta G_v)^{3/2}$ is plotted against the vibrational term value G_v for high v levels in the $B^1\Pi$ state. The intercept of extrapolated line yields the dissociation energy D_e = 1324.3±0.3 cm^{-1}.

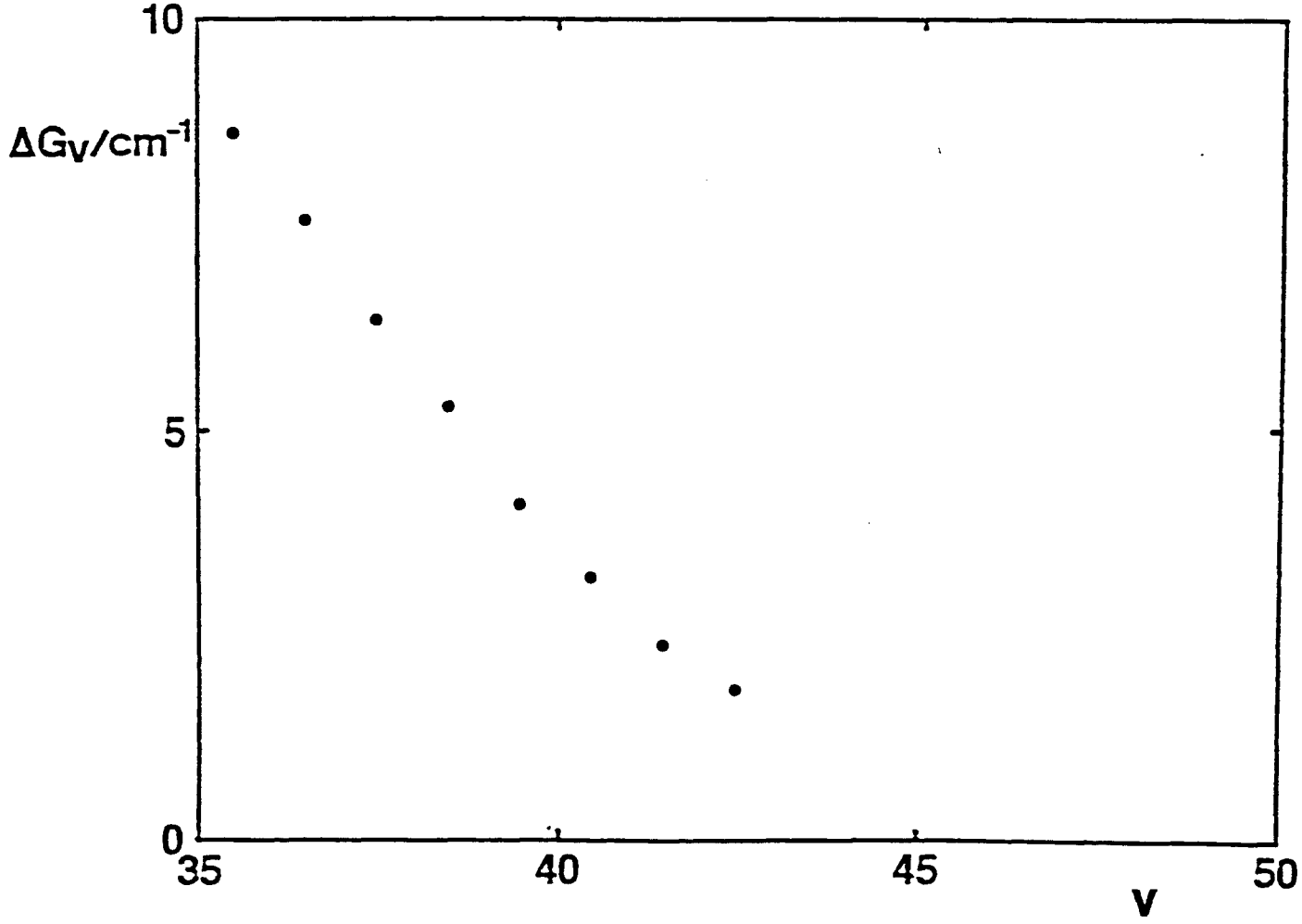

Fig. 8. Birge-Sponer plot; ΔG_v is plotted against v.

Fig. 7. The plot is linear and the dissociation energy is determined to be 1324.3±0.3 cm^{-1} from the extrapolation. The Birge-Sponer plot,[34] which is the plot of the ΔG_v against v, is shown in Fig. 8. Compared to the LeRoy-Bernstein plot [Fig. 7], there is more flexibility in extrapolating the convergence limit. The LeRoy-Bernstein plot is found to be more useful than the Birge-Sponer plot when transitions close to the dissociation limit, where the long-range potential can be expressed by Eq. (3.12), are observed.

Ross et al.[17] reported D_e of the $X^1\Sigma^+$ state to be 5274.9±0.5 cm^{-1}. D_e of the $B^1\Pi$ state can also be obtained from the atomic energy level difference $\Delta E[K(4p^2P_{3/2}) - K(4s^2S_{1/2})]$ = 13042.89 cm^{-1} and the minimum electronic energy T_e = 16992.7446 cm^{-1} reported in Ref. 16;

$$D_e(B^1\Pi) = D_e(X^1\Sigma^+) + \Delta E[K(4p^2P_{3/2}) - K(4s^2S_{1/2})] - T_e$$
$$= 1325.05 \pm 0.5 \text{ cm}^{-1}.$$

This value and the one obtained by the LeRoy-Bernstein plot are coincident within the experimental errors.

From the obtained dissociation energy, the highest observed v'=43 level is estimated to be 1.8 cm^{-1} below the dissociation limit. Thus 99.86±0.02 % of the well depth of the $B^1\Pi$ state is covered by OODR polarization experiment.

3.4 Predissociation near the Dissociation Limit of the $B^1\Pi$ State

The spectral line shapes of the $B^1\Pi(v'=29\sim43, J'=16)$ - $X^1\Sigma^+(v''=4, J''=17)$ transitions are shown in Fig. 9. Similar spectral lines with opposite sign were observed for the R lines. A remarkable line broadening was observed for transitions to the levels of $v'\geq33$. The energy threshold of the broadening is coincident with the dissociation limit to $Na(3s^2S_{1/2})$ + $K(4p^2P_{1/2})$ atoms, which is located 57.72 cm^{-1} below the one to $Na(3s^2S_{1/2})$ + $K(4p^2P_{3/2})$ atoms. Any irregular line shifts were not observed for all the broadened lines. The v'-dependence of the linewidths (FWHM) of the P(17) and R(17) lines are plotted in Fig. 10. For the levels of $v'\leq32$, the linewidth is observed to be about 200 MHz. However, the linewidth of v'=34 is found to be 3.4 GHz. This line broadening may originate from the predissociation, and the rate can be estimated from the linewidth to be about 2×10^{10} s^{-1} for v'=34. The linewidth decreases somewhat for $v'\geq35$, but is still broader than those for $v'\leq32$.

In the Hund's case (a) representation there are four molecular states, $^1\Sigma^+$, $^1\Pi$, $^3\Sigma^+$, and $^3\Pi$, correlated with the separated atoms Na(3s) + K(4p). By neglecting the spin-orbit interaction, Stevens et al.[35] calculated the potential energy curves for all these states up to R = 20 a_o by the full-valence configuration interaction computations. We added a - C_{10}/R^{10} term to the long-range potential curve obtained by Bussery and Aubert-Frecon,[28] and the C_{10} value was determined so as to fit with the potential energies at R = 15 and 20 a_o obtained by Stevens et al.[35] The resulting potential curves are shown in Fig. 11(A).

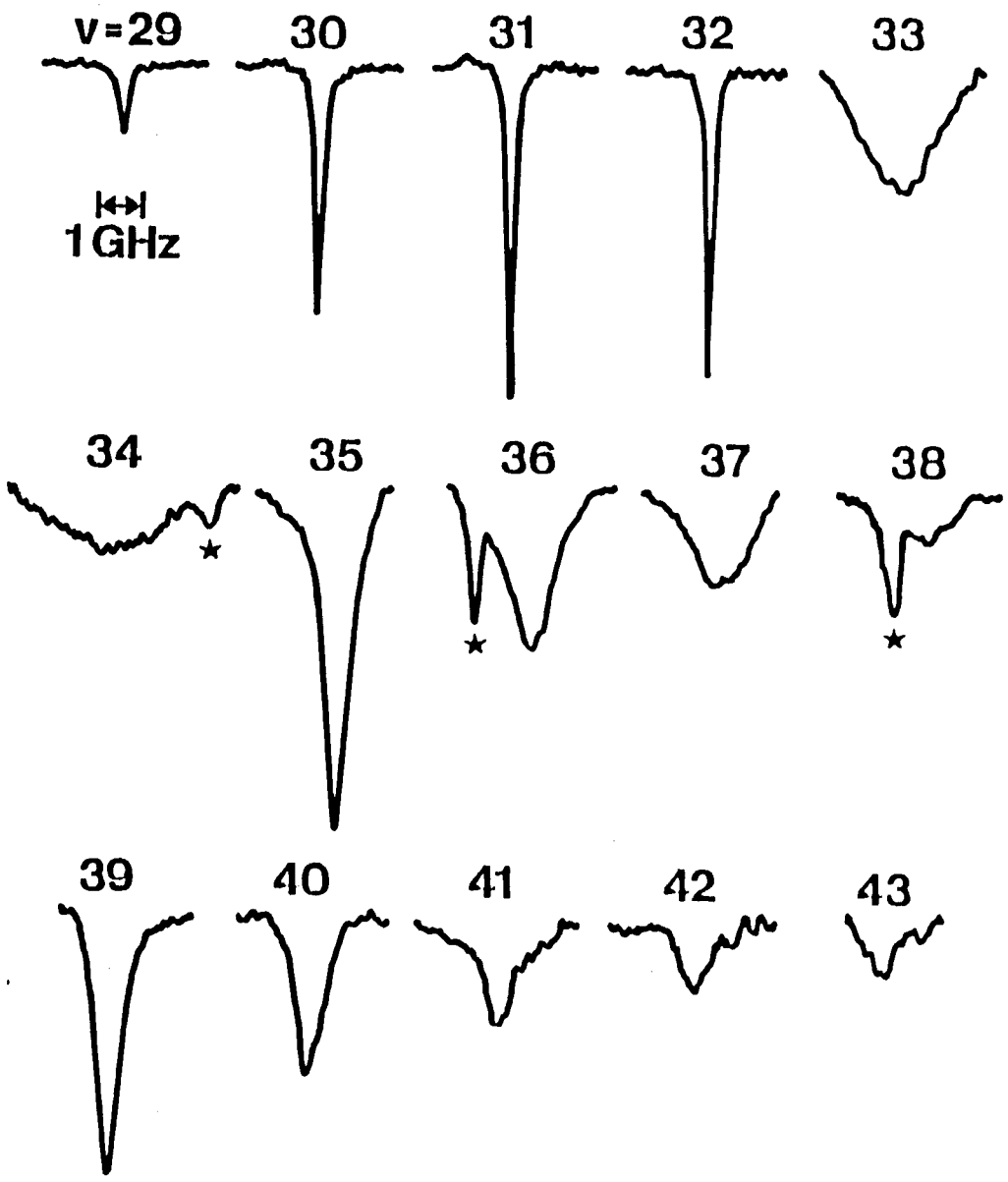

Fig. 9. The observed line shapes of the $B^1\Pi$(v'=29-43, J'=16) - $X^1\Sigma^+$(v"=4, J"=17) transitions. The frequency scale is shown on the top. Lines with ★ are accidentally overlapped lines, which are not observed for the corresponding R lines.

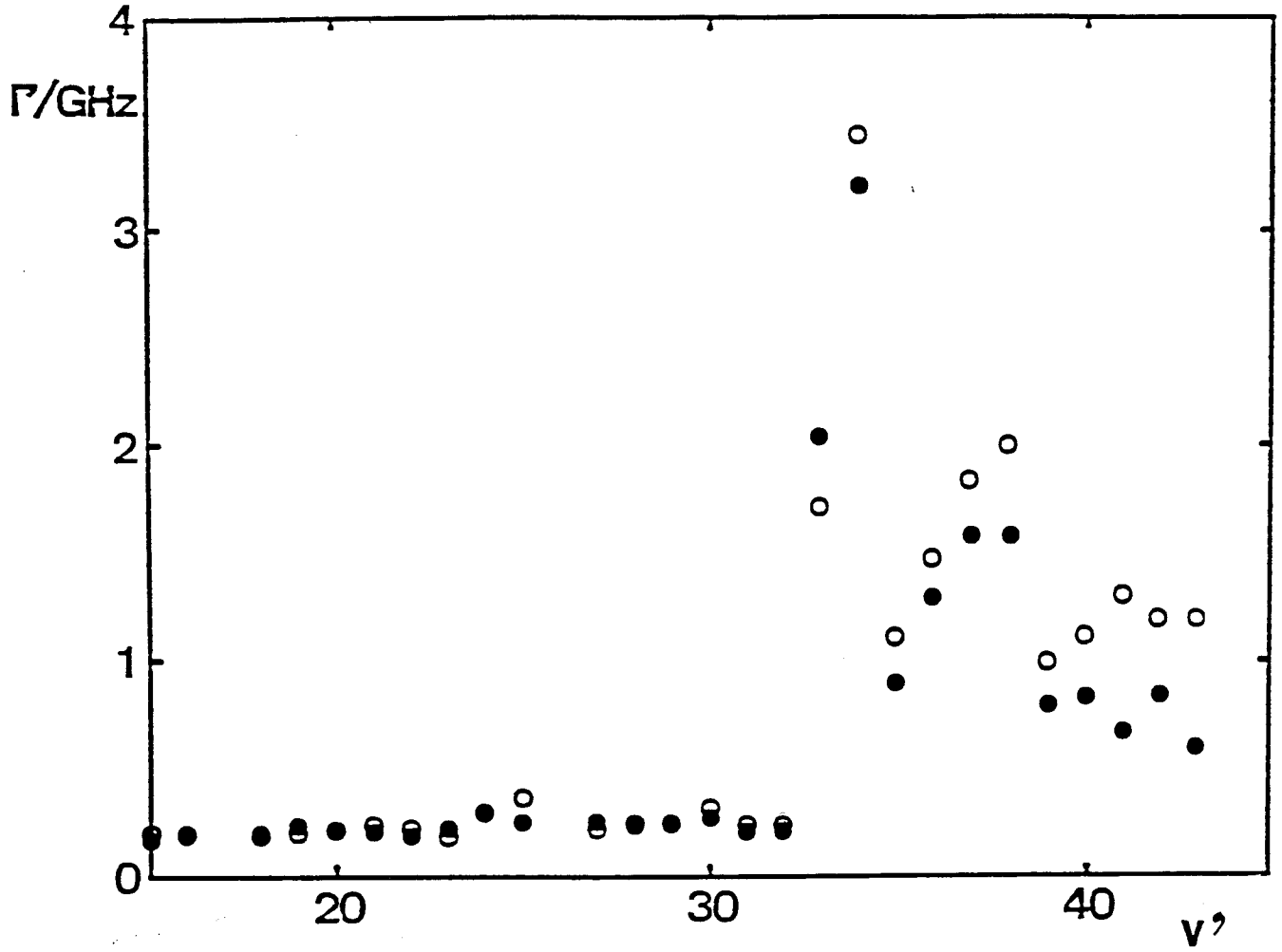

Fig. 10. The linewidths Γ of the $B^1\Pi$(v'=15-43, J'=16 and 18) - $X^1\Sigma^+$(v"=4, J"=17) transitions. An open circle (o) is for the R branch and a filled circle (●) for the P branch.

At long internuclear distances, the effect of the spin-orbit interaction cannot be neglected, and the electronic states transform into Hund's case (c) states. The $B^1\Pi(\Omega=\pm1)$ state transforms into the 1(a) state at long internuclear distances, and the outer RKR turning points in the long-range determined above compose the potential curve of the 1(a) state. The energies and eigenfunctions for a given value of R can be obtained by diagonalizing the energy matrix composed of long-range interaction and spin-orbit interaction. The resulting energies are plotted in Fig. 11(B). The spin-orbit interaction mixes the $^1\Pi(\Omega=\pm1)$, $^3\Pi(\Omega=\pm1)$, and $^3\Sigma^+(\Omega=\pm1)$ states, but the mixing of the $^3\Sigma^+(\Omega=\pm1)$ state, which is correlated with the separated atoms $Na(3s^2S_{1/2})$ + $K(4p^2P_{1/2})$, is small for the 1(a) state [see Table VIII]. The potential curve of the 1(a) state does not cross with any curves of the other states in the long-range [see Fig. 11(B)]. Hence, the predissociation of the $B^1\Pi(\Omega=\pm1)$ state to $Na(3s^2S_{1/2})$ + $K(4p^2P_{1/2})$ atoms through the interaction at long-range is expected to be negligibly small.

In order to cause an appreciable predissociation, a repulsive potential curve must either come very near to, or cross, the $B^1\Pi$ state curve. According to the computations by Stevens et al.,[35] the $(2)^3\Sigma^+$ curve comes close to the $B^1\Pi$ curve on the inner limb and crosses just above the dissociation limit. The perturbation between the $B^1\Pi$ and $(2)^3\Sigma^+$ states can occur through the spin-orbit interaction H_{SO}. The nonvanishing matrix elements are[36] $\langle B^1\Pi(v'J)|H_{SO}|(2)^3\Sigma^+(vN(=J \text{ and } J\pm1)J)\rangle$. The rate of the predissociation is approximately proportional to the product of the Franck-Condon factor $|\langle v'|v\rangle|^2$ and the electronic-rotational

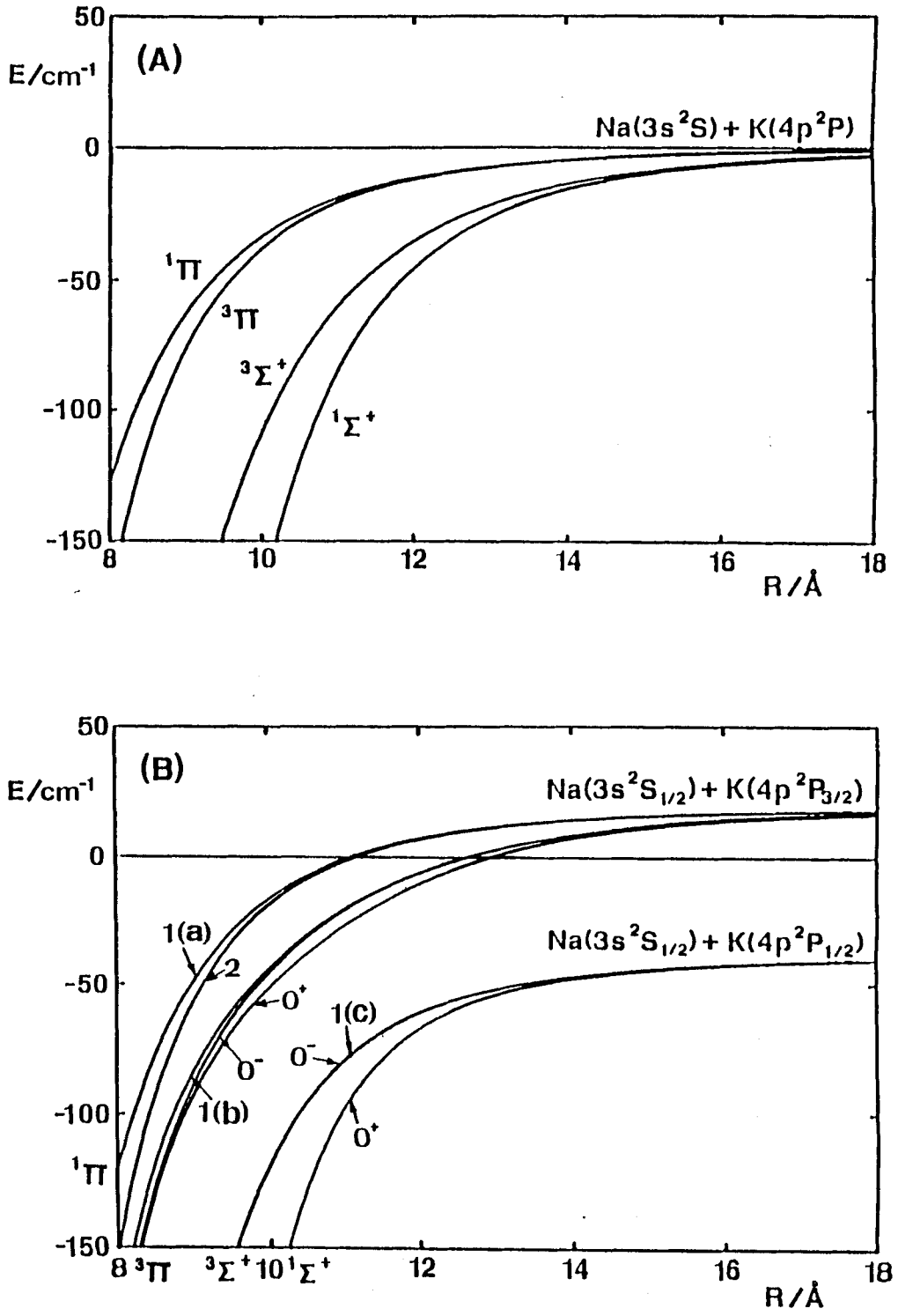

Fig. 11. Potential energy curves of NaK corresponding asymptote Na(3s) + K(4p). (A): Spin-orbit interaction is neglected. The C_{10} values for $^1\Pi$, $^3\Pi$, $^1\Sigma^+$, and $^3\Sigma^+$ states are, respectively, -0.5, 4.3, 48, and -18 $cm^{-1}Å^{10}$. (B): Spin-orbit interaction is included. The numbers are the values of Ω in Hund's case (c) notation, and a letter in ( ) is a symbol to distinguish each.

Table VIII. Eigenfunctions of 1(a, b, and c) states correlated with the separated atoms Na(3s) + K(4p), which are expressed as a linear-combination of the Hund's case (a) wave functions: $C_1|^3\Sigma^+_{\pm1}\rangle + C_2|^1\Pi_{\pm1}\rangle + C_3|^3\Pi_{\pm1}\rangle$.

State	R/Å	Energy/cm^{-1}	C_1	C_2	C_3
1(a)	10	-17.657	0.023	0.760	-0.650
	10.5	-8.141	0.019	0.742	-0.670
	11	-1.371	0.016	0.731	-0.682
	11.5	3.520	0.013	0.724	-0.689
	12	7.105	0.011	0.720	-0.694
	13	11.772	0.008	0.714	-0.700
	14	14.469	0.006	0.712	-0.702
	16	17.107	0.004	0.709	-0.705
	18	18.190	0.002	0.708	-0.706
	20	18.682	0.002	0.708	-0.706
1(b)	10	-45.203	0.383	0.594	0.708
	10.5	-32.089	0.475	0.583	0.660
	11	-21.666	0.557	0.560	0.614
	11.5	-13.314	0.623	0.533	0.572
	12	-6.657	0.673	0.508	0.538
	13	2.745	0.735	0.471	0.489
	14	8.547	0.767	0.447	0.460
	16	14.437	0.796	0.423	0.431
	18	16.890	0.807	0.415	0.420
	20	18.002	0.812	0.412	0.415
1(c)	10	-121.842	0.923	-0.265	-0.278
	10.5	-97.139	0.880	-0.330	-0.341
	11	-80.463	0.831	-0.389	-0.399
	11.5	-69.136	0.782	-0.437	-0.444
	12	-61.319	0.740	-0.473	-0.478
	13	-51.844	0.679	-0.518	-0.521
	14	-46.750	0.641	-0.542	-0.543
	16	-42.047	0.605	-0.563	-0.563
	18	-40.203	0.591	-0.571	-0.571
	20	-39.384	0.584	-0.574	-0.574

factor $|\langle B^1\Pi(J)|H_{SO}|(2)^3\Sigma^+(N(=J \text{ and } J\pm1)J)\rangle|^2$. From the variation of the linewidth with v' [see Fig. 10], the $(2)^3\Sigma^+$ potential curve probably crosses the $B^1\Pi$ curve near the left turning point of the $B^1\Pi(v'=34)$ level. For such a crossing, we can expect on Franck-Condon considerations a very rapid rise of the predissociation just before the crossing and a gradual falling off at higher v'. We conclude that the remarkable line broadenings at $v' \geq 33$ occur through the predissociation to $Na(3s^2S_{1/2})$ + $K(4p^2P_{1/2})$ atoms, the predissociation is caused by a strong spin-orbit interaction between the $B^1\Pi$ and $(2)^3\Sigma^+$ states, and the potential curves cross around the inner turning point of the $B^1\Pi(v'=34)$ level.

Chapter 4. DOPPLER-FREE OPTICAL-OPTICAL DOUBLE RESONANCE POLARIZATION SPECTROSCOPY FOR HIGHLY EXCITED STATES OF THE $^{23}Na^{39}K$ MOLECULE

Rydberg states of the homonuclear alkali metal diatomic molecules Li_2[10,37,38], Na_2[9,39], and K_2[40,41] have been studied for many years, but the Rydberg states or highly excited states of the heteronuclear NaK molecule have not yet been reported. Density of the electronic states is very high at the high energy region and many transition lines can be overlapped. A Doppler-free OODR polarization spectroscopy is a very useful technique for studying the highly excited states. The spectrum is simplified, because transitions only from a chosen vibrational-rotational level can be observed.

The highly excited states of the NaK molecule were observed by using a technique of the Doppler-free OODR polarization spectroscopy. By choosing the $B^1\Pi$ state as an intermediate state, the stepwise excitation allows to excite to the highly excited $^1\Sigma^+$, $^1\Pi$, and $^1\Delta$ states. The scheme of the stepwise excitation $^1\Delta(v, J) \leftarrow B^1\Pi(v', J') \leftarrow X^1\Sigma^+(v''=0, J'')$ is shown in Fig. 12. Four $^1\Sigma^+$, three $^1\Pi$, and five $^1\Delta$ states were observed in the energy regions 33016~33674 cm^{-1} and 34449~34717 cm^{-1}, and the molecular constants were determined. In the observed OODR polarization spectra, many lines are found to deviate from the extrapolated values. Several types of the perturbation between closely lying electronic states were found. These results are reported in this chapter.

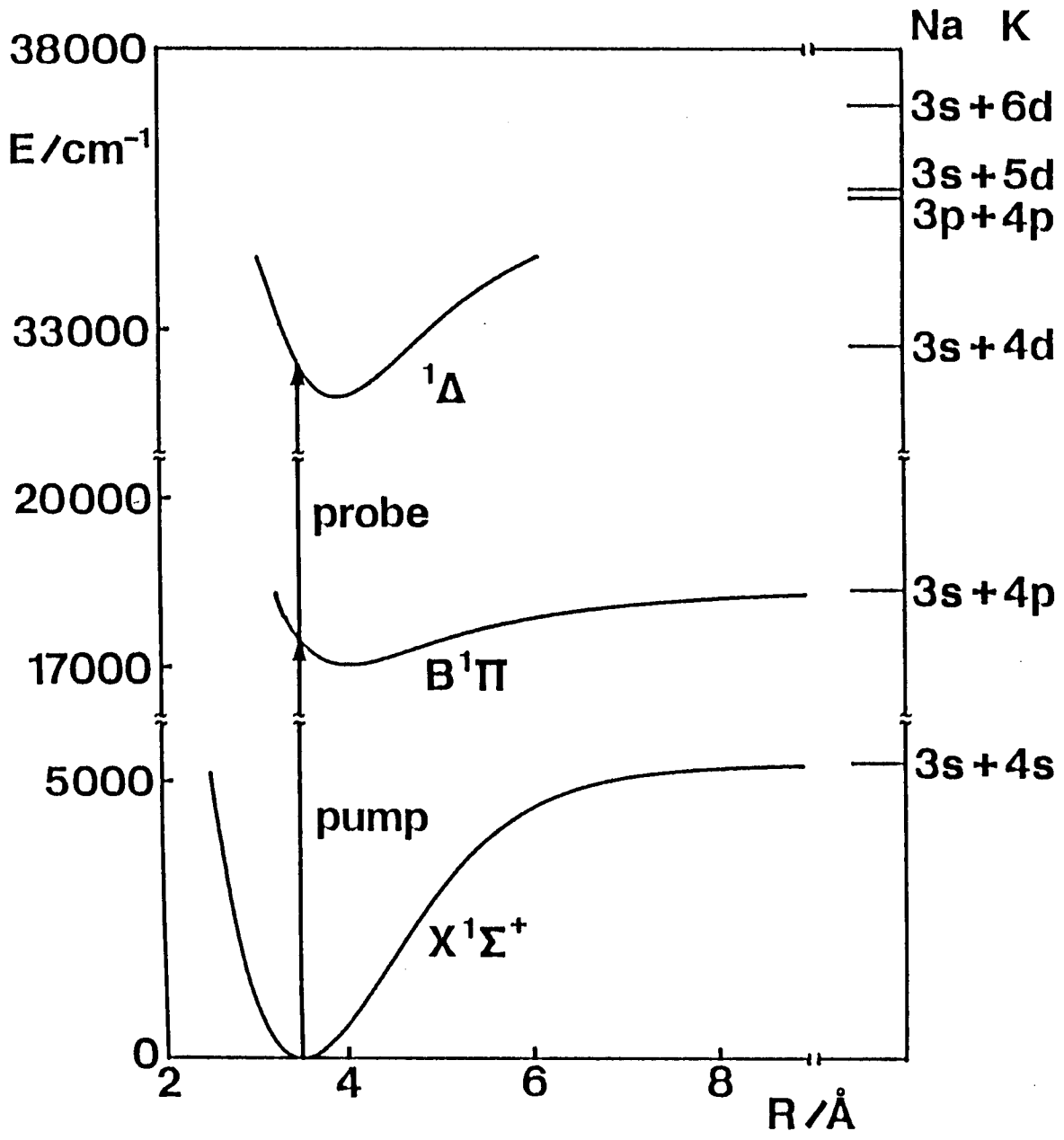

Fig. 12. A scheme of the OODR stepwise excitation to study highly excited states.

4.1 Experimental

The details and experimental arrangement of the OODR polarization spectroscopy is described in Chapter 2 and 3.1. In case of a stepwise excitation of the NaK molecule, the pump laser (Coherent CR699-21, operated by Rhodamin 6G dye) is tuned to a center of Doppler profile of a known transition $B^1\Pi(v', J') \leftarrow X^1\Sigma^+(v"=0, J")$ and the wavenumber is fixed. The probe laser (Coherent CR699-29, operated by Kiton Red or Rhodamine 6G dye) is scanned through the spectral range of transitions to the highly excited levels R(v, J) from the intermediate $B^1\Pi$ (v', J') level.

When two transition lines are accidentally located within the Doppler width of the pump transition, they are simultaneously excited and two intermediate levels are populated. In such case, another OODR spectrum was measured by changing the pump transition. For an example, if the P(J'+1) line is overlapped with the other line, the R(J'-1) line is selected as the pump line. By comparing the term values of the R(v, J') level obtained from the P(J'+1) and R(J'-1) lines, we can confirm that the assignment of the P(J'+1) line.

4.2 Determination of the Molecular Constants of Highly Excited States of the $^{23}Na^{39}K$ Molecule

4.2.1 Assignment of the Observed Transition Lines

From the $B^1\Pi$ state, $^1\Sigma^+$, $^1\Sigma^-$, $^1\Pi$, and $^1\Delta$ states can be excited by an electric dipole transition. The electronic state excited by the OODR stepwise excitation can be assigned from the spectral patterns of the OODR polarization spectrum. From the

selection rules for a electronic dipole transition [Eq. (3.1)-(3.5)] and the relative intensities calculated by the Hönl-London factor $S(\Lambda_1 J_1 \leftarrow \Lambda J)$ [in Table III] and the polarization factor ζ^{C} (or ^{L})$(J_1 \leftarrow J, J_2 \leftarrow J_1)$ [in Table II]. The allowed transitions at large J are schematically shown in Fig. 13. When a circularly polarized pump beam is tuned to a P or R line, P and R lines can be detected as the Lorentian shaped lines of different signs for the $^1\Sigma^+ \leftarrow {}^1\Pi$, $^1\Pi \leftarrow {}^1\Pi$, and $^1\Delta \leftarrow {}^1\Pi$ transitions. If the polarization of the pump beam is elliptical, Q lines can also be detected as a dispersed lines for the $^1\Sigma^- \leftarrow {}^1\Pi$ and $^1\Delta \leftarrow {}^1\Pi$ transitions. On the other hand, when a linearly polarized pump beam, of which polarization plane is chosen to be 45° against the probe polarization, is tuned to a Q line, Q lines can be detected for the $^1\Sigma^+ \leftarrow {}^1\Pi$ and $^1\Delta \leftarrow {}^1\Pi$ transitions, and weak P and R lines can also be detected for the $^1\Sigma^- \leftarrow {}^1\Pi$, $^1\Pi \leftarrow {}^1\Pi$, and $^1\Delta \leftarrow {}^1\Pi$ transitions. Note that the Q line of the $^1\Pi \leftarrow {}^1\Pi$ transition can be detected at only small J, because the intensity is proportional to $1/J^2$ as we can see the Hönl-London factor. [Table III]

In the observed region, several $^1\Sigma^+$, $^1\Pi$, and $^1\Delta$ states, except $^1\Sigma^-$ state, could be observed and assigned. The observed spectral lines, which are assigned as the $^1\Sigma^+ \leftarrow {}^1\Pi$, $^1\Pi \leftarrow {}^1\Pi$, and $^1\Delta \leftarrow {}^1\Pi$ transitions are shown, respectively, in Fig. 14(a), (b), and (c). The upper trace (A) represents the OODR polarization signals which were observed when the circularly polarized pump beam was tuned to the $B^1\Pi(v'=9, J'=30e) \leftarrow X^1\Sigma^+(v''=0, J''=31e)$ transition [P(31) line]. The lower trace (B) represents the ones which were observed when the linearly polarized pump beam was

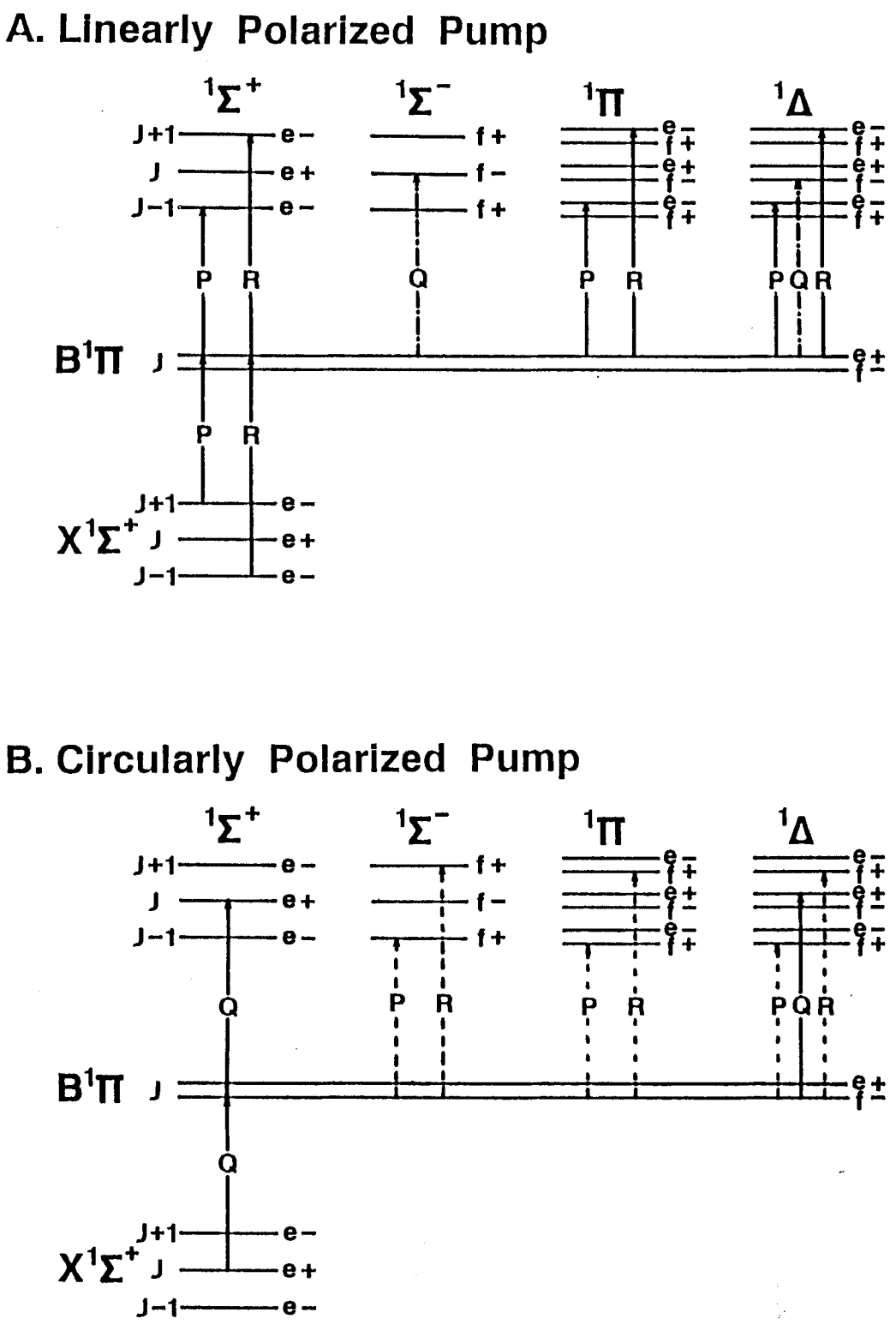

Fig. 13. Spectral patterns of the OODR polarization spectrum with circularly polarized pump beam tuned to P or R line (A), and linearly polarized pump beam tuned to Q line (B). A dotted-broken line in (A) is for the dispersion shaped signal, and a broken line in (B) is for the weak intensity signal.

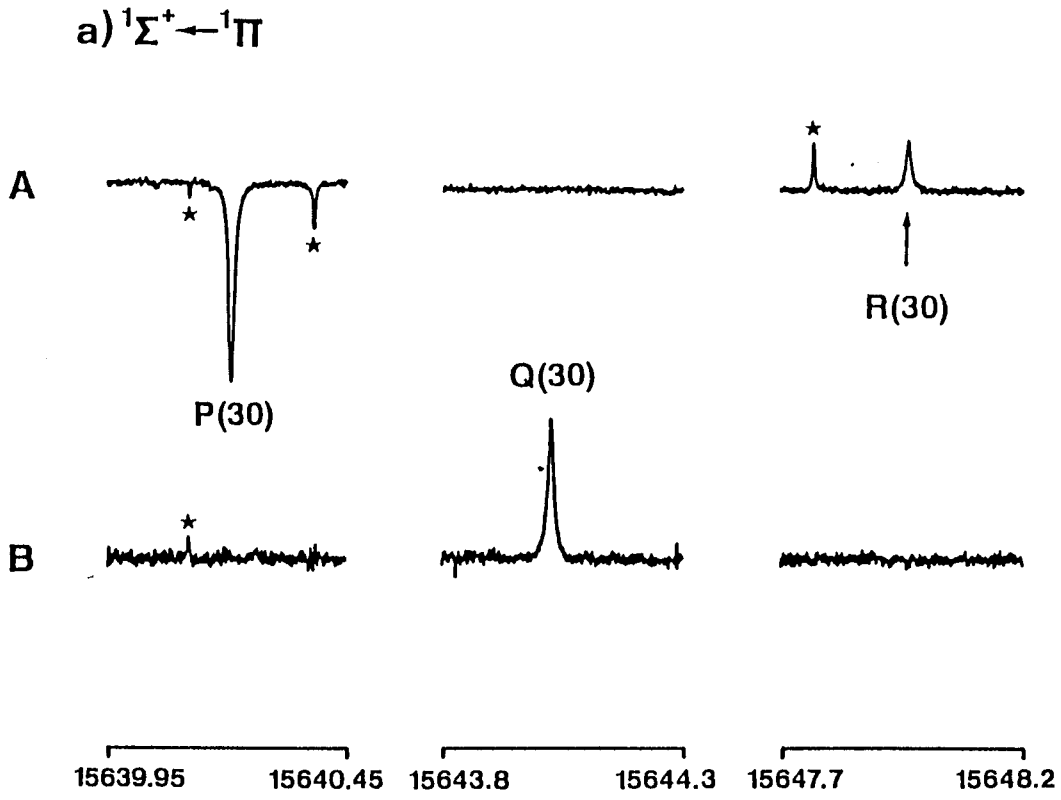

Fig. 14. A part of the OODR polarization signals. (a), (b), and (c) are the $^1\Sigma^+$ - $B^1\Pi$, $^1\Pi$ - $B^1\Pi$, and $^1\Delta$ - $B^1\Pi$ transition lines. Upper trace (A): a circularly polarized pump beam was tuned to the $B^1\Pi(v'=9, J'=30e)$ - $X^1\Sigma^+(v''=0, J''=31e)$ transition; lower trace (B): a linearly polarized pump beam was tuned to the $B^1\Pi$ $(v'=9, J'=30f)$ - $X^1\Sigma^+(v''=0, J''=30e)$ transition. Lines with ★ originated from other types of the OODR transitions.

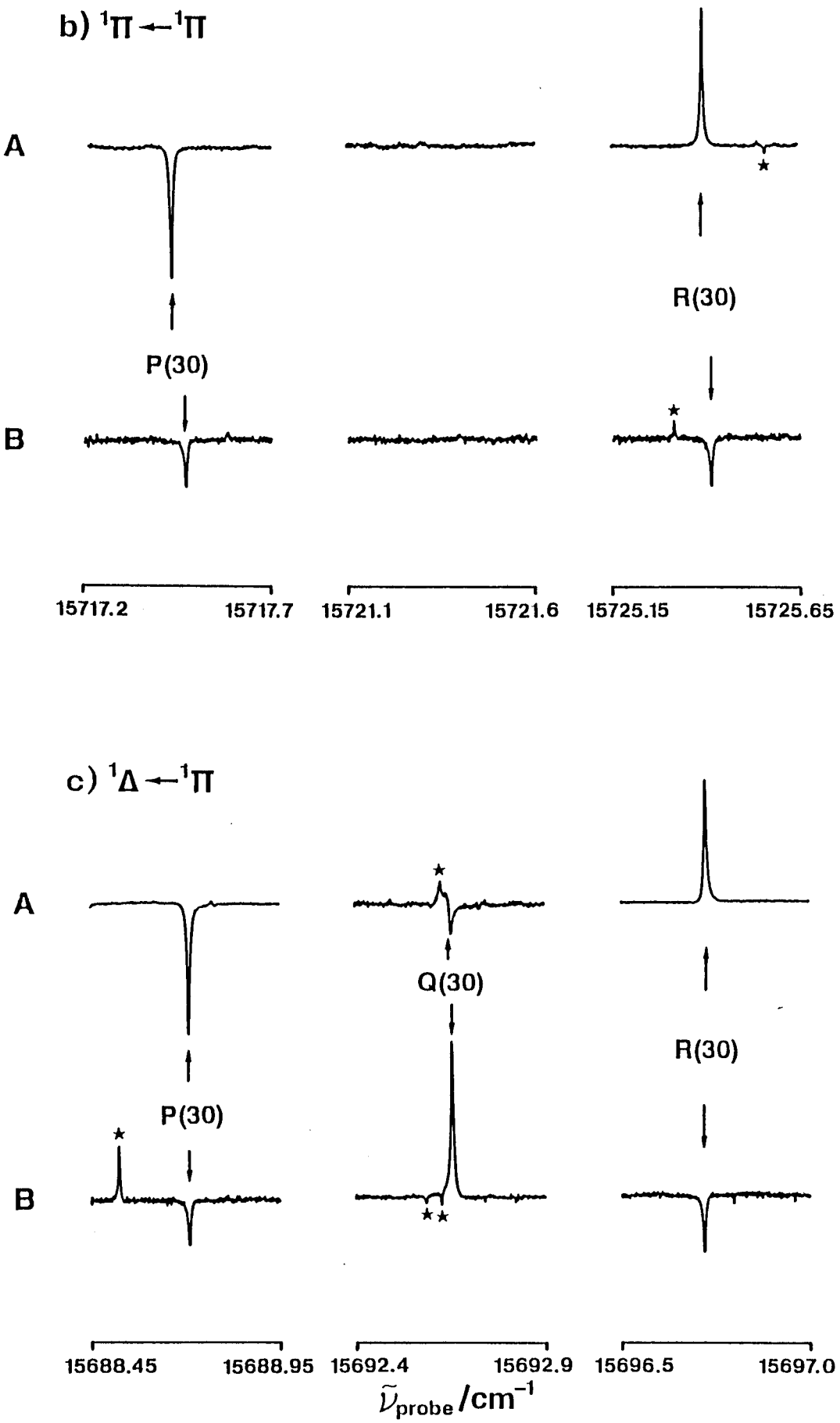

Fig. 14. (Continued)

tuned to the $B^1\Pi(v'=9, J'=30f) \leftarrow X^1\Sigma^+(v''=0, J''=30e)$ transition [Q(30) line].

A part of the OODR polarization spectrum which contains the $^1\Delta(v, J=29e, 30f,$ and $31e) \leftarrow B^1\Pi(v'=9, J'=30e)$ and $^1\Sigma^+(v, J=29e) \leftarrow B^1\Pi(v'=9, J'=30e)$ transitions is shown in Fig. 15. In this case, the $B^1\Pi(v'=9, J'=30e) \leftarrow X^1\Sigma^+$ $(v''=0, J''=31e)$ transition was chosen as the pump transition by a circularly polarized pump beam. In addition to the lines of the sequential two photon absorption, many extra lines are observed, as we can see in Fig. 15. The extra lines in Fig. 15 are assigned as the transitions to the levels of the $B^1\Pi$ and $C^1\Sigma^+$ states from the $X^1\Sigma^+(v'', J''=29e$ and $31e)$ levels populated by the radiative transitions $B^1\Pi(v'=9, J'=30e) \rightarrow X^1\Sigma^+(v'', J=29e$ and $31e)$. [see Fig. 1(d)] Since the molecular constants of the NaK $X^1\Sigma^+$, $B^1\Pi$ and $C^1\Sigma^+$ states are known,[17,16,42] these extra lines can be easily assigned from the combination difference of the P(J+1) and R(J-1) lines.

The energy region of 33016~33674 cm^{-1} above the potential minimum of the ground state could be studied when the $B^1\Pi(v'=9, J'e/f) \leftarrow X^1\Sigma^+(v''=0, J''e)$ transitions (mainly J'=30-40) were chosen as the pump transitions, and more than 400 rotational levels of the highly excited states were observed. Among them, 215 levels were assigned to $^1\Delta$ states, 21 levels to $^1\Pi$ states, and 106 levels to $^1\Sigma^+$ states. From the rotational constants B_v and the vibrational spacings ΔG_v, the observed lines were attributed to three $^1\Sigma^+$, two $^1\Pi$ and three $^1\Delta$ states. The molecular constants will be reported in the next section. The progression of the vibrational levels could be found in two $^1\Delta$ states

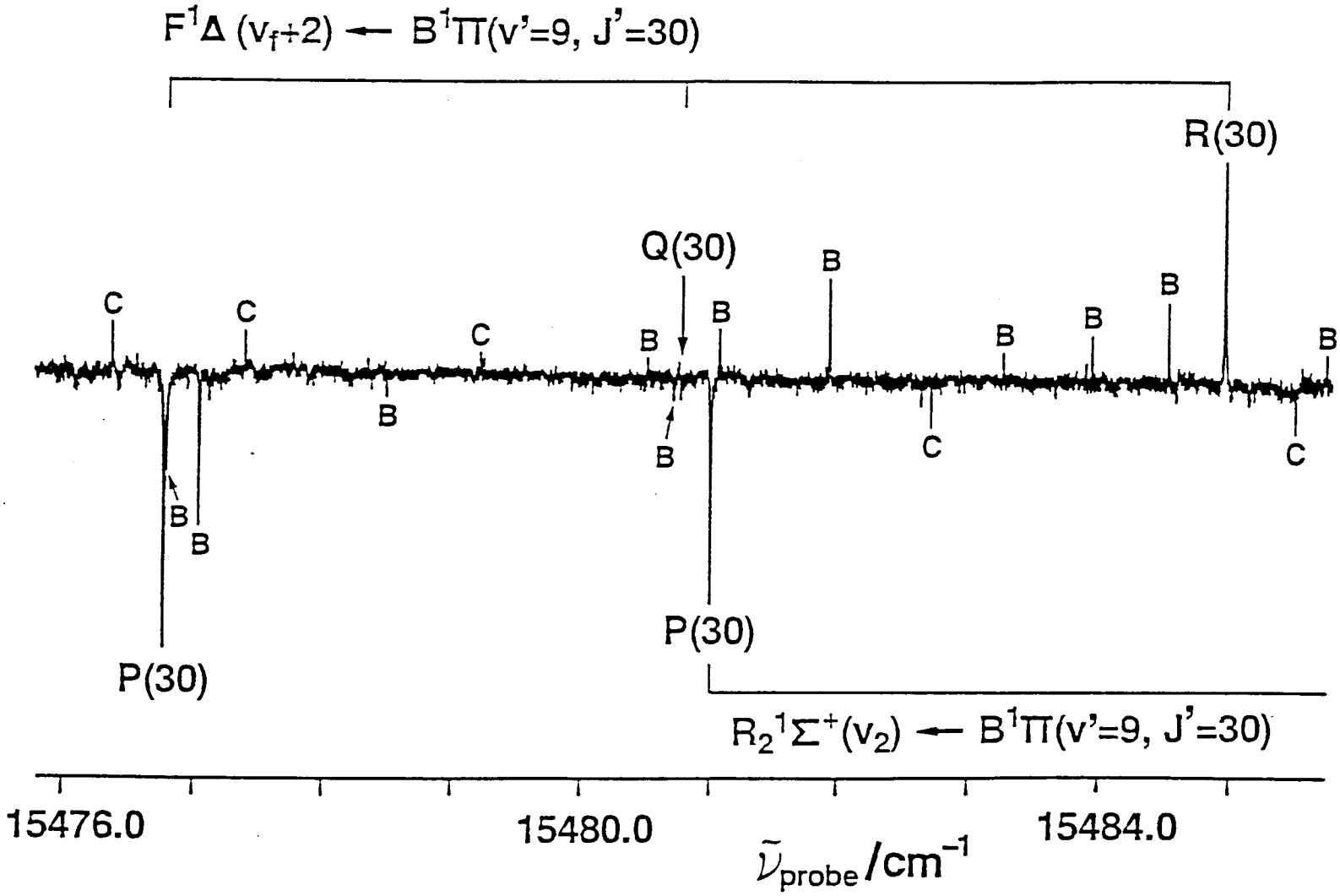

Fig. 15. A part of the OODR polarization spectrum, where the $B^1\Pi(v'=9, J'=30e) - X^1\Sigma^+(v''=0, J''=31e)$ transition is used as the pump transition. The extra lines with B and C originated from $B^1\Pi - X^1\Sigma^+$ and $C^1\Sigma^+ - X^1\Sigma^+$ transitions, respectively.

and three $^1\Sigma^+$ states. These states are notated as the $F^1\Delta$, $G^1\Delta$, $H^1\Sigma^+$, $I^1\Sigma^+$, and $J^1\Sigma^+$.

The energy region of 34449-34717 cm^{-1} above the potential minimum of the ground state could be studied when the $B^1\Pi$(v'=6, J'*e/f*) ← $X^1\Sigma^+$(v"=0, J"*e*) transitions (J'=18, 20, and 22) were chosen as the pump transitions, and 32 rotational levels were assigned to two $^1\Delta$ states, one $^1\Pi$ state, and one $^1\Sigma^+$ state. The progression of the vibrational levels could be found in only one $^1\Delta$ state. This state is notated as the $K^1\Delta$ state. The excited states which were observed at only one vibrational level are noted as the R_n (n=1~6) in order of the energy.

The assignment of J were easy because the intermediate level of known J' were chosen by the pump laser. But the vibrational numberings are difficult and the estimate will be discussed in the next section.

4.2.2 Molecular Constants of Highly Excited State and the Potential Energy Curve of the $G^1\Delta$ State

The term energy is expressed by Eq. (1.3) and (1.4). From the term energy of the observed transition lines, the molecular constants E_v^0, B_v, and D_v of the observed highly excited states were determined by a least-squares-fitting procedure. The obtained molecular constants of the $^1\Delta$ states and others are listed, respectively, in Table IX and X. The vibrational quantum number v_f, v_g, •••, in Table IX and X represent the lowest observed level of the F, G, •••, state, respectively. The energy E_v^0 of the assigned levels are schematically shown in Fig. 16 and 17.

Table IX. Molecular constants E^0_v, B_v and D_v of the NaK F, G, and $K^1\Delta$ states. All values are in units of cm^{-1}. N is the number of rotational energy levels used to determine the constants. J_{min} and J_{max} are the minimum and maximum rotational quantum number used to determine the constants.

state	v	E^0_v	10^2B_v	10^7D_v	N(J_{min}, J_{max})
$F^1\Delta$	v_f	32877.147	6.7452	—	2 (39, 41)
	v_f+1	32958.209	6.7750	2.0905	10 (29, 42)
	v_f+2	33039.174	6.7401	2.4856	9 (29, 42)
	v_f+3	33119.716	6.6976	2.2599	30 (2, 41)
	v_f+4	33200.233	6.6524	2.0065	11 (27, 43)
$G^1\Delta$	11	32909.318	6.9904	—	3 (37, 41)
	12	32997.827	6.8010	1.8663	7 (29, 41)
	13	33084.295	6.7363	1.4801	8 (29, 42)
	14	33169.183	6.6811	1.9249	6 (29, 41)
	15	33252.134	6.6272	3.3997	14 (27, 41)
	16	33335.759	6.2787	-5.3069(a)	6 (31, 41)
	17	33411.516	6.4805	2.2898	4 (29, 41)
	18	33488.808	6.4041	1.5432	4 (29, 41)
	19	33565.825	6.2364	—	2 (39, 41)
$K^1\Delta$	v_k	34518.842	6.8369	1.3211	5 (17, 23)
	v_k+1	34604.184	6.7906	0.8789	5 (17, 23)
	v_k+2	34688.856	6.7491	—	2 (17, 19)

(a) The anomalous values may be originating from the perturbation.

Table X. Molecular constants E^0_v, B_v and D_v of the NaK $^1\Sigma^+$, $^1\Pi$, $^1\Delta$ states. All values are in units of cm^{-1}. N is the number of rotational energy levels used to determine the constants. J_{min} and J_{max} are the minimum and maximum rotational quantum number used to determine the constants.

state	v	E^0_v	10^2B_v	10^7D_v	N(J_{min}, J_{max})
$H^1\Sigma^+$	v_h	32951.694	6.4095	1.5405	8 (29, 41)
	v_h+2	33123.350	6.3816	4.2940	41 (9, 48)
	v_h+3	33206.686	6.2457	1.6150	8 (29, 43)
$I^1\Sigma^+$	v_i	33044.409	6.6032	3.2224	7 (29, 42)
	v_i+1	33127.937	6.4000	-8.6281(a)	20 (17, 41)
$J^1\Sigma^+$	v_j	33161.873	6.4517	-4.3626(a)	6 (29, 41)
	v_j+2	33333.544	6.5550	1.1833	9 (31, 41)
$R_1{}^1\Delta$	v_1	33108.476	6.4865	2.2990	9 (29, 41)
$R_2{}^1\Pi$	v_2	33143.131	6.5939	1.5362	8 (27, 41)
$R_3{}^1\Pi$	v_3	33281.128	6.5773	3.5670	8 (29, 41)
$R_4{}^1\Sigma^+$	v_4	34510.430	6.3692	-8.8132(a)	5 (17, 23)
$R_5{}^1\Pi$	v_5	34529.425	6.6621	3.6313	4 (17, 23)
$R_6{}^1\Delta$	v_6	34592.702	6.5642	—	2 (17, 19)

(a) The anomalous values may be originating from the perturbation.

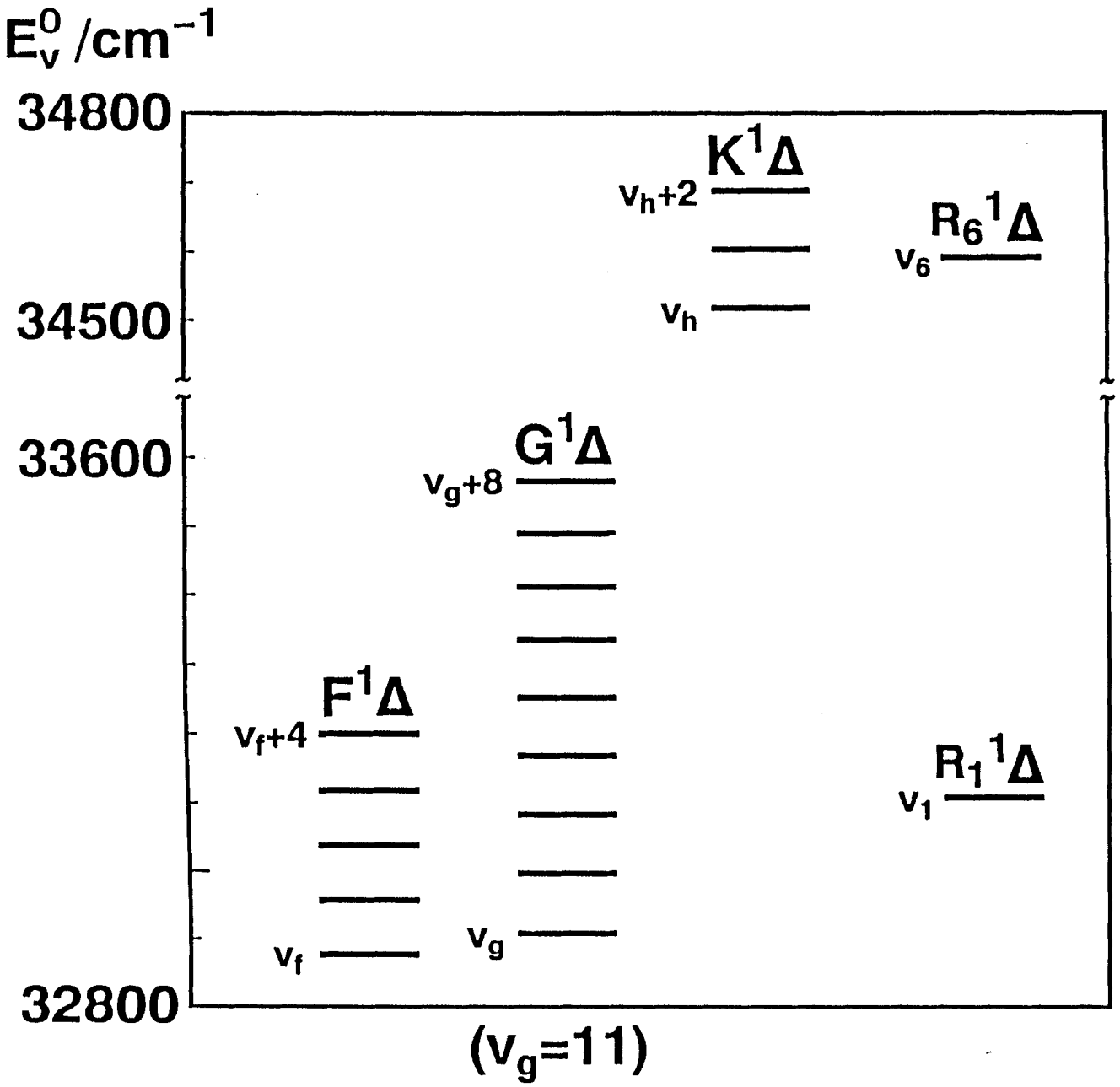

Fig. 16. The vibrational level energies (E_v^o) of the observed $^1\Delta$ states.

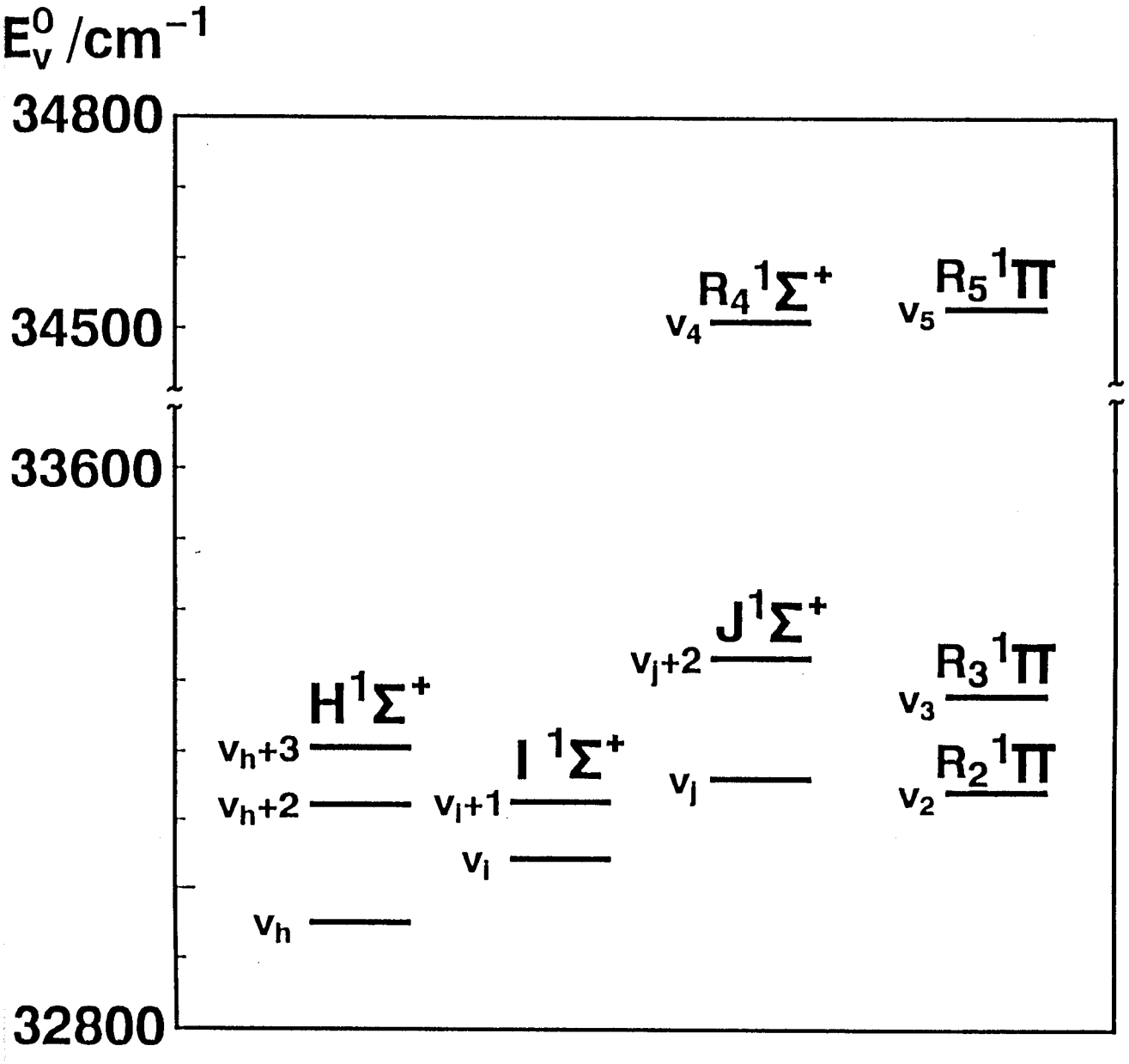

Fig. 17. The vibrational level energies (E_v^o) of the observed $^1\Sigma^+$ and $^1\Pi$ states.

For the $G^1\Delta$ state, the progression of the vibrational levels could be found for v_g to v_g+8, where v_g is the vibrational quantum number of the lowest observed level of the $G^1\Delta$ state. The assignment of the vibrational quantum number is possible if the dispersed fluorescence is observed. However, we could not observe the fluorescence spectra from the $G^1\Delta$ state. The $^1\Delta$ state cannot directly radiate to the lower $A^1\Sigma^+$ or $X^1\Sigma^+$ state. The fluorescence to the $B^1\Pi$ state cannot be distinguished from the fluorescence originated from the pump or probe transition.

Recently, Bautista et. al.[43] reported a method todetermine the vibrational quantum numbers by a simple algebraic procedure. By applying this method, we estimated as v_g=10 or 11, and v_f≈20. From the estimated v value and the molecular constants in Table IX, we calculated the Dunham coefficients $Y_{i,j}$(j=0 and 1)[16] for the $G^1\Delta$ state :

$$E_v^0 - T_e - 4B_v = \sum_{i=0,1,2} Y_{i0}(v + 1/2)^i \qquad (4.1)$$

$$B_v = \sum_{i=0,1,2} Y_{i1}(v + 1/2)^i. \qquad (4.2)$$

From the Dunham coefficients Y_{i0} and Y_{i1} obtained above, the potential energy curve of the $G^1\Delta$ state was calculated by the RKR method.[20,21] And then, we calculated the Frank-Condon factors of the $G^1\Delta(v) \leftarrow B^1\Pi(v'=9)$ transitions. These procedures were performed for several v values around the v_g=10. From the comparison between the calculated Frank-Condon factors and the intensity pattern of the observed OODR signals, we have determined v_g to be 11. The resulting Dunham coefficients and the RKR turning points for the $G^1\Delta$ state are listed, respectively, in Table XI and XII. The rotationless potential energy curve is

Table XI. Dunham coefficients for the NaK $G^1\Delta$ state. All value given by cm^{-1}.

T_e	31761.70	Y_{01}	7.62861×10^{-2}
Y_{10}	110.209	Y_{11}	-6.56598×10^{-4}
Y_{20}	-9.0764×10^{-1}		

Table XII. RKR potential energy curve of NaK $G^1\Delta$ state. R_{min} and R_{max} are turning points at the each vibrational value. R_e is the equilibrium internuclear distance.

v	V(R)/cm^{-1}	R_{min}/Å	R_{max}/Å
		R_e = 3.9095	
-0.25	27.8029	3.8113	4.0159
0.	54.8307	3.7719	4.0637
1.00	163.2244	3.6801	4.1892
2.00	269.8029	3.6207	4.2827
3.00	374.5660	3.5746	4.3635
4.00	477.5139	3.5361	4.4371
5.00	578.6464	3.5027	4.5061
6.00	677.9637	3.4729	4.5721
7.00	775.4657	3.4459	4.6357
8.00	871.1524	3.4212	4.6977
9.00	965.0238	3.3983	4.7585
10.00	1057.0800	3.3768	4.8183
11.00	1147.3208	3.3566	4.8776
12.00	1235.7464	3.3375	4.9364
13.00	1322.3567	3.3192	4.9950
14.00	1407.1517	3.3018	5.0535
15.00	1490.1314	3.2850	5.1121
16.00	1571.2958	3.2689	5.1709
17.00	1650.6450	3.2531	5.2299
18.00	1728.1788	3.2378	5.2893
19.00	1803.8974	3.2229	5.3492
20.00	1877.8007	3.2084	5.4097
21.00	1949.8886	3.1941	5.4709
22.00	2020.1614	3.1800	5.5329
23.00	2088.6188	3.1661	5.5957
24.00	2155.2609	3.1524	5.6595
25.00	2220.0878	3.1388	5.7243
26.00	2283.0993	3.1252	5.7904
27.00	2344.2956	3.1116	5.8577
28.00	2403.6766	3.0980	5.9263
29.00	2461.2423	3.0844	5.9966
30.00	2516.9927	3.0707	6.0684

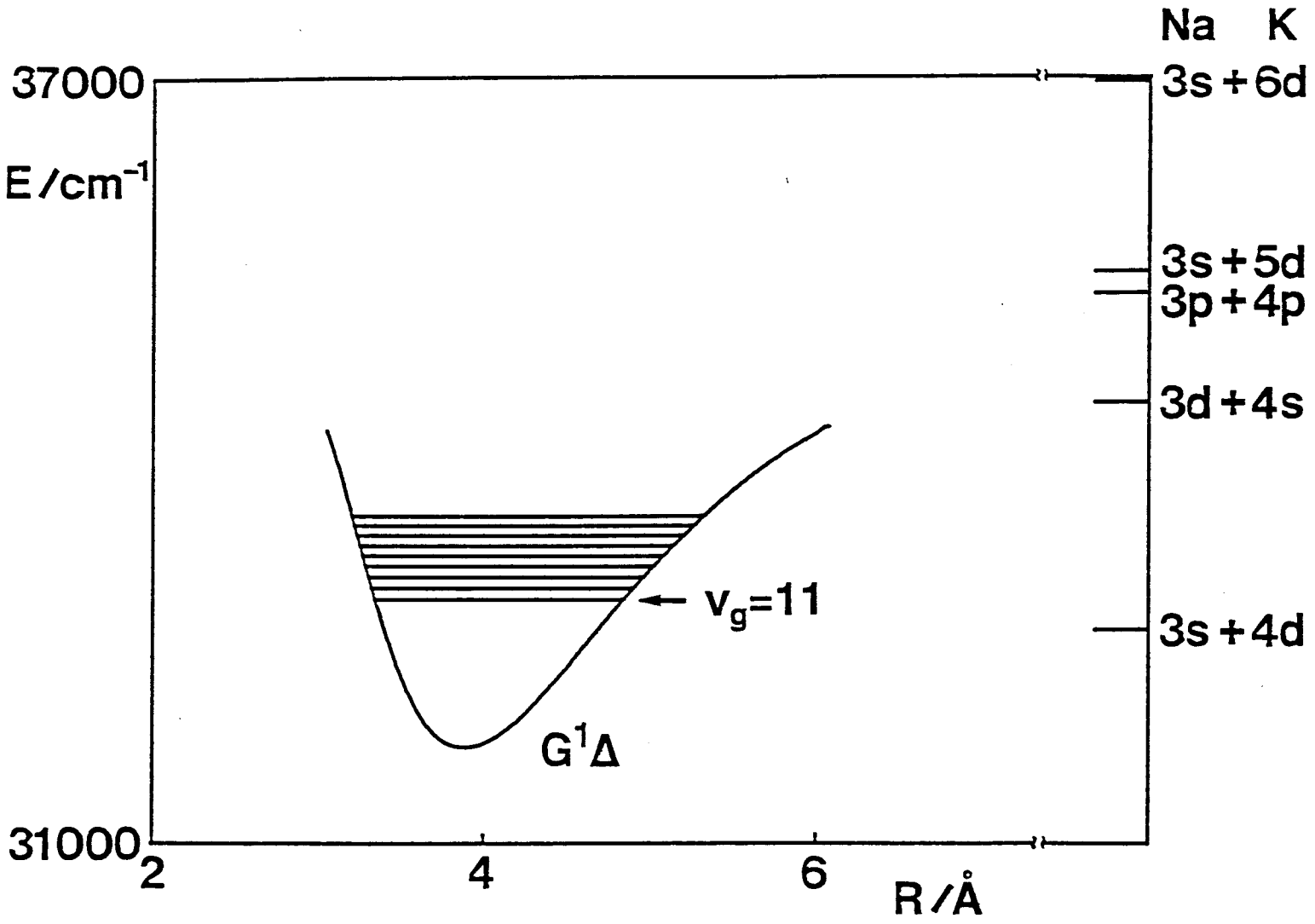

Fig. 18. The rotationless RKR potential energy curve of the NaK $G^1\Delta$ state. The horizontal lines show the observed vibrational levels.

shown in Fig. 18.

Starting from the intermediate $B^1\Pi$ state, which dissociates to the Na(3s) + K(4p) atoms, only the transitions involving the K(4p) electron have appreciable transition probability to states correlated with the atomic asymptote Na(3s) + K(ns) and Na(3s) + K(nd). Similarly, transitions involving the Na(3s) electron can lead to doubly excited states arising from the atomic asymptote Na(np) + K(4p). The possible atomic asymptotes of the $G^1\Delta$ state are shown in Fig. 18. Stevens et. al.[35] calculated the potential curves for the three $^1\Delta$ states correlated with the Na(3s) + K(3d), Na(3d) + K(4s), and Na(3p) + K(4p) atomic asymptote by the full-valence configuration interaction computations. The molecular constants of the $^1\Delta$ states and the NaK^+ ion ground state $X^2\Sigma^+$ [44,45] are listed in Table XIII for comparison. The molecular constants of the calculated $^1\Delta$ state correlated with the atomic asymptote Na(3s) + K(3d) and the ones of the $G^1\Delta$ state are similar. It suggests the $G^1\Delta$ state may be correlated with the Na(3s) + K(nd). From the similarity of the constants, we assumed the $G^1\Delta$ state correlated with the atomic asymptote Na(3s) + K(5d).

As we can see from the Fig. 18, it is expected the doubly excited $^1\Delta$ state which is correlated with the atomic asymptote Na(3p) + K(4p) exists near the $G^1\Delta$ state. The strong electrostatic interaction between the Rydberg state and the doubly excited configuration were found in the Li_2[10] and Na_2[46] molecules. It is expected the NaK $G^1\Delta$ state interacts with the $^1\Delta$ state correlated with Na(3p) + K(4p), and the $G^1\Delta$ state is a mixture of the Rydberg state and a balence state.

Table XIII. The molecular constants of NaK $^1\Delta$ states and NaK^+ $X^2\Sigma^+$ ion ground state. T_e, ω_e, $\omega_e x_e$, and D_e values are in cm^{-1}. R_e is the equilibrium internuclear distance in Å.

state	asymptote	T_e	ω_e	$\omega_e x_e$	R_e	D_e
$^1\Delta$	Na(3s)+K(3d)[a]	23352	103.6	0.70	3.724	4076
$^1\Delta$	Na(3s)+K(4d)	—	—	—	—	—
$^1\Delta$	Na(3d)+K(4s)[a]	29905	72.8	0.30	4.178	4744
$^1\Delta$	Na(3p)+K(4p)[a]	35492	50.6	—	5.034	266[f]
$G^1\Delta$	Na(3s)+K(5d)[b]	31762	110.2	0.91	3.909	3699
		T_0	ω_e		R_e	D_0
$X^2\Sigma^+$	Na(3s)+ K^+ [c]	35620	—	—	—	4597
	[d]	34585	89.8	—	3.81	5632

a. Reference 35.

b. This work.

c. Reference 44.

d. Reference 45.

f. This state is metastably bound with respect to Na(3p)+K(4p).

For the $^1\Pi$ and $^1\Delta$ states, the difference of the term values of the R(v, J) levels excited by the circularly and linearly polarized pump beam gives the Λ-type splitting ΔE [see Fig. 13],

$$\Delta E = E_{v,Je} - E_{v,Jf} = q_v[J(J+1) - \Lambda^2], \qquad (4.3)$$

where q_v is the Λ doubling constants. The Λ-type doubling originates from the L-uncoupling interaction[18] between sufficiently distant two electronic states with $\Delta\Lambda = \pm 1$. Many rotational levels were found to irregular and deviates from the extrapolated values. It suggests the perturbations between closely lying electronic states. The obtained Λ-type splittings ΔE are found to be irregular in many parts. From the observed unperturbed lines, we estimated the q_v of the $F^1\Delta$ and $G^1\Delta$ states,

$F^1\Delta$ state : $q_v = 1.5 \times 10^{-5}$ cm^{-1},

$G^1\Delta$ state : $q_v = 0.5 \times 10^{-5}$ cm^{-1}.

The highly excited states, involving the Rydberg states, belong with respect to the angular momentum coupling to the intermediate range between the two limiting Hunt's coupling case (a) and (d).[11] In case (a) the electronic orbital angular momentum **L** is strongly coupled to the internuclear axis and its projection quantum number Λ is well defined. In case (d) **L** is completely decoupled from the axis of the rotating molecule and combines with the angular momentum **R** of the molecular rotation to form the resultant **N=R+L**. The relative small Λ-type splittings indicate that Λ is still a fairly good quantum number and Hund's case (a) coupling is a good approximation.

4.3 Perturbation between the highly excited states

From the analysis of the observed transition lines, many rotational levels were found to irregular and deviates from the extrapolated values. It suggests the perturbations between closely lying electronic states. The selection rules for perturbation between the electronic states are[11]

$$\Delta J = 0 \tag{4.4}$$

$$+ \leftrightarrow + \text{ and } - \leftrightarrow - \quad (e \leftrightarrow e \text{ and } f \leftrightarrow f) \tag{4.5}$$

$$\Delta S = 0, \pm 1 \tag{4.6}$$

$$\Delta \Lambda = 0, \pm 1. \tag{4.7}$$

If the perturbation occurs between two levels, the higher level is displaced upward and the lower level downward by an equal amount, and the smaller the separation between the levels the larger are their shifts.

For the spectral range of the $F^1\Delta(v=v_f+3) \leftarrow B^1\Pi(v'=9)$ and $H^1\Sigma^+(v=v_h+2) \leftarrow B^1\Pi(v'=9)$ transitions, the OODR polarization spectrum was observed. The intermediate $B^1\Pi(v'=9$, $J'=1\sim60e$ and several $J'f$) levels were chosen by the pump laser. By using the OODR technique, only a pair of the mutual perturbing levels could be observed. The observed line positions (in cm^{-1}) for each intermediate $J'e$ levels are schematically shown in Fig. 19 (similar to Fortrat diagram[11]), where the only Q lines of the $F^1\Delta(v=v_f+3$, $Jf) \leftarrow B^1\Pi(v'=9$, $Je)$ transition are the transitions to f levels, and others are the ones to e levels. [see Fig. 13(A)] In addition to the expected transition lines to the $F^1\Delta(v=v_f+3)$ and $H^1\Sigma^+(v=v_h+2)$ levels, other transition lines, which are represented by □ and Δ in Fig. 19, could be observed

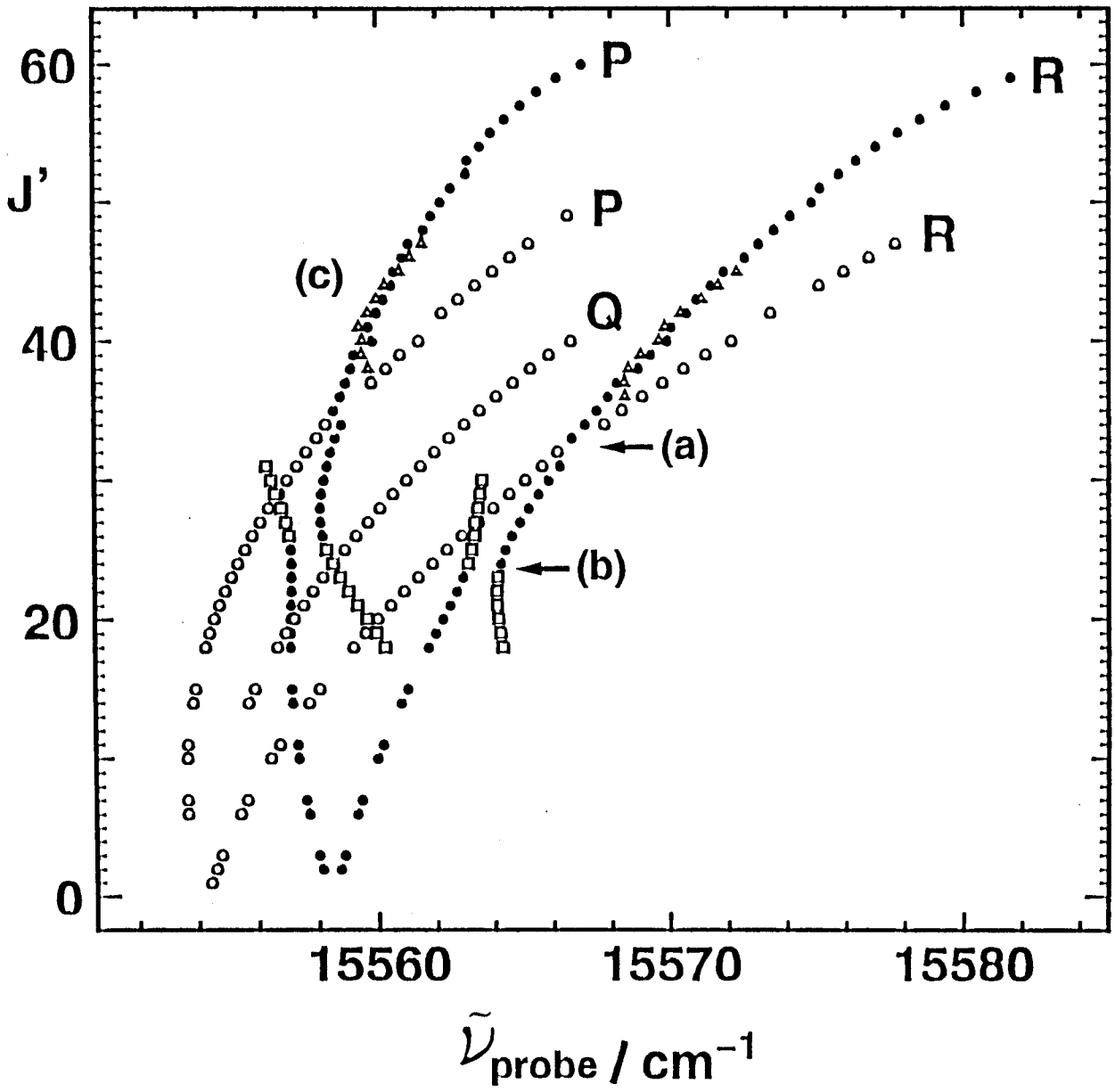

Fig. 19. The observed line positions against to intermediate J'e value. [Fortrat diagram] o is shown a transition to the $F^1\Delta$ state, • to $H^1\Sigma^+$ state, □ to U-state, and Δ to T-state. The regions of the irregular line positions are represented by (a), (b), and (c).

only at the place the interaction occurs with $H^1\Sigma^+$ state. Here we shall call these interacting states as "U" state (for lines with □) and "T" state (for lines with Δ), respectively. There are three regions of the irregular line positions, and these are shown as (a), (b), and (c) in Fig. 19.

(a) is due to the perturbation between the $F^1\Delta(v=v_f+3)$ and $H^1\Sigma^+(v=v_h+2)$ states. The deviations from the expected values were found only for *e* levels. The molecular constants of the $F^1\Delta(v=v_f+3)$ state are determined from *f* levels and listed in Table IX. The differences between the measured term values and the values calculated from the molecular constants are shown in Fig. 20. The largest energy shift of the $F^1\Delta(v=v_f+3)$ levels is about 0.2 cm^{-1} at J=34. From the direction and the magnitude of the energy shifts, the rotational level of the $F^1\Delta(v=v_f+3)$ and $H^1\Sigma^+(v=v_h+2)$ state is expected to cross at J_c=34. However, as we can see from the Eq. (4.7), the $^1\Delta$ state cannot directly interact to $^1\Sigma^+$ state. A possible state which perturbs with both a $^1\Delta$ and $^1\Sigma^+$ state is a $^1\Pi$ state. Both of the $^1\Delta \sim {}^1\Pi$ and $^1\Pi \sim {}^1\Sigma^+$ perturbation can be induced by L-uncoupling interaction;[18]

$$H_{JL} = - B(J_+L_- + J_-L_+), \qquad (4.8)$$

where $B = \hbar^2/2\mu R^2$, μ is the reduced mass. J is the total angular momentum and L is the electronic orbital angular momentum. $J_\pm = J_x \pm iJ_y$ and $L_\pm = L_x \pm iL_y$, where x and y denote the molecule-fixed coordinates with the z axis coinciding the internuclear axis. The nonbanishing matrix elements between the $^1\Delta(v, Je)$ and $^1\Pi$ state, and between the $^1\Sigma^+(v, Je)$ and $^1\Pi$ state are given by[47]

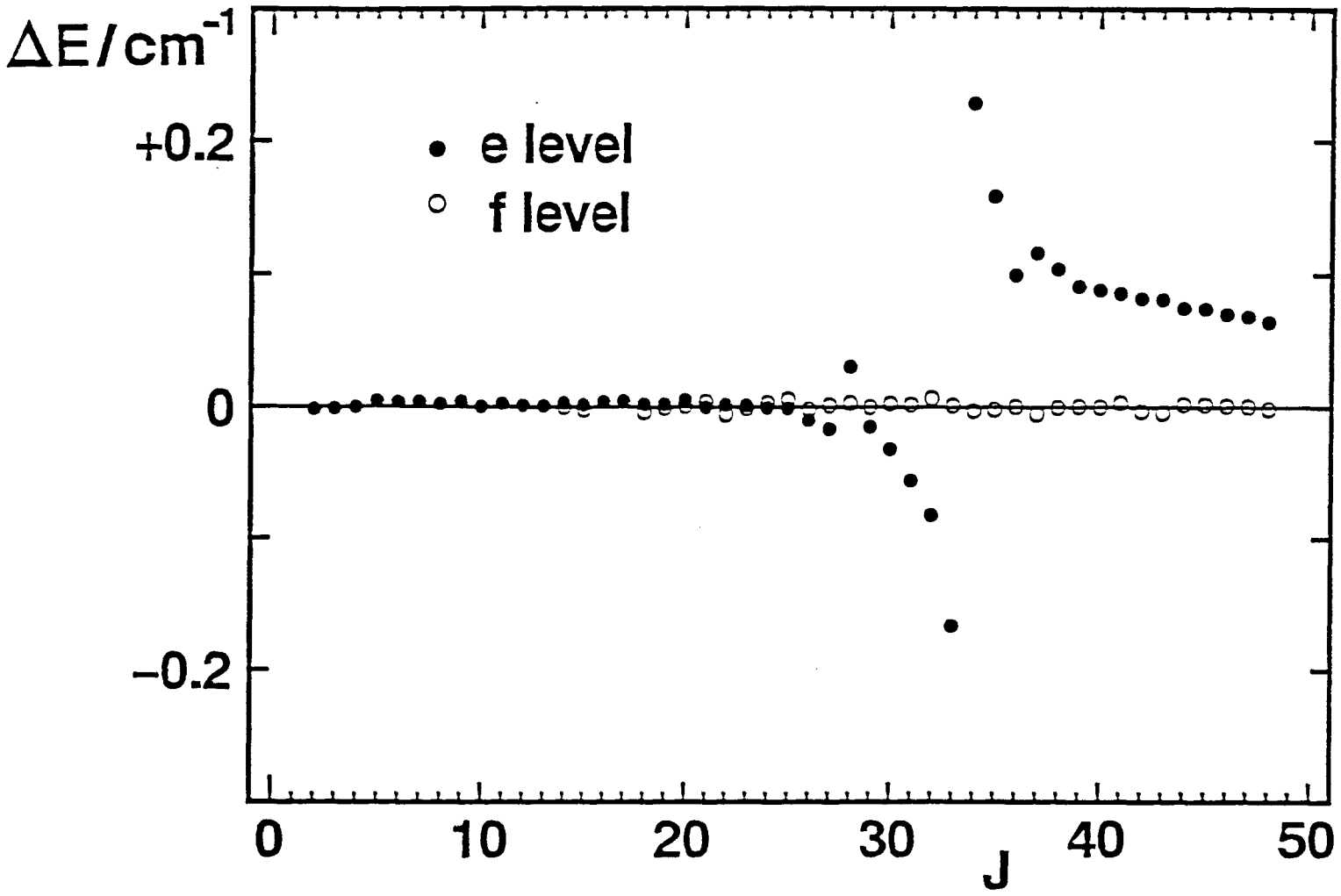

Fig. 20. Difference between measured term values and calculated values from the molecular constants of the $F^1\Delta(v=v_f+3)$ state. A filled circle (•) is for an *e* level and an open circle (o) is for a *f* level.

$$\langle {}^1\Delta(v, Je/f)|H_{JL}|{}^1\Pi(v, Je/f)\rangle = -2\eta_1[J(J+1)-2]^{1/2}, \quad (4.9)$$

and

$$\langle {}^1\Pi(v, Je)|H_{JL}|{}^1\Sigma^+(v, Je)\rangle = -2\eta_2[J(J+1)]^{1/2}, \quad (4.10)$$

where η_1 and η_2 are constants. The energy shift of the *f* levels of the $F^1\Delta$ state could not be observed. It suggests the perturbing $^1\Pi$ state is far away from the $F^1\Delta$ and $H^1\Sigma^+$ states. Therefore, the perturbation between the $F^1\Delta$ and $H^1\Sigma^+$ levels occurs through a combination of the L-uncoupling interactions between the $^1\Delta(v, Je)$ and $^1\Pi(v, Je)$ levels: $\langle {}^1\Delta(v, Je)|H_{JL}|{}^1\Pi(v, Je)\rangle$, and between the $^1\Pi(v, Je)$ and $^1\Sigma^+(v, Je)$ levels: $\langle {}^1\Pi(v, Je)|H_{JL}|{}^1\Sigma^+(v, Je)\rangle$. In such an indirect perturbation of the $F^1\Delta(v=v_f+3)$ levels with the $H^1\Sigma^+(v=v_h+2)$ levels, the $^1\Pi$ state distant from these two states acts as "transfer" state for the $^1\Delta \sim {}^1\Sigma^+$ perturbation.[48]

(b) is due to the perturbation between the $H^1\Sigma^+(v=v_h+2)$ and U state. The largest energy shift of the $H^1\Sigma^+(v=v_h+2)$ levels is about 0.55 cm^{-1} at J=28. From the direction and the magnitude of the energy shifts, the rotational level of the $H^1\Sigma(v=v_h+2)$ and U state is expected to cross at J_c=25. The electronic state of the U band could not be identified because the only *e* levels can be observed through the perturbation with $^1\Sigma^+$ state which has only *e* levels.

(c) is due to the perturbation between the $H^1\Sigma^+(v=v_h+2)$ and T state. The observed line shapes of the $H^1\Sigma^+$ ($v=v_h+2$, J=38~44*e*) ← $B^1\Pi$(v'=9, J'=J-1*e*) and T(v, J=38~44*e*) ← $B^1\Pi$(v'=9, J'=J-1*e*) transitions are shown in Fig. 21. As we can see in Fig. 21 (lower trace), the transition lines to perturbing T(v, J=39~42, and 44*e*) levels are split into four lines. Similar splittings

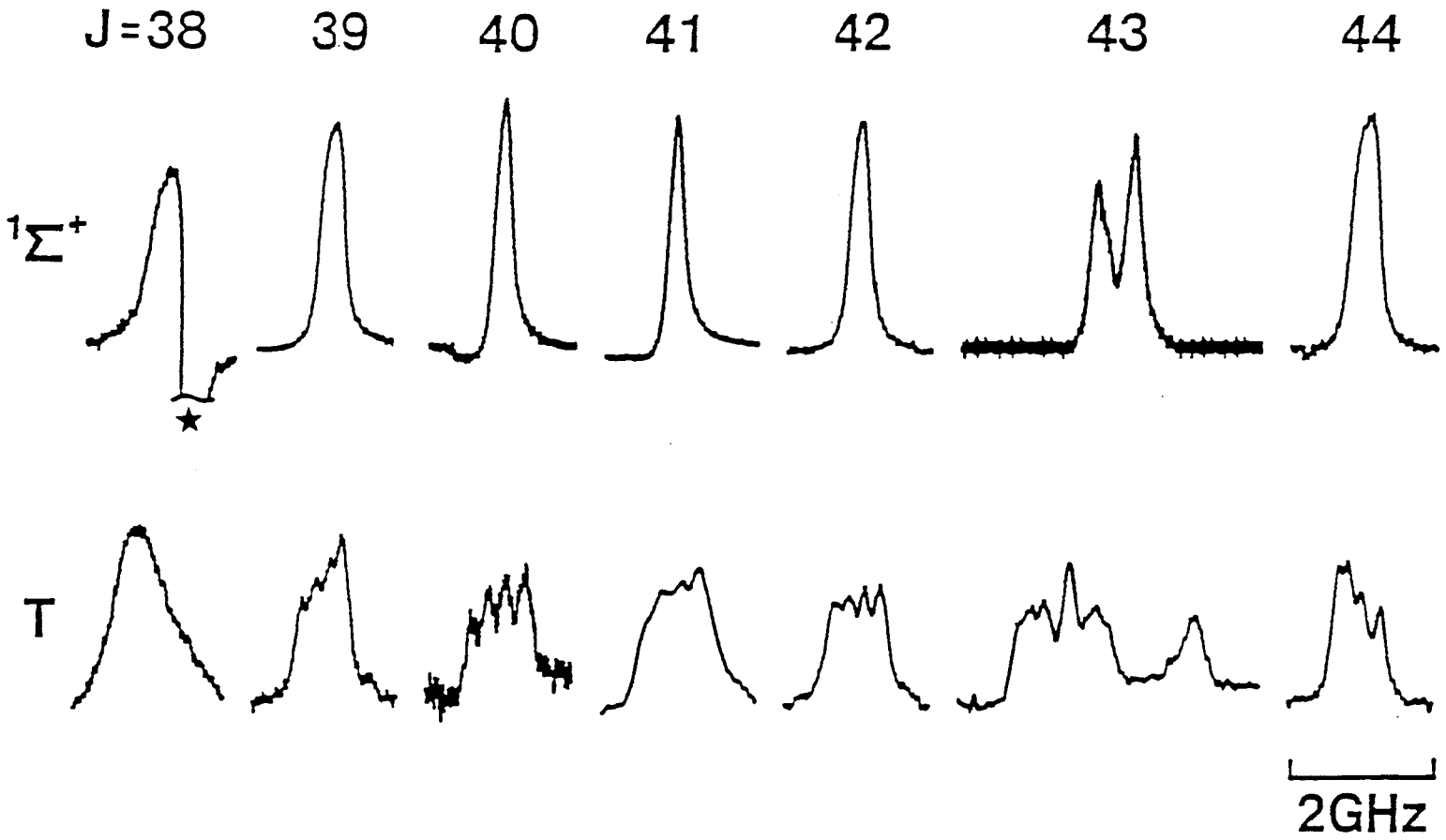

Fig. 21. The observed line shapes of the transition lines to the $H^1\Sigma^+(v=v_h+2,\ J=38\text{-}44e)$ levels perturbed by T state from the $B^1\Pi$ $(v'=9,\ J'=J-1e)$ levels. [R lines] Upper trace: transitions to the $H^1\Sigma^+$ state. Lower trace: transitions to T state. A line with ★ is an accidentally overlapped line, which is not observed for the corresponding P line.

were found for the $B^1\Pi \sim c^3\Sigma^+$ perturbation and identified as the hyperfine splittings of the $c^3\Sigma^+$ state induced by the Fermi contact interaction between the nuclear moment of ^{23}Na and an electron spin.[16] It suggests the observed splitting of the perturbed lines may be the hyperfine splitting. At J=43, the transition line to the $H^1\Sigma^+$ state is split to two lines, and the transition line to T state has more complicate structure. [see Fig. 21] These line shapes suggests that another perturbing state interacts to the $H^1\Sigma^+$ and/or T state. In order to identify the perturbing states, more extensive work are necessary on the perturbed regions.

Chapter. 5. DOPPLER-FREE HIGH RESOLUTION LASER SPECTROSCOPY OF THE Cs_2 $D^1\Sigma_u^+$ STATE AND THE PREDISSOCIATION

I. INTRODUCTION

The absorption spectrum of Cs_2 has six distinct band systems at 480, 580, 625, 720, 760, and 1000 nm.[49-51] Raab et al.[4] used the technique of the OODR polarization spectroscopy to study the 580 nm system, and they observed only P and R lines but no Q lines, which led to the assignment of the band to the $D^1\Sigma_u^+ - X^1\Sigma_g^+$ transition. The lines to low v' levels of the $D^1\Sigma_u^+$ state are overlapped with the lines of the $C^1\Pi_u - X^1\Sigma_g^+$ transition. By selecting an appropriate wavenumber region with a monochromator to detect a selected series of the $D^1\Sigma_u^+(v') - X^1\Sigma_g^+(v")$ transitions, Yokoyama et al.[52] observed the excitation spectra and determined the spectroscopic constants for v'=0-5. Collins et al.[53] studied the photolysis of Cs_2 by the two-photon technique; the time delay between the photodissociation and detection of the products was varied to separate the collisional effects from the primary dissociation process. They found that the $D^1\Sigma_u^+$ state predissociates selectively to the $Cs(6^2P_{3/2})$ and $Cs(6^2S_{1/2})$ atoms. Amiot et al.[54] studied the $D^1\Sigma_u^+ - X^1\Sigma_g^+$ transition by Fourier transform spectroscopy, Doppler-free polarization spectroscopy, and OODR polarization spectroscopy. They found an unusual vibrational spacing. Line broadening was observed in the Doppler-free polarization spectrum and was attributed to the predissociation.[4]

However, more extensive studies are necessary in order to understand the perturbations and the mechanism for predissocia-

tion. The Doppler-free polarization spectrum of the $D^1\Sigma_u^+(v', J')$ - $X^1\Sigma_g^+(v", J")$ transition up to v'=58 was measured, and the assignments of the $D^1\Sigma_u^+$ - $X^1\Sigma_g^+$ transitions were confirmed by the V-type OODR polarization spectrum. From the observed spectrum, the molecular constants of the $D^1\Sigma_u^+$ state were determined more accurately. The Doppler-free excitation spectrum was measured by using an experimental setup where a collimated Cs beam is crossed at right angles by the laser beam. The v' and J' dependence of the linewidths of the $D^1\Sigma_u^+(v', J')$ - $X^1\Sigma_g^+(v", J")$ transition was found by selectively measuring the atomic emission at 852.3 nm ($6^2P_{3/2}$ - $6^2S_{1/2}$: D_2 line). Using these spectroscopic data, we identify the perturbing states and predissociation mechanism.

5.1 Experimental

Two experimental methods were used in this work.

(a) The Doppler-free normal polarization spectroscopy was mainly used for the observation of the $D^1\Sigma_u^+(v', J')$ - $X^1\Sigma_g^+(v", J")$ transitions. The experimental details and arrangement is described in Chapter 2. and 3.1. In this case, Cs_2 vapor was produced by heating cesium metal (5g) in a stainless heat pipe oven, which was operated at 550K. A part of the Doppler-free polarization spectrum, which contains the rotational lines of the $D^1\Sigma_u^+(v'=27)$ - $X^1\Sigma_g^+(v"=2)$ transition, is shown in Fig. 22. The linewidths of the unperturbed rotational lines were about 75 MHz, and were very sensitive to the vapor pressure. When the assignments are difficult due to the perturbation, the V-type OODR polarization spectrum was measured and confirmed the assignments.

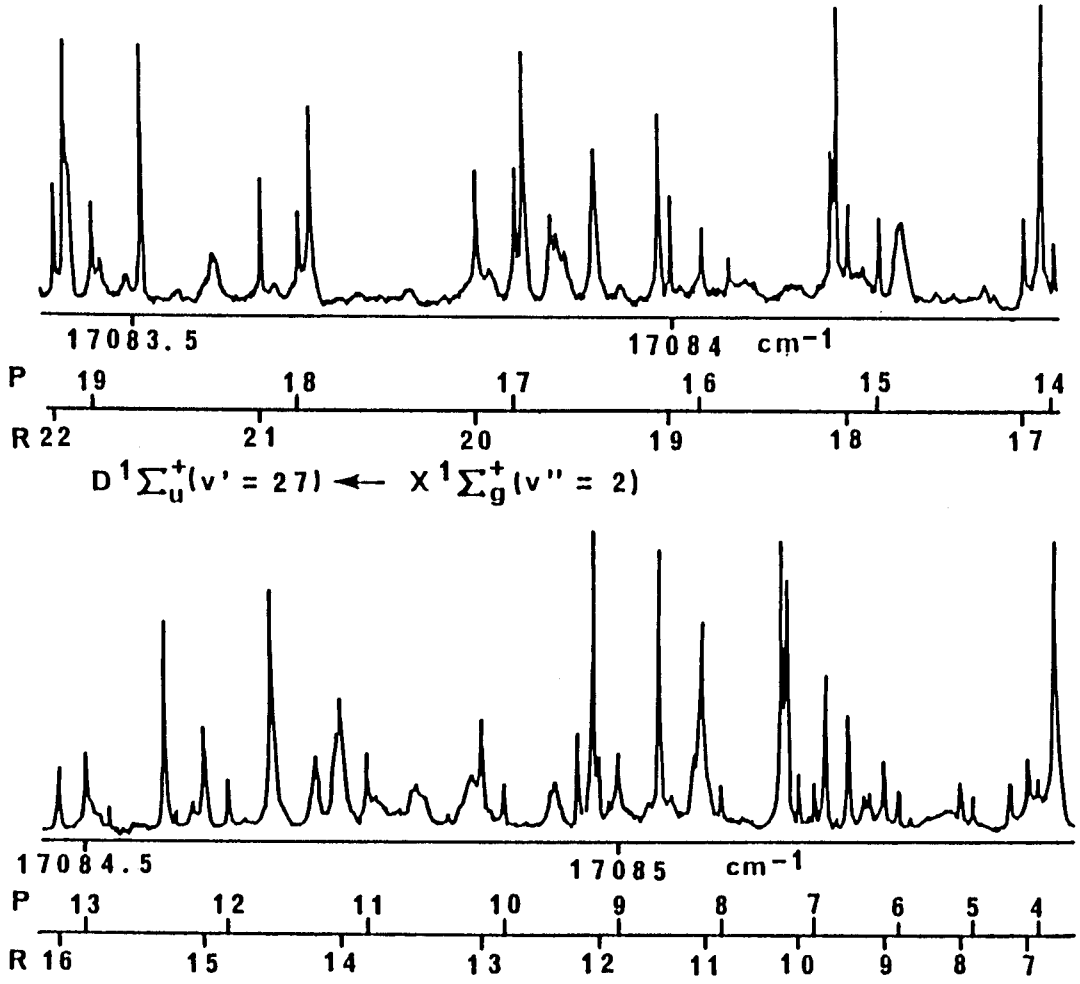

Fig. 22. A part of the Doppler-free polarization spectrum of Cs_2 near the band origin of the $D^1\Sigma_u^+(v'=27, J\pm1) - X^1\Sigma_g^+(v''=2, J)$ transition. The assignments are shown below the spectrum.

In this case, a circularly polarized pump beam was tuned to a center of the Doppler profile of a known transition $C^1\Pi_u$(v'=12, J'=34) - $X^1\Sigma_u^+$(v"=9, J"=33), and the probe laser was scanned through the spectral range of the $D^1\Sigma_u^+$(v', J'=32 and 34) - $X^1\Sigma_g^+$ (v"=9, J"=33) transitions.

(b) The experimental set-up for Doppler-free excitation spectroscopy[55] is shown in Fig. 23. The cesium beam was generated by expanding the vapor from the oven through a 300 μm orifice into a high vacuum chamber (< 10^{-6} Torr). Cesium metal (2g) was put in the oven cell, and heated to 400°C. The cesium beam was collimated by a conical skimmer with inner diameter of 1 mm at 5 cm from the nozzle, and crossed at right angles by the laser light. The cesium beam was trapped by a liquid-nitrogen trap after the excitation region. The emission was collected using a concave mirror and was detected by a red-sensitive photomultiplier (Hamamatsu R943-02) and a photon-counting system (Hamamatsu C767). The beam contained mainly Cs atoms, a small amount of Cs_2 molecules, and a trace of higher clusters. From the rotational and vibrational line spacings of the excitation spectrum, we identified the spectral lines as originating from the $D^1\Sigma_u^+$ - $X^1\Sigma_g^+$ excitation of the Cs_2 molecule. Contributions from the Cs atom and the higher clusters were negligible in the present study. The cesium beam was effusive with a rotational temperature of the Cs_2 molecule estimated to be about 200 K from the intensity distribution of the rotational lines. Two color filters (TOSHIBA C50S and R62), which transmit from 610 to 690 nm (transmittance > 20 %), were used to detect the fluorescence from the $D^1\Sigma_u^+$ state of the Cs_2 molecule, and appropriate interference filters to

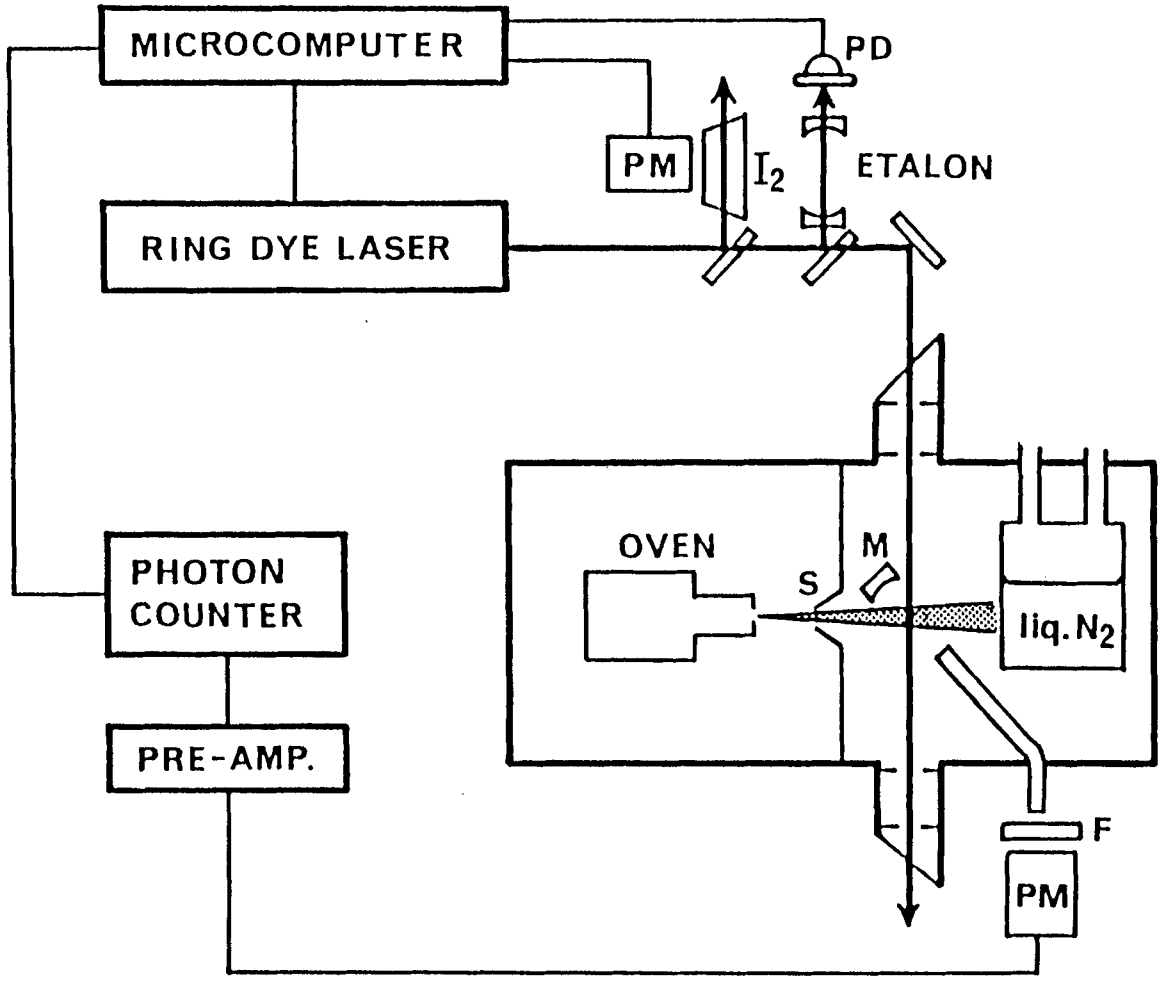

Fig. 23. The experimental setup for the Doppler-free excitation spectroscopy. S: conical skimmer, M: concave mirror, F: filter, PM: photomultiplier, and PD: photodiode.

detect selectively the $D_2(6^2P_{3/2} - 6^2S_{1/2})$ or $D_1(6^2P_{1/2} - 6^2S_{1/2})$ line emission from the photodissociated Cs atoms. Thus, we measured separately the intensities of the $D^1\Sigma_u^+ - X^1\Sigma_g^+$ molecular fluorescence and the D_2 or D_1 atomic emission as a function of the frequency of the tunable dye laser. We shall call these, respectively, "an excitation spectrum monitored by the molecular fluorescence," and "an excitation spectrum monitored by the D_2 or D_1 atomic emission." The Doppler-free excitation spectrum in Fig. 24 shows the rotational lines of the $D^1\Sigma_u^+(v'=28) - X^1\Sigma_g^+$ (v"=2) transition. The FWHM of the unperturbed lines of mostly 15 MHz was mainly due to the residual Doppler-width.

5.2 Determination of the Molecular Constants and Potential Energy Curve of the $D^1\Sigma_u^+$ State

The equilibrium internuclear distance of the $D^1\Sigma_u^+$ state is much longer than that of the $X^1\Sigma_g^+$ state (Fig. 25). Because of the Franck-Condon principle,[11] the transition to the low v' level of the $D^1\Sigma_u^+$ state can be allowed only from high v" levels of the $X^1\Sigma_g^+$ state. Furthermore, the transitions to the low v' levels are overlapped by lines of the $C^1\Pi_u - X^1\Sigma_g^+$ transition. Hence, it was difficult to assign the $D^1\Sigma_u^+(v', J') - X^1\Sigma_g^+(v", J")$ transition for low v' in the spectrum obtained by normal polarization spectroscopy. The transitions to the $D^1\Sigma_u^+(v'=6)$ level was measured with the excitation spectrum by choosing the appropriate wavenumber region through a monochromator to detect a selected series of the $D^1\Sigma_u^+(v') - X^1\Sigma_g^+$ (v") transitions.[52] The transitions to the $D^1\Sigma_u^+(v'=7\sim58)$ levels were measured by Doppler-free

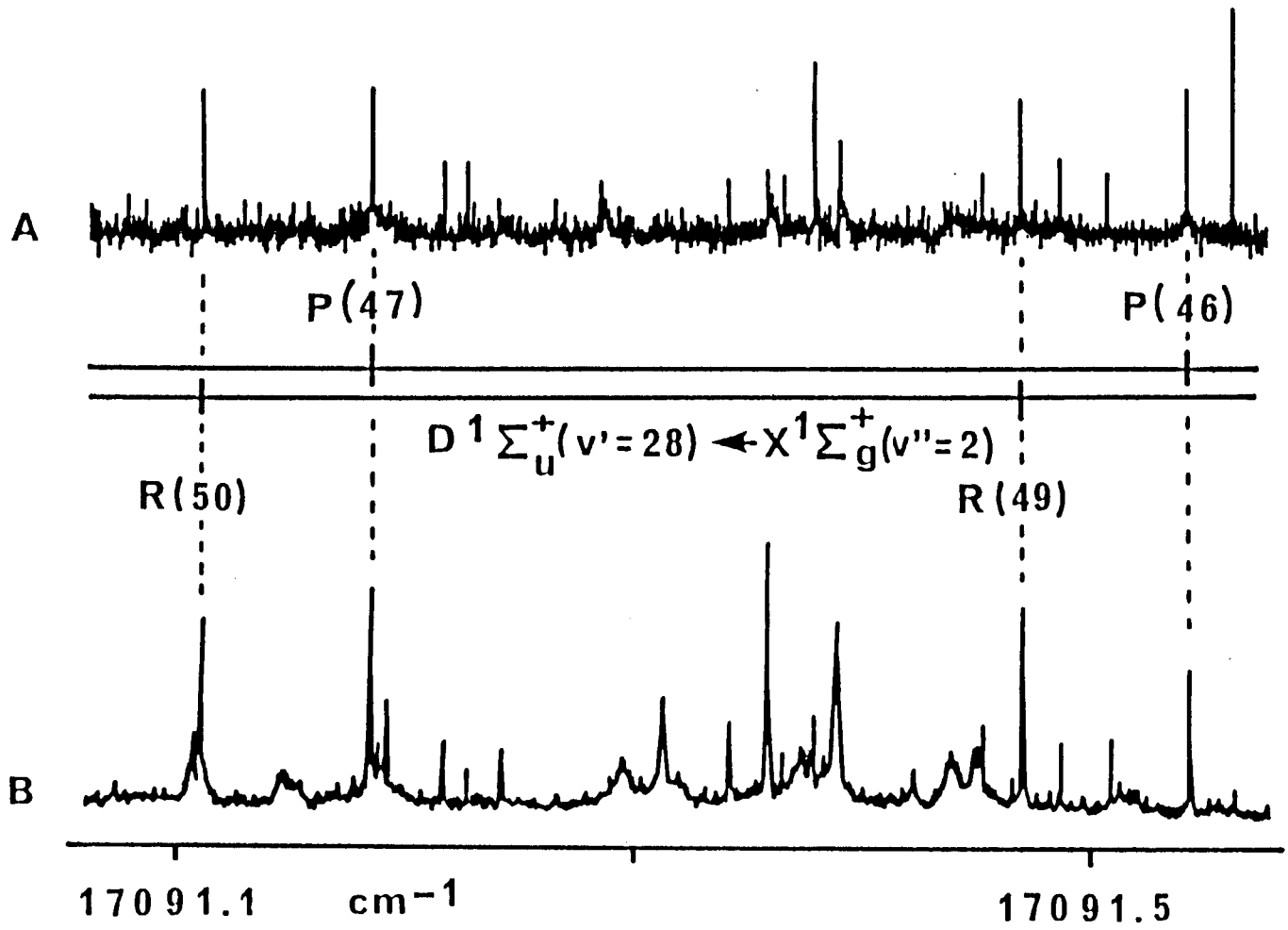

Fig. 24. A part of the Doppler-free excitation spectrum of Cs_2 beam near the $D^1\Sigma_u^+(v'=28, J=45) - X^1\Sigma_g^+(v"=2, J=46)$ transition. Upper trace (A) is the excitation spectrum monitored by the $D^1\Sigma_u^+ - X^1\Sigma_g^+$ molecular fluorescence. Lower trace (B) is the excitation spectrum monitored by the D_2 atomic emission. The atomic emission is about 5 times stronger than the molecular fluorescence.

polarization spectroscopy. The molecular constants of the $X^1\Sigma_g^+$ state, which are accurate up to the dissociation limit, have been reported.[56] Using these molecular constants, the quantum numbers v" and J" for each of a series of the P and R lines could be easily assigned.

The term energies of $^1\Sigma^+(v, J)$ levels are expressed in Eq. (1.3) and (1.4). The wavenumber $\sigma(v'J', v"J")$ of the $D^1\Sigma_u^+(v', J') - X^1\Sigma_g^+ (v", J")$ transition is given by

$$\sigma(v'J', v"J") = E_{v',J'} - E_{v",J"}. \quad (5.1)$$

The term energies $E_{v',J'}$ of the $D^1\Sigma_u^+$(v':unassigned, J':assigned) levels are calculated by Eq. (5.1) from the observed wavenumber $\sigma(v'J', v"J")$ of the transitions and the term energies $E_{v"J"}$ of the assigned $X^1\Sigma_g^+(v", J")$ levels. Molecular constants for the $D^1\Sigma_u^+$(v'=6~58) levels were determined by the following procedures:

(i) Preliminary values of T_v and B_v for each v were calculated by a nonlinear least-squares fitting procedure[57] for the levels with J smaller than 30.

(ii) The values of T_v and B_v obtained in these separate fittings for v=6~58 and in Ref. 52 for v=0~5 were used as input data for least-squares fittings, which yielded the Dunham coefficients Y_{ij} (j=0 and 1):[19]

$$G_v = \sum_{i=1,2,\cdots} Y_{i0}(v + 1/2)^i, \quad (5.2)$$

$$B_v = \sum_{i=0,1,\cdots} Y_{i1}(v + 1/2)^i. \quad (5.3)$$

(iii) From the Dunham coefficients Y_{i0} and Y_{i1} obtained above, the rotationless potential curve of the $D^1\Sigma_u^+$ state was construct-

ed up to v=58 by the RKR method.[20,21]

(iV) For the RKR potential curve, the values of G_v, B_v, D_v, and H_v for v=6~58 were then calculated by the computational method described by Hutson.[22]

(V) With D_v and H_v fixed at these values, a nonlinear least-squares fitting procedure[50] for the levels with J≤30 and v=6~58 was used to redetermine the values of T_v and B_v.

(Vi) With T_v and B_v fixed at these values, a nonlinear least-squares fitting procedure[50] for all the assigned rotational lines of each v was used to redetermine the values of D_v and H_v.

5029 assigned lines were used to determine the molecular constants of the $D^1\Sigma_u^+$ state. The results are listed in Table XIV. Almost all line frequencies could be reproduced by these constants with deviations of less than 0.01 cm^{-1}. The standard deviation for each v level is listed in Table XIV. The T_v and B_v values of v=0~58 were used, respectively, to determine the Dunham coefficients Y_{i0} and Y_{i1} by least-squares fitting. The results are listed in Table XV. The values of D_v and H_v are irregular and are not appropriate for the Dunham expansion. From the Dunham coefficients Y_{i0} and Y_{i1}, the potential curve of the $D^1\Sigma_u^+$ state was constructed by the RKR method. The results are shown in Table XVI and are plotted in Fig. 25.

Table XIV. The vibrational energy (T_v), the rotational constant (B_v), and the centrifugal distortion constants (D_v and H_v) for each vibrational level of the $D^1\Sigma_u^+$ state. δE is the standard deviation $|E_{v,J}^{Obs} - E_{v,J}^{Cal}|$. All the values are in units of cm^{-1}. N is the number of transitions which were used to determine the molecular constants.

v	T_v	10^3B_v	10^9D_v	$10^{15}H_v$	$10^2\delta E$	N
0	16708.9281	7.7507	4.756	-1.92	1.01	126
1	16728.6344	7.7023	4.788	-1.61	0.71	54
2	16748.1360	7.6548	4.823	-1.32	1.36	284
3	16767.4350	7.6083	4.857	-1.08	0.89	42
4	16786.5366	7.5627	4.880	-0.93	0.54	122
5	16805.4192	7.5179	4.881	-0.82	0.99	355
6	16824.1493	7.4783	4.999	0.46	0.40	30
7	16842.6481	7.4335	5.052	0.90	0.24	78
8	16860.9737	7.3901	5.090	1.23	0.13	58
9	16879.1207	7.3504	5.111	1.53	0.11	31
10	16897.0793	7.3019	5.109	1.64	0.17	96
11	16914.9148	7.2629	5.078	1.59	0.26	83
12	16932.5845	7.2262	5.019	1.48	0.31	60
13	16950.1233	7.1835	4.931	1.22	0.22	87
14	16967.5461	7.1440	4.815	0.93	0.12	22
15	16984.8653	7.1097	4.987	-2.55	0.19	75
16	17002.1049	7.0795	4.526	0.39	0.23	118
17	17019.2808	7.0486	4.365	0.23	0.25	107
18	17036.4099	7.0268	4.202	0.20	0.56	97
19	17053.5125	7.0009	4.045	0.29	0.16	27
20	17070.5936	6.9735	3.900	0.51	0.23	90
21	17087.6721	6.9511	3.774	0.87	0.15	57
22	17104.7393	6.9377	3.670	1.35	0.22	78
23	17121.7833	6.9224	3.592	1.92	0.56	91
24	17138.9109	6.9004	3.541	2.57	0.18	67
25	17155.9796	6.8740	3.519	3.27	0.21	106
26	17173.0459	6.8539	3.525	3.99	0.17	84
27	17190.0991	6.8432	3.558	4.70	0.38	121
28	17207.1373	6.8287	3.615	5.36	0.38	90
29	17224.1738	6.7987	3.692	5.93	0.19	68
30	17241.1668	6.7819	3.787	6.38	0.10	72
31	17258.1293	6.7609	3.893	6.64	0.22	37
32	17275.0321	6.7213	4.006	6.66	0.43	102
33	17291.9292	6.7281	4.120	6.36	0.14	84
34	17308.7414	6.6915	4.228	5.75	0.14	75
35	17325.4206	6.6549	4.326	4.78	0.34	40

Table XIV. (Continued)

v	T_v	10^3B_v	10^9D_v	$10^{15}H_v$	$10^2\delta E$	N
36	17342.3070	6.6222	4.409	3.43	0.85	75
37	17358.8184	6.6038	4.472	1.72	0.12	38
38	17375.2403	6.5553	4.512	-0.28	0.30	78
39	17391.8996	6.5666	4.528	-2.53	0.16	43
40	17408.2092	6.5127	4.522	-4.95	0.18	80
41	17424.1763	6.4819	-5.980	-7.48	0.44	76
42	17440.7890	6.4713	9.024	-10.11	0.27	108
43	17456.7905	6.4225	4.395	-12.76	0.20	105
44	17472.0103	6.4511	-9.235	-15.41	0.79	88
45	17488.8130	6.3623	4.266	-18.09	0.23	78
46	17504.4689	6.3229	-3.749	-20.79	0.39	91
47	17520.5948	6.3145	1.466	-23.38	0.65	71
48	17535.8881	6.2604	4.098	-25.77	0.15	83
49	17551.1546	6.2382	4.060	-27.81	0.70	90
50	17566.9549	6.2055	14.784	-29.23	0.61	86
51	17581.9293	6.1609	4.005	-29.63	0.27	98
52	17596.7910	6.1483	3.972	-28.50	0.63	90
53	17612.2826	6.0823	9.716	-20.50	0.25	85
54	17626.8711	6.0579	3.793	-17.87	0.19	76
55	17641.3258	6.0553	3.548	-4.80	0.32	62
56	17656.4898	5.9715	10.737	15.93	0.36	72
57	17670.6336	5.9473	2.287	40.49	0.20	81
58	17684.7012	5.9337	1.256	54.11	0.31	61

Table XV. Dunham coefficients Y_{ij} for the $D^1\Sigma_u^+$ state.[a] All values are in cm^{-1}.

i	j	Y_{ij}	i	j	Y_{ij}
1	0	19.9103	1	1	7.7820×10^{-3}
2	0	-1.05117×10^{-1}	2	1	-5.1690×10^{-5}
3	0	2.37699×10^{-3}	3	1	5.8034×10^{-7}
4	0	-4.43514×10^{-4}	4	1	4.8064×10^{-9}
5	0	3.83326×10^{-5}	5	1	-1.6010×10^{-10}
6	0	-1.46591×10^{-6}			
7	0	2.86676×10^{-8}			
8	0	-2.83418×10^{-10}			
9	0	1.12767×10^{-12}			

[a] These values are useful for $J<30$.

Table XVI. The RKR potential energy curve of the $D^1\Sigma_u^+$ state. R_{min} and R_{max} are the turning points of each vibrational level. R_e is the equilibrium internuclear distance.

v	G_v/cm^{-1}	$R_{min}/Å$	$R_{max}/Å$	v	G_v/cm^{-1}	$R_{min}/Å$	$R_{max}/Å$
0	9.9314	5.5581	5.8781	31	559.1414	4.8031	7.5379
1	29.6373	5.4568	6.0134	32	576.0651	4.7924	7.5726
2	49.1443	5.3912	6.1128	33	592.9382	4.7819	7.6071
3	68.4536	5.3402	6.1976	34	609.7533	4.7714	7.6414
4	87.5643	5.2974	6.2738	35	626.5039	4.7610	7.6758
5	106.4753	5.2601	6.3443	36	643.1842	4.7507	7.7102
6	125.1865	5.2268	6.4106	37	659.7896	4.7405	7.7445
7	143.7005	5.1965	6.4737	38	676.3163	4.7305	7.7789
8	162.0222	5.1685	6.5342	39	692.7615	4.7206	7.8133
9	180.1595	5.1425	6.5924	40	709.1230	4.7108	7.8478
10	198.1231	5.1182	6.6487	41	725.3993	4.7013	7.8823
11	215.9262	5.0952	6.7032	42	741.5891	4.6919	7.9170
12	233.5837	5.0736	6.7561	43	757.6910	4.6828	7.9517
13	251.1123	5.0531	6.8074	44	773.7035	4.6739	7.9867
14	268.5291	5.0336	6.8573	45	789.6241	4.6653	8.0218
15	285.8520	5.0151	6.9057	46	805.4493	4.6570	8.0572
16	303.0980	4.9976	6.9528	47	821.1746	4.6489	8.0931
17	320.2836	4.9808	6.9985	48	836.7937	4.6411	8.1294
18	337.4239	4.9649	7.0430	49	852.2994	4.6336	8.1662
19	354.5320	4.9497	7.0862	50	867.6833	4.6263	8.2036
20	371.6193	4.9351	7.1283	51	882.9365	4.6193	8.2418
21	388.6946	4.9212	7.1692	52	898.0506	4.6126	8.2808
22	405.7644	4.9078	7.2092	53	913.0192	4.6062	8.3207
23	422.8331	4.8949	7.2482	54	927.8395	4.6002	8.3614
24	439.9021	4.8825	7.2864	55	942.5153	4.5948	8.4027
25	456.9712	4.8704	7.3239	56	957.0602	4.5900	8.4445
26	474.0379	4.8586	7.3607	57	971.5018	4.5862	8.4863
27	491.0978	4.8472	7.3969	58	985.8872	4.5837	8.5273
28	508.1452	4.8359	7.4327				
29	525.1734	4.8248	7.4681		R_e = 5.7095 Å		
30	542.1748	4.8139	7.5031				

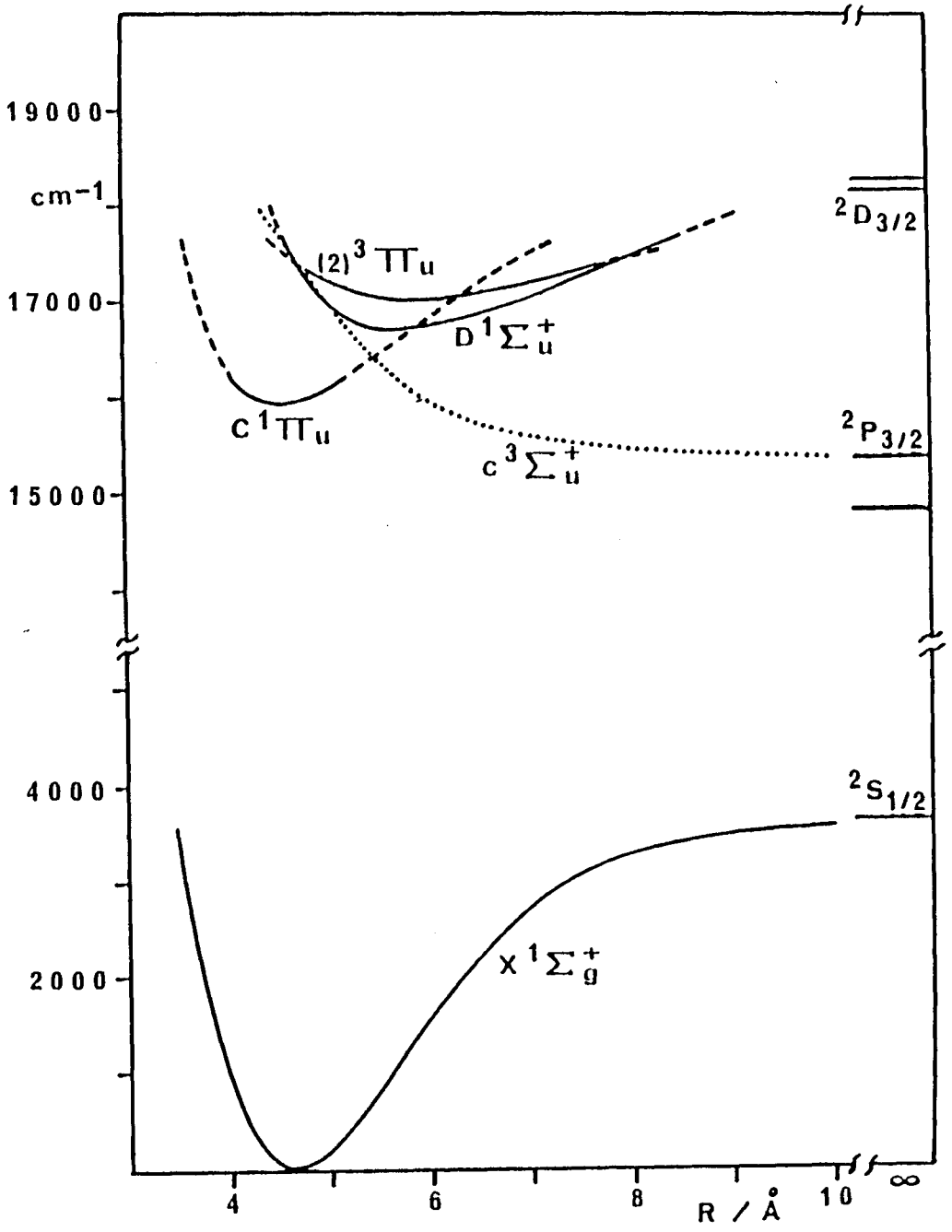

Fig. 25. The potential energy curves for Cs_2. The curves of the $D^1\Sigma_u^+$, $c^1\Pi_u$, and $X^1\Sigma_g^+$ states are calculated by the RKR method from the molecular constants in this work, Ref. 4, and Ref. 56, respectively. The curve of the $(2)^3\Pi_u$ state is a Morse function estimated in this work. The dotted line is the estimated diabatic potential energy curve of the $c^3\Sigma_u^+$ state, which is expected to cross the potential curve of another $^3\Sigma_u^+$ state,[55] which is bound and separates into the $Cs(5^2D_{3/2})$ and $Cs(6^2S_{1/2})$ atoms.

5.3 Perturbation Between the $D^1\Sigma_u^+$ and $(2)^3\Pi_u$ States

The vibrational spacing $\Delta G_v = G_{v+1} - G_v = T_{v+1} - T_v$ for the $D^1\Sigma_u^+$ state was calculated from T_v in Table XIV, and is plotted as a function of v by open circles in Fig. 26. The fitted values of ΔG_v, which are calculated from Eq. (5.3) and the Dunham coefficients Y_{i0} in Table XV, are shown by filled circles in Fig. 26. ΔG_v decreases linearly as v increases for v=0~12. ΔG_v is almost invariant for v=17~29, but large differences between ΔG_v and the fitted values are observed for v>35. The striking variation of ΔG_v with v was first found by Amiot et al.,[54] but their detailed values are slightly different from our results. They reported a large deviation from the fitted ΔG_v curve around v=12~19, but we could not find such a deviation. The discrepancy may result from a wrong assignment of v' or J'. In order to confirm our assignments, the V-type OODR polarization spectrum was observed. Starting from a selected lower level $X^1\Sigma_g^+$(v"=9, J"=33), the OODR polarization signals for a vibrational progression to the upper levels $D^1\Sigma_u^+$(v'=5~14, J'=32 and 34) were observed. A part of the OODR polarization spectrum is shown in Fig. 27. A comparison of the OODR polarization spectrum and the normal polarization spectrum is shown in Fig. 28. Because transitions only from the selected $X^1\Sigma_g^+$(v", J") level are observable in the OODR polarization spectrum, the v' and J' quantum numbers of the $D^1\Sigma_u^+$(v', J') - $X^1\Sigma_g^+$(v", J") transition could be accurately assigned.

Usually, ΔG_v decreases regularly as v increases because of the anharmonicity. The observed change of ΔG_v with v results from a change in the gradient of the potential curve of the $D^1\Sigma_u^+$

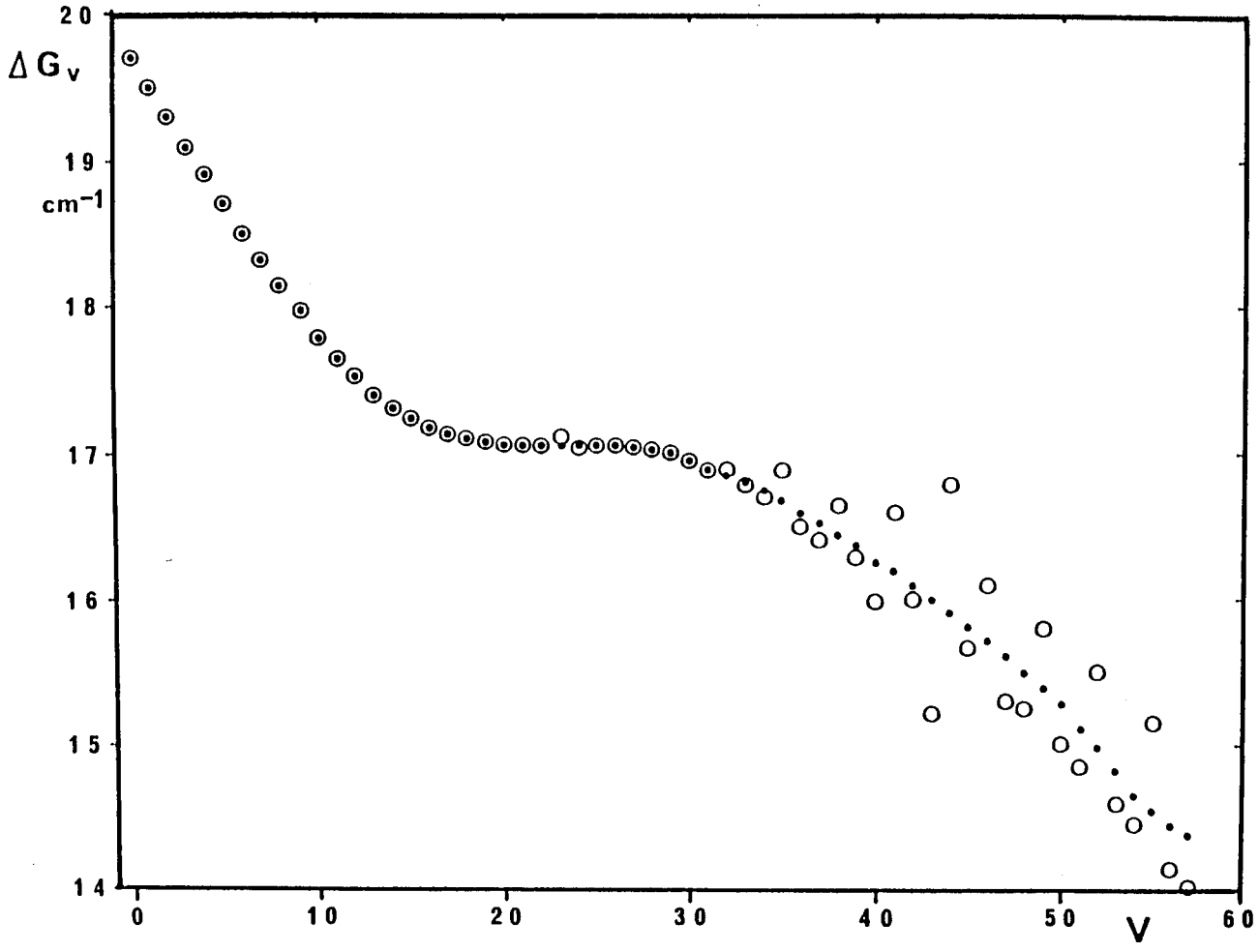

Fig. 26. Open circles (o) show the variation of vibrational spacing ΔG_v of the $D^1\Sigma_u^+$ state with v. Filled circles (•) are the fitted values of ΔG_v, which are calculated from Eq. (5.4) and the Dunham coefficients Y_{i0} in Table XV.

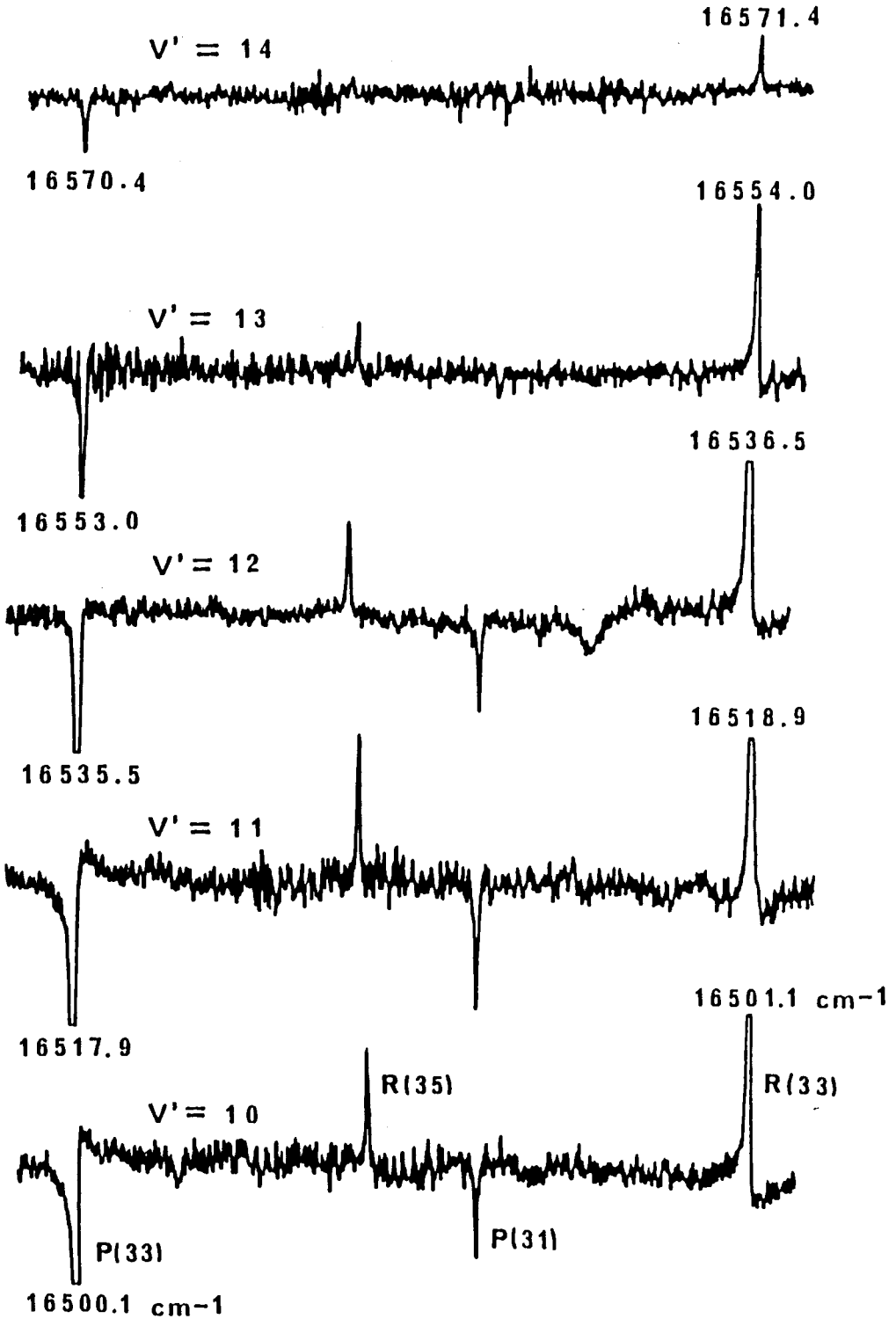

Fig. 27. A part of the OODR polarization spectrum for the $D^1\Sigma_u^+$ (v'=10-14, J'=32 and 34) - $X^1\Sigma_g^+$(v"=9, J"=33) transitions: P(33) and R(33). The $C^1\Pi_u$(v'=12, J'=34) - $X^1\Sigma_g^+$(v"=9, J"=33) transition is used as the pump transition. Rotational lines R(35) and P(31), which are induced by a collisional energy transfer, are also observed.

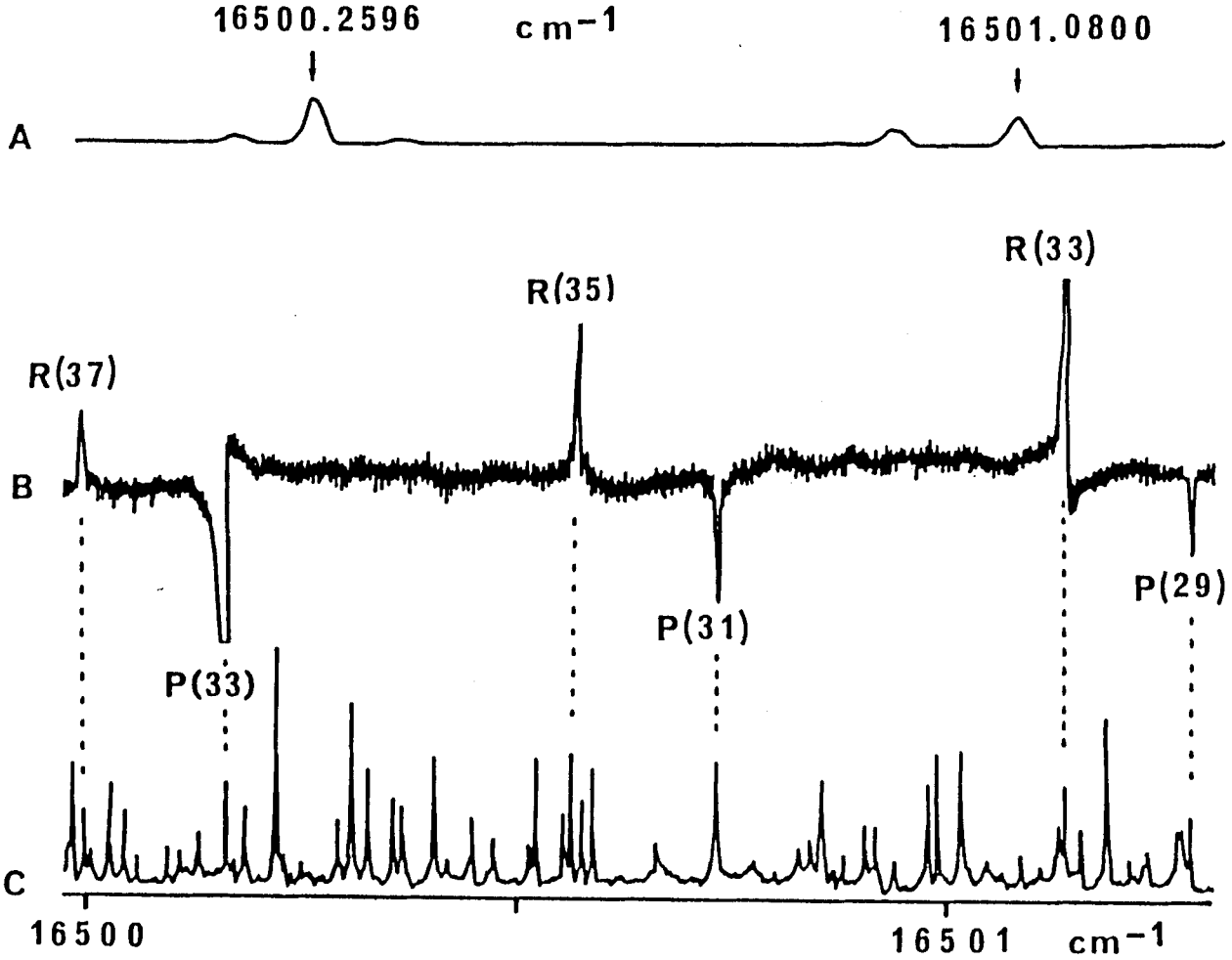

Fig. 28. Top (A) is the fluorescence excitation spectrum of I_2 for calibration of the absolute wavenumber. The second (B) is a part of the OODR-polarization spectrum, where the $C^1\Pi_u(v'=12, J'=34) - X^1\Sigma_g^+(v''=9, J''=33)$ transition is used as the pump transition. Bottom (C) is the normal polarization spectrum and a part of the assignments.

state. No perturbations were found in the individual rotational lines of the P and R branches for each vibronic transition. However, large deviations of ΔG_v from the fitted ΔG_v curve were observed for v larger than 35 (Fig. 26). Almost all rotational levels of a vibrational state deviate uniformly from the regular changes in a vibrational progression. Such a perturbation is called a vibrational perturbation.[11]

Perturbations can occur only between levels of the same total angular momentum J; the selection rule is $\Delta J=0$.[11,18] The resulting shift of a level increases as the energy separation between the perturbing levels decreases. The ΔG_v values for v=35-58 are fluctuating; some are shifted upward and some downward from the fitted values. If the perturbing state is a continuous state, such non-uniform energy shifts are not observed. From this fact, we can conclude that the perturbing electronic state is a bound state. The shift of all rotational levels of a vibrational state can occur if the rotational constants of two perturbing vibrational states are nearly equal; when the energy separations between levels of the same J of the two perturbing vibrational states are equal, the uniform shift of all rotational levels of a vibrational state occurs. Hence, the equilibrium internuclear distance of the perturbing state can be estimated to be nearly equal (within ±0.2 Å) to the $D^1\Sigma_u^+$ state.

A possible perturbing state is the $(2)^3\Pi_u$ state, which asymptotically dissociates into the $Cs(6^2S_{1/2})$ and $Cs(5^2D_{3/2})$ atoms.[58] The perturbation between the $D^1\Sigma_u^+$ and $(2)^3\Pi_u$ states is induced by the spin-orbit interaction (H_{SO}). The nonvanishing matrix elements between the three Hund's case (a) states $^3\Pi_\Omega$ (Ω

= 0, 1, and 2) and a $^1\Sigma^+$ state are[47]

$$<^1\Sigma^+(v', J)|H_{so}|^3\Pi_0(v, Je)> = \xi = \xi_{el}<v'|v>, \quad (5.4)$$

where the symbol *e* refers to an *e* level of the Λ-type doubling. The perturbed term energies are expressed as

$$PTE_+ = \{E_2 + E_1 + [(E_2 - E_1)^2 + 4\xi^2]^{1/2}\}/2,$$
$$PTE_- = \{E_2 + E_1 - [(E_2 - E_1)^2 + 4\xi^2]^{1/2}\}/2, \quad (5.5)$$

where E_1 and E_2 are the unperturbed energies of the $D^1\Sigma_u^+(v', J)$ and $(2)^3\Pi_{0u}(v, Je)$ levels, respectively. For a given pair of interacting levels, the higher level is displaced upward and the lower level downward by an equal amount. For a given ξ, the smaller the separation between the levels, the larger are their shifts. From the direction of the energy shift of the $D^1\Sigma_u^+(v')$ level, we can estimate the location of the perturbing $(2)^3\Pi_{0u}(v\ e)$ level. By analyzing a series of shifts of the observed vibrational energies of the $D^1\Sigma_u^+(v'=35\text{~}58)$ levels from the extrapolated values, the value of $\Delta G_v = G_{v+1} - G_v$ for the $(2)^3\Pi_u$ state around $D^1\Sigma_u^+(v'=40)$ is estimated to be 12 cm^{-1}, and the value of $\omega_e x_e$ to be 0.033 cm^{-1}.

Large shifts of the vibrational levels of $D^1\Sigma_u^+(v')$ around v'=35~58 suggest that the potential curve of the $(2)^3\Pi_u$ state crosses the potential curve of the $D^1\Sigma_u^+$ state at about v'=40. Since the level shifts are observed only for v'>32, the potential minimum of the $(2)^3\Pi_u$ state is predicted to lie above the potential minimum of the $D^1\Sigma_u^+$ state.

In order to reproduce the above factors, we estimate that the potential curve of the $(2)^3\Pi_u$ state is described by the Morse potential

$$V(R) = 17028 + 1500\{1 - \exp[-0.35886(R - 5.85)]\}^2, \quad (5.6)$$

where V(R) is in units of cm^{-1} and the internuclear distance R is in units of Å. The vibrational level energies are given by;[59]

$$E_v = 17028 + 14.0(v + 1/2) - 0.032667(v + 1/2)^2. \quad (5.7)$$

The unperturbed energy (E_v) of the $D^1\Sigma_u^+(v, J=0)$ level, which can be approximated by the fitted level energy, is calculated from the Dunham coefficients in Table XV. The energies E_v of the $D^1\Sigma_u^+(v=34\text{-}58)$ and $(2)^3\Pi_u(v=21\text{-}53)$ vibronic states are shown in Fig. 29. The difference between an observed level energy, which is listed as T_v in Table XIV, and the unperturbed level energy (E_v) is shown as ΔE (= T_v - E_v) in Fig. 29. The observed shifts (ΔE's) of the $D^1\Sigma_u^+$ vibronic states can be explained very well by the location of the unperturbed $D^1\Sigma_u^+$ and $(2)^3\Pi_u$ vibronic states, as can seen in Fig. 29. Eq. (5.6) should represent the potential curve of the $(2)^2\Pi_u$ state fairly well for V(R) < 17700 cm^{-1}.

5.4. Predissociation of the $D^1\Sigma_u^+$ State

Line broadening was observed in the Doppler-free polarization spectrum, and was attributed to the predissociation.[4] In order to study the predissociation more directly, we measured separately the excitation spectra monitored by the molecular fluorescence and the excitation spectra monitored by the D_2 or D_1 atomic emission. In order to eliminate collisional effects and to obtain a Doppler-free high resolution spectrum, we used a collimated cesium beam crossed at right angles with the laser beam. The intensity of the excitation spectrum of the $D^1\Sigma_u^+(v', J') - X^1\Sigma_g^+(v'', J'')$ transition monitored by the molecular fluorescence became very weak as v' increases. Conversely, only the

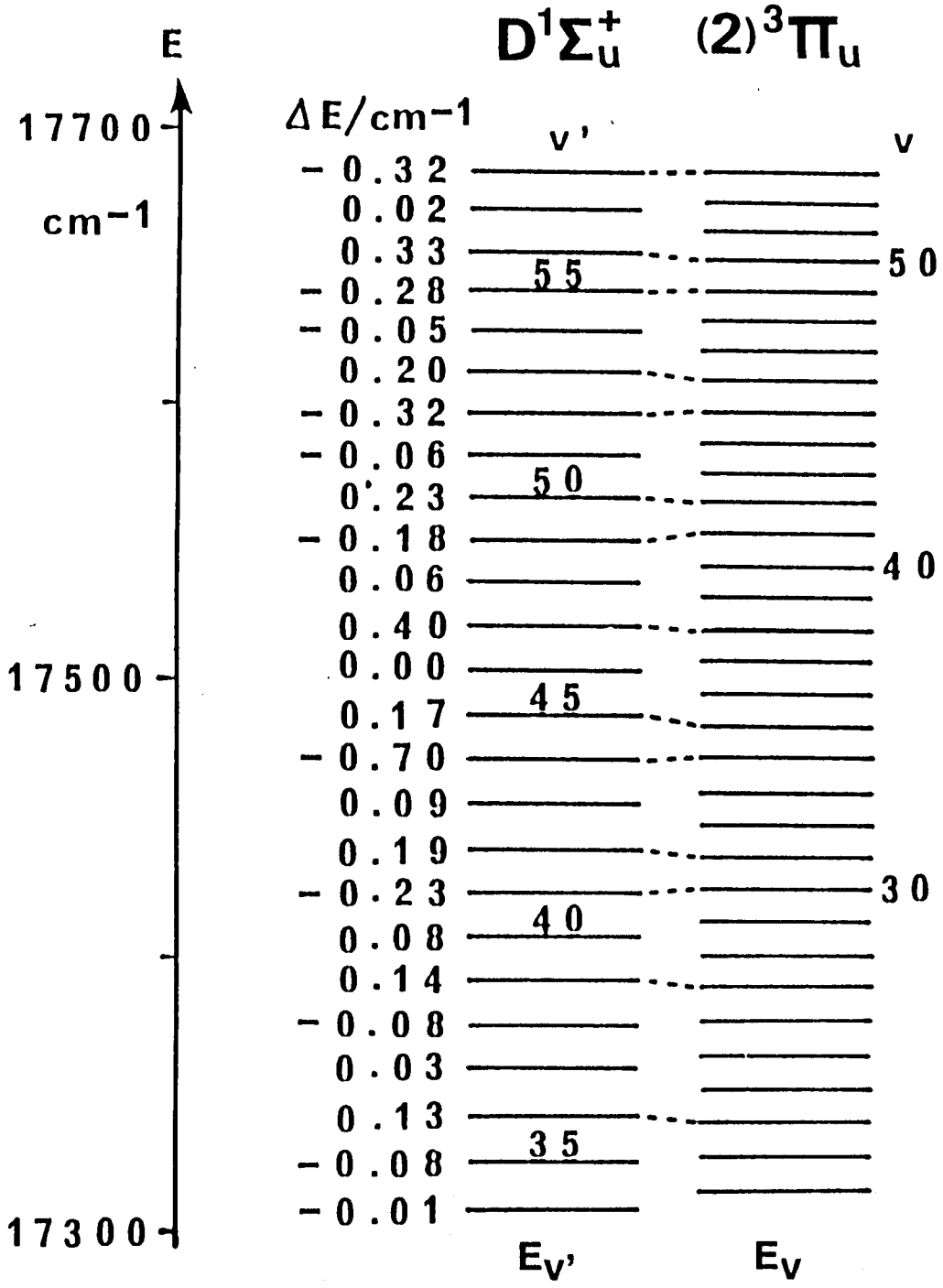

Fig. 29. The unperturbed level energies (E_v') of the $D^1\Sigma_u^+(v', J=0)$ state, as calculated from the Dunham coefficients in Table XV. ΔE is the difference between the observed level energy, which is listed as T_v in Table XIV, and the unperturbed level energy E_v'. The unperturbed level energies (E_v) of the $(2)^3\Pi_u(v, J=0)$ state is calculated from Eq. (5.7). Strongly perturbing levels ($|\Delta E|>0.1$ cm^{-1}) are connected by broken lines.

excitation spectrum monitored by the molecular fluorescence could be detected for v'<15. We could not detect any excitation spectrum monitored by the D_1 atomic emission for any v'. The observed results show that (i) the predissociation of the $D^1\Sigma_u^+$ state occurs appreciably for v'>20, and the probability of predissociation increases with v'. (ii) all of the $D^1\Sigma_u^+(58>v'>20)$ levels decompose selectively into two atoms $Cs(6^2P_{3/2})$ and $Cs(6^2S_{1/2})$.

A significant change in the linewidth was observed for v'>25. We measured the v' and J' dependence of the linewidth Γ. An example of the change of the line shape with J' is shown in Fig. 30. The linewidth increases with increase in J'. The line broadening may be due to hyperfine splitting, but such structure is not observed with our spectral resolution of 15 MHz. The predissociation ratio, which is proportional to the intensity ratio of two excitation spectra monitored by the atomic emission and monitored by the molecular fluorescence, is observed to increase in parallel with the increase of the linewidth. Hence, the hyperfine splitting is ignored. The observed linewidth can be attributed to the lifetime broadening. The J' dependence of Γ was found to change significantly with v'. The observed dependence of Γ on J' for v'=28 and v'=46 is shown, respectively, in Figs. 31 and 32. The linewidth Γ is related to the lifetime τ of the level by

$$\tau(s) = \frac{5.3\times10^{-12}}{\Gamma(cm^{-1})} = \frac{159\times10^{-9}}{\Gamma(MHz)} \quad . \tag{5.8}$$

The lifetime τ is related to the predissociation rate k_p and the radiative decay rate k_r by

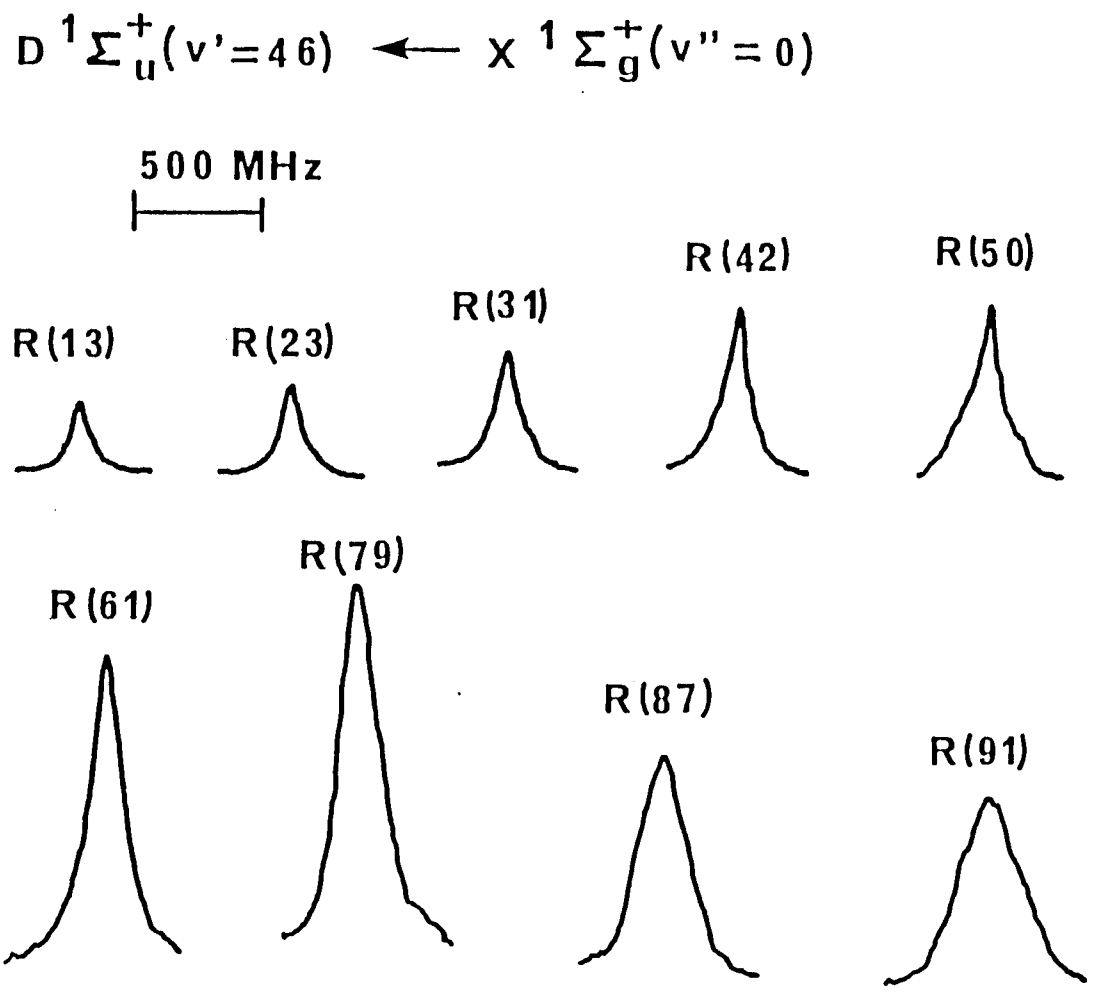

Fig. 30. The J-dependence of the spectral line shape of the $D^1\Sigma_u^+(v'=46,\ J+1)$ - $X^1\Sigma_g^+(v"=0,\ J)$ transitions. These are the excitation spectra monitored by the D_2 atomic emission. The spectral resolution is 15 MHz, and the frequency scale is shown on the top.

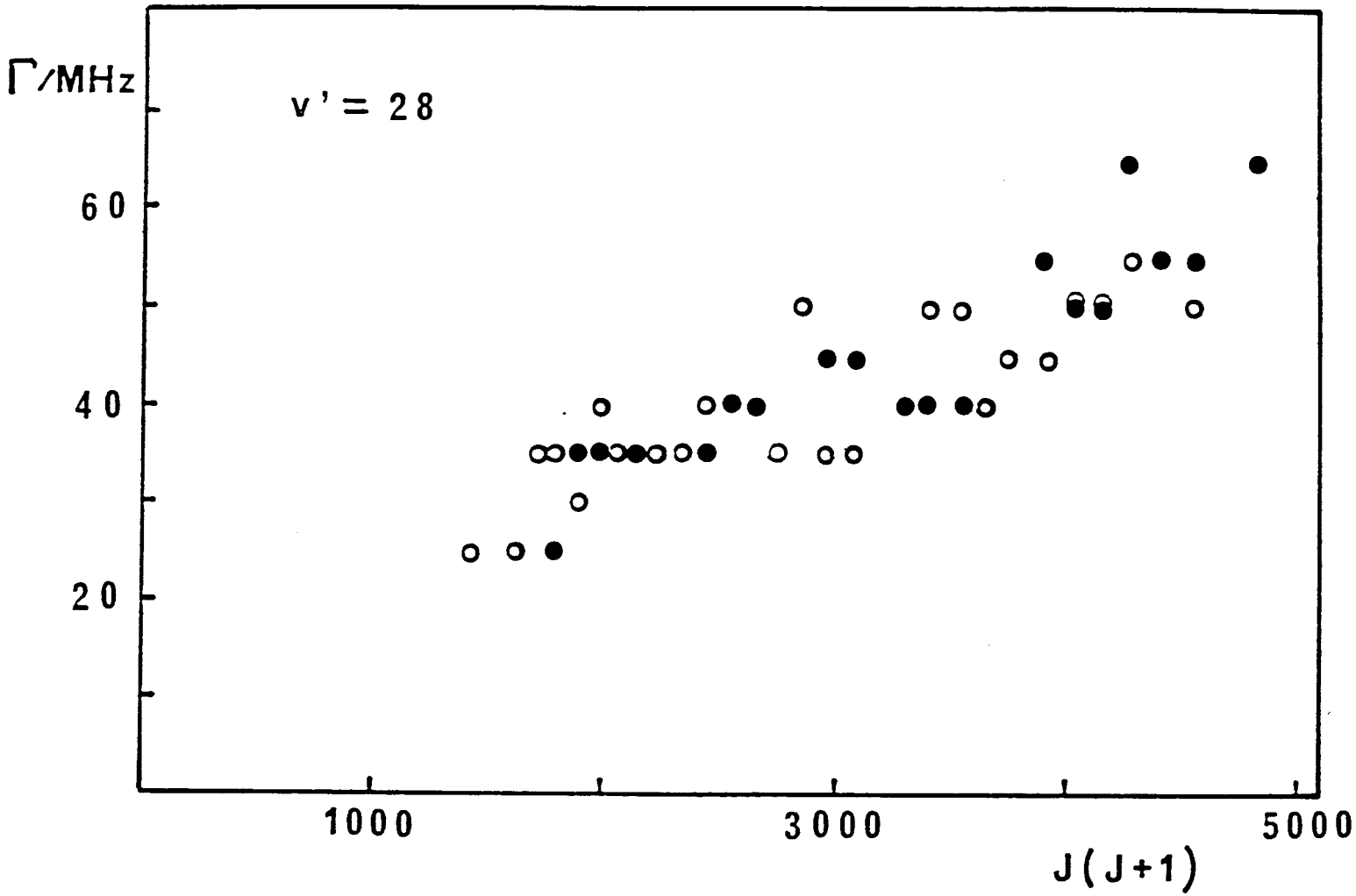

Fig. 31. The linewidth Γ of the $D^1\Sigma_u^+(v'=28, J) - X^1\Sigma_g^+(v''=2, J\pm1)$ transitions, plotted against J(J+1). An open circle (o) denotes the R branch and a filled circle (●) the P branch. The difference between the P and R branches is due to the experimental uncertainty.

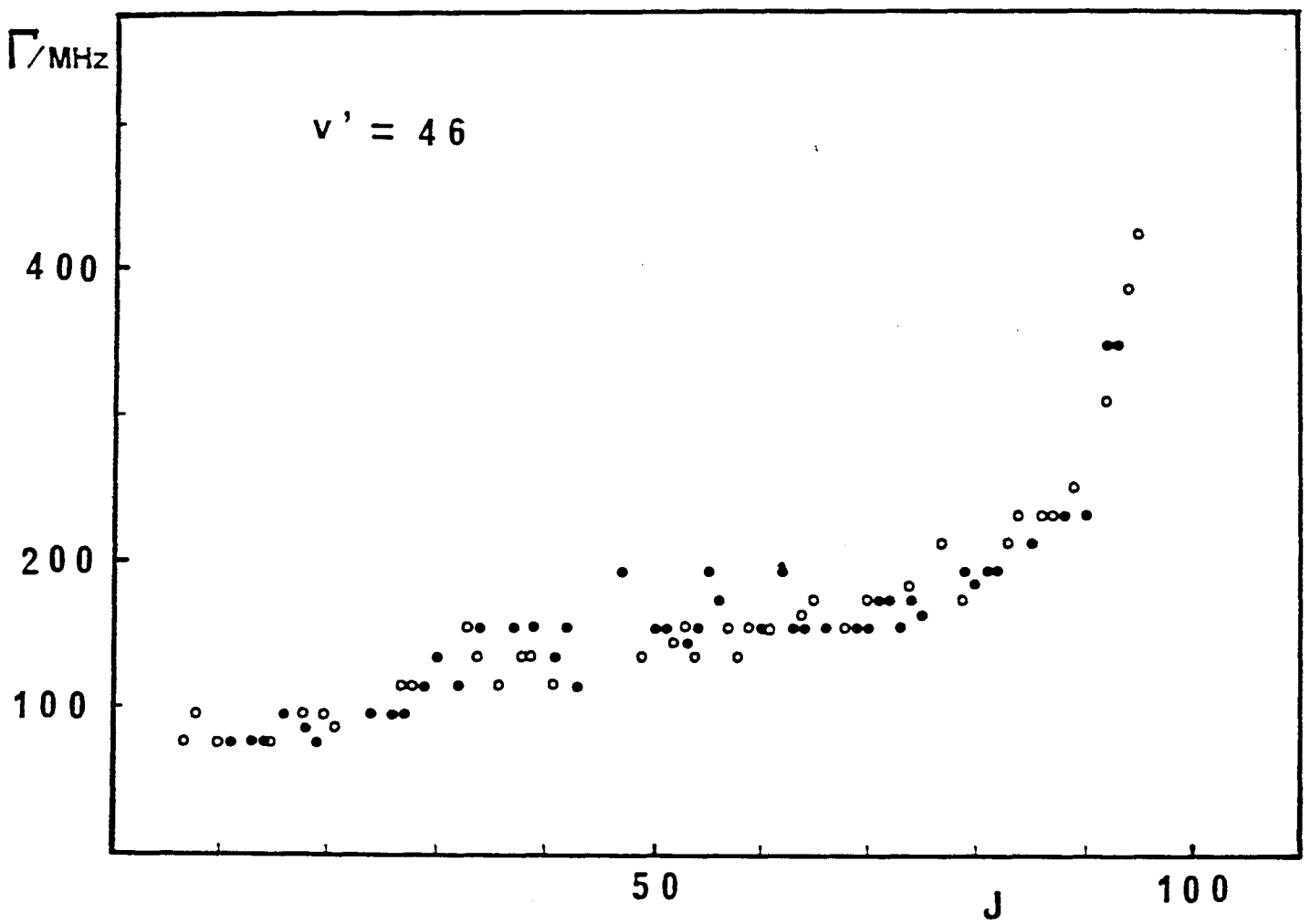

Fig. 32. J-dependence of the linewidth Γ of the $D^1\Sigma_u^+(v'=46, J)$ - $X^1\Sigma_g^+(v''=0, J\pm1)$ transitions. An open circle (o) denotes the P branch and a filled circle (●) the R branch. The difference between the P and R branches is due to the experimental uncertainty.

$$\tau = 1/(k_p + k_r). \qquad (5.9)$$

The increase of the linewidth represents the increase of the predissociation rate. The lifetimes of the $D^1\Sigma_u^+(v'=46,\ J'=30\sim70)$ levels are calculated to be about 1 ns from the observed Γ (Fig. 32) and Eq. (5.8). The radiative lifetime of the $D^1\Sigma_u^+$ state is about 35 ns.[60] Hence, the observed linewidth can be attributed to the predissociation rate; the predissociation rates k_p of the $D^1\Sigma_u^+(v'=46,\ J'=30\sim70)$ levels are $10^9\ s^{-1}$.

In the previous section, it is shown that the $D^1\Sigma_u^+(v',\ J)$ level is perturbed by the $(2)^3\Pi_u(v,\ Je)$ level. The $(2)^3\Pi_u$ state is expected to be bound. Hence, the perturbation with the $(2)^3\Pi_u$ state does not lead directly to predissociation. The most probable repulsive state, which leads to predissociation, is the $c^3\Sigma_u^+$ state.[58] However, there is no interaction between $^1\Sigma^+$ and $^3\Sigma^+$ in the first order approximation.[47] The perturbation between the $^3\Pi$ and $^3\Sigma^+$ states occurs through L-uncoupling interaction. [Eq. (4.9)] The nonvanishing matrix elements between the $^3\Pi_0(v,\ Je)$ and $^3\Sigma^+$ states are given by[47]

$$\langle ^3\Sigma^+(N=JJ)|H_{JL}|^3\Pi_0(v,\ Je)\rangle = [J(J+1)]^{1/2}2\eta, \qquad (5.10)$$

where η is a constant. Therefore, the predissociation of the $D^1\Sigma_u^+$ state occurs through a combination of the spin-orbit interaction between the $D^1\Sigma_u^+(v',\ J)$ and $^3\Pi_{0u}(v,\ Je)$ levels: $\langle ^1\Sigma_u^+(v',\ J)|H_{so}|^3\Pi_{0u}(v,\ Je)\rangle$; and the L-uncoupling interaction between the $^3\Pi_{0u}(v,\ Je)$ and $^3\Sigma_u^+(N=JJ)$ levels: $\langle ^3\Pi_{0u}(v,\ Je)|H_{JL}|^3\Sigma_u^+(N=JJ)\rangle$. From these results, the potential curve of the $c^3\Sigma_u^+$ state, which is repulsive and decomposes into the $Cs(6^2P_{3/2})$ and $Cs(6^2S_{1/2})$ atoms, is presumed to extend to the

inner wall of the $D^1\Sigma_u^+$ state potential curve and to cross near the $D^1\Sigma_u^+(v'=40)$, where the crossing with the $(2)^3\Pi_u$ state also occurs.

As we can see in Fig. 31, the linewidth Γ, hence the predissociation rate, of the $D^1\Sigma_u^+(v'=28)$ level increases proportionally to $J(J+1)$. This is in agreement with Eq. (5.11), which shows that L-uncoupling induces the predissociation and the rate is proportional to $J(J+1)$. This tendency is observed for $v'=25\sim30$. However, the J dependence of the linewidth Γ is found to change drastically at higher v' (>35) levels. An example is shown in Fig. 32. The linewidths Γ increase significantly at large J in the $D^1\Sigma_u^+(v'=46)$ level. This J dependence may originate from a change in the energy spacing or the Franck-Condon factors between the perturbing levels. More accurate molecular constants for the $(2)^3\Pi_u$ state are necessary for more detailed analysis. Generally, the linewidth is observed to increase with v'. This also indicates that the $D^1\Sigma_u^+$ state is more predissociative at high v' values.

ACKNOWLEDGEMENTS

The work reported in this thesis was done at the Kobe University from April 1990 until December 1992, under the direction of Professor *Hajime Katô*. I am specially grateful to *H. Katô* for his help and encouragement during the course of studies. His helpful suggestions and advice propelled forward this research work.

I would like to thank Professor *M. Baba* for helpful discussions and warmly encouragement and for his help about the early stage of this experiments. I would like to thank Mr. *K. Ishikawa* for helpful discussions about the experiments and analysis. I would like to thank Mr. *M. Chosa* and Mr. *K. Nishizawa* for their help about the early stage of this experiments. I would like to thank *H. Ikoma* for his help about the experiments and helpful discussions for analysis. I am very grateful to my fellows of graduate and undergraduate students in group for helpful discussions and warm assistance.

Finally, I would like to thank the Fellowship of the Japan Society for the Promotion of Science for Japanese Junior Scientists.

REFERENCE

[1]W. Demtröder, Laser Spectroscopy (Springer, Berlin, 1981).

[2]C. Wieman and T. W. Hänsch, Phys. Rev. Lett. 36, 1170 (1976).

[3]R. E. Teets, F. V. Kowalski, W. T. Hill, N. Carlson, and T. W. Hänsch, SPIE vol. 113 Laser Spectroscopy, p.80 (1977).

[4]M. Raab, G. Höning, W. Demtröder, and C. R. Vidal, J. Chem. Phys. 76, 4370 (1982).

[5]R. E. Teets, Ph. D. thesis, G. L. Report No. 2821, Stanford University (1978).

[6]M. S. Feld and A. Javan, Phys. Rev. 177, 540 (1969).

[7]T. W. Hänsch and P. Toschek, Z. Phys. 236, 213 (1970).

[8]Z. -G. Wang and H. -R. Xie, Molecular and laser spectroscopy (Springer, Berlin, 1991).

[9]N. W. Carlson, A. J. Taylar, K. M. Jones, and A. L. Schawlow, Phys. Rev. A24, 822 (1981).

[10]B. Hermmerling, R. Bombach, W. Demtröder, and N. Spies, Z. Phys. D5, 165 (1987).

[11]G. Herzberg, Molecular Spectra and Molecular Structure. I. Spectra of Diatomic Molecules (Van Nostrand Reinhold, 1950).

[12]R. S. Mulliken, Phys. Rev. 120, 1674 (1960).

[13]G. K. Chawla, H. J. Vedder, and R. W. Field, J. Chem. Phys. 86, 3082 (1987).

[14]J. Heinze and F. Engelke, J. Chem. Phys. 89, 42 (1988).

[15]R. F. Barrow, R. M. Clements, J. Derouard, N. Sadeghi, C. Effantin J. d'Incan, and A. J. Ross, Can. J. Phys. 65, 1154 (1987).

[16]H. Katô, M. Sakano, N. Yoshie, M. Baba, and K. Ishikawa, J. Chem. Phys. 93, 2228 (1990).

[17]A. J. Ross, C. Effantin, J. d'Incan, and R. F. Barrow, Mol. Phys. 56, 903 (1985).

[18]H. Lefebvre-Brion and R. W. Field, Perturbation in the Spectra of Diatomic Molecules (Academic, Orlando, 1986).

[19]J. L. Dunham, Phys. Rev. 41, 721 (1932).

[20]R. Rydberg, Z. Phys. 73, 376 (1931); O. Klein, ibid. 76, 226 (1932); A. L. G. Rees, Proc. Phys. Soc. London Ser. A59, 998 (1947).

[21]R. N. Zare, J. Chem. Phys. 40, 1934 (1964).

[22]J. M. Hutson, J. Phys. B14, 851 (1981).

[23]B. H. Wells, E. B. Smith, and R. N. Zare, Chem. Phys. Lett. 99, 244 (1983).

[24]R. J. LeRoy, J. Chem. Phys. 52, 2683 (1970).

[25]G. W. King and J. H. Van Vleck, Phys. Rev. 55, 1165 (1939).

[26]P. R. Fontana, Phys. Rev. 123, 1865, (1961), ibid, 123, 1871 (1961).

[27]A. Dalgarno and W. D. Davison, Mol. Phys. 13, 479 (1967).

[28]B. Bussery and M. Aubert-Frécon, J. Phys. B18, L379 (1985).

[29]R. Düren, W. Gröger, and R. Liedtke, Chem. Phys. Lett. 109, 424 (1984).

[30]L. Brencher, B. Nawracala, and H. Pauly, Z. Phys. D10, 211 (1988).

[31]R. J. LeRoy, Molecular Spectroscopy, Vol. 1. p.113 (The Chemical Society, London, 1973).

[32]W. C. Stwalley, Chem. Phys. Lett. 7, 600 (1970).

[33]R. J. LeRoy and R. B. Bernstein, J. Chem. Phys. 52, 3869 (1970).

[34]R. T. Birge and H. Sponer, Phys. Rev. 28, 259 (1926).

[35]W. J. Stevens, D. D. Konowalow, and L. B. Ratcliff, J. Chem. Phys. 80, 1215 (1984).

[36]M. Baba, T. Nakahori, T. Iida, and H. Katô, J. Chem. Phys. 93, 4637 (1990).

[37]R. A. Bernheim, L. P. Gold, and T. Tipton, J. Chem. Phys. 78, 3635 (1983).

[38]X. Xie, and R. W. Field, J. Mol. Spectros. 117, 228 (1986).

[39]S. Martin, J. Chevaleyre, M. C. Bordas, S. Valignat, M. Broyer, B. Cabaud, and A. Hoareau, J. Chem. Phys. 79, 4132 (1983).

[40]M. Broyer, J. Chevaleyre, G. delacretaz, S. Martin, and L. Wöste, Chem. Phys. Lett. 99, 206 (1983).

[41]G. Jong, H. Wang, C. -C. Tsai, W. C. Stwally, and A. M. Lyyra, J. Mol. Spectros. 154, 324 (1992).

[42]R. F. Barrow, R. M. Clements, G. Delacrétaz, C. Effantin, J. d'Incan, A. J. Ross, J. Vergès, and L. Wöste, J. Phys. B: At. Mol. Phys. 20, 3047 (1987).

[43]M. Bautista, and C. L. Ladera, J. Chem. Phys. 96, 5600 (1992).

[44]S. Leutwyler, M. Hofmann, H. P. Harri, and E. Schumacher, Chem. Phys. Lett. 77, 257 (1981).

[45]P. Cavaliere, G. Ferrante, and L. Lo Cascio, J. Chem. Phys. 62, 4753 (1975).

[46]L. Li and R. W. Field, J. Mol. Spectrosc. 117, 245 (1986).

[47]I. Kovács, Rotational Structure in the spectra of Diatomic Molecules (Adam Hilger, Bristol, 1969).

[48]B. Hermmerling, R. Bombach, and W. Demtröder, J. Phys. Chem. 87, 5186 (1987).

[49]F. W. Loomis and P. Kusch, Phys. Rev. 46, 292 (1934).

[50]R. P. Benedict, D. L. Drummond, and L. A. Schlie, J. Chem. Phys. 66, 4600 (1977).

[51]R. Gupta, W. Happer, J. Wagner, and E. Wennmyr, J. Chem. Phys. 68, 799 (1978).

[52]K. Yokoyama, M. Baba, and H. Katô, J. Chem. Phys. 89, 1209 (1988).

[53]C. B. Collins, J. A. Anderson, D. Popescu, and I. Popescu, J. Chem. Phys. 74, 1067 (1981).

[54]C. Amiot, W. Demtröder, and C. R. Vidal, J. Chem. Phys. 88, 5265 (1988).

[55]M. Baba, T. Nakahori, T. Iida, and H. Katô, J. Chem. Phys. 93, 4637 (1990).

[56]H. Weickenmeier, U. Diemer, M. Wahl, M. Raab, W. Demtröder, and W. Müller, J. Chem. Phys. 82, 5354 (1985).

[57]R. N. Zare, A. L. Schmeltekopf, W. J. Harrop, and D. L. Albritton, J. Mol. Spectrosc. 46, 37 (1973).

[58]H. Katô and K. Yoshihara, J. Chem. Phys. 71, 1585 (1979).

[59]L. Pauling and E. B. Wilson, Introduction to Quantum Mechanics (McGraw-Hill, New York, 1935).

[60]H. Katô, T. Kobayashi, Y. C. Wang, K. Ishikawa, M. Baba and S. Nagakura, Chem. Phys. 162, 107 (1992).

APPENDIX. THE OBSERVED ENERGY LEVELS OF HIGHLY EXCITED STATES OF THE $^{23}Na^{39}K$ MOLECULES

From the 2-step OODR polarization spectrum for the transitions to the highly excited states of the NaK molecule, many rotational levels of several $^1\Sigma^+$, $^1\Pi$, and $^1\Delta$ states could be observed and assigned (see Chapter 4). Here the transition energies of the transitions to highly excited levels from the pumped $B^1\Pi(v', J')$ levels and the term energies of the highly excited levels are listed.

(1): The observed lines where the $B^1\Pi(v'=9, J') \leftarrow X^1\Sigma^+$ $(v"=0, J")$ transition was chosen as the pump transition are listed in Table A1.

(2): The observed lines where the $B^1\Pi(v'=6, J') \leftarrow X^1\Sigma^+$ $(v"=0, J")$ transition was chosen as the pump transition are listed in Table A2.

(3): For the perturbed region of the $F^1\Delta(v=v_f+3)$ and $H^1\Sigma^+$ $(v=v_h+2)$ levels, the intermediate $B^1\Pi(v'=9, J'=1\sim60e$ and several $J'f)$ levels were chosen by the pump transition. In this case, observed lines are listed in Table A3.

(4): The unexpected levels could be observed through the perturbation with $H^1\Sigma^+$ $(v=v_h+2)$ levels, and these levels are listed in Table A4.

Table A1(a). Observed lines of the $^{23}Na^{39}K$ $F^1\Delta(v, J) \leftarrow B^1\Pi$ $(v'=9, J')$ transitions. The pump transition is fixed to one of the $B^1\Pi(v'=9, J') \leftarrow X^1\Sigma^+(v''=0, J'')$ rotational transition lines.

state	inter-mediate level (v', J')	probe transition energy (cm^{-1})	term energy (cm^{-1})	assignment (v, J)	
$F^1\Delta$	9, 40e	15320.0262	32982.1018	v_f,[b] 39e	
		15330.9534	32993.0290	41e	
	9, 30e	15396.1667	33016.7246	v_f+1, 29e	
		15400.3696	33020.9275	30f	(a)
		15404.3851	33024.9430	31e	
	9, 38e	15399.7886	33052.7820	v_f+1, 37e	
		15410.1321	33063.1255	39e	
	9, 38f	15400.0705	33052.8594	v_f+1, 37f	
		15405.1007	33057.8896	38e	
		15410.4086	33063.1975	39f	
	9, 40e	15401.0489	33063.1245	v_f+1, 39e	
		15406.4752	33068.5508	40f	(a)
		15411.9135	33073.9891	41e	
	9, 30e	15476.7978	33097.3557	v_f+2, 29e	
		15480.8013	33101.3592	30f	(a)
		15484.9675	33105.5254	31e	
	9, 30f	15476.7836	33097.3417	v_f+2, 29f	
		15480.8154	33101.3735	30e	
		15484.9515	33105.5096	31f	
	9, 37e	15479.6910	33128.2418	v_f+2, 36e	
		15489.6978	33138.2486	38e	
	9, 38e	15480.1878	33133.1812	v_f+2, 37e	
		15490.4563	33143.4497	39e	
	9, 40e	15481.3732	33143.4488	v_f+2, 39e	
		15492.1612	33154.2229	41e	

($F^1\Delta$)	9, 40f	15481.1485	33143.4285	v_f+2,	39f
		15486.4968	33148.7768		40e
		15491.9429	33154.2368		41f
	9, 41e	15481.6142	33148.7775	v_f+2,	40e
		15492.6581	33159.8214		42e
	9, 30e	15556.9709	33177.5288	v_f+3,[c]	29e
		15560.9829	33181.5408		30f (a)
		15565.0515	33185.6094		31e
	9, 40e	15561.4024	33223.4780	v_f+3,[c]	39e
		15566.6121	33228.6877		40f (a)
		15572.1289	33234.2045		41e
	9, 28e	15636.5535	33250.1396	v_f+4,	27e
		15640.2570	33253.8431		28f (a)
		15644.1051	33257.6912		29e
	9, 30e	15637.1318	33257.6897	v_f+4,	29e
		15641.1114	33261.6693		30f (a)
		15645.2078	33265.7657		31e
	9, 30f	15637.1323	33257.6904	v_f+4,	29f
		15641.1049	33261.6630		30e
		15645.2141	33265.7722		31f
	9, 32e	15637.7773	33265.7634	v_f+4,	31e
		15642.0305	33270.0166		32f (a)
		15646.3799	33274.3660		33e
	9, 34e	15638.4918	33274.3636	v_f+4,	33e
		15642.9672	33278.8390		34f (a)
		15647.5706	33283.4424		35e
	9, 36e	15639.2278	33283.4433	v_f+4,	35e
		15644.0207	33288.2362		36f (a)
		15648.8858	33293.1013		37e
	9, 38e	15640.1046	33293.0980	v_f+4,	37e
		15645.1409	33298.1343		38f (a)
		15650.2295	33303.2229		39e
	9, 38f	15640.3376	33293.1265	v_f+4,	37f
		15645.3252	33298.1141		38e
		15650.5028	33303.2917		39f
	9, 40e	15641.1505	33303.2261	v_f+4,	39e
		15646.5394	33308.6150		40f (a)
		15651.8569	33313.9325		41e

($F^1\Delta$)	9, 40f	15641.0077	33303.2877	v_f+4, 39f
		15646.2737	33308.5537	40e
		15651.6883	33313.9683	41f
	9, 41e	15641.3925	33308.5558	v_f+4, 40e
		15652.3692	33309.5325	42e
	9, 42e	15641.9237	33313.9294	v_f+4, 41e
		15653.1311	33325.1368	43e

(a) These Q lines are dispersion shaped signals.

(b) The lowest observed vibrational level v_f is approximately 20.

(c) These $F^1\Delta(v=v_f+3)$ levels are listed in Table A3(a).

Table A1(b). Observed lines of the $^{23}Na^{39}K$ $G^1\Delta(v, J) \leftarrow B^1\Pi$ ($v'=9$, J') transitions. The pump transition is fixed to one of the $B^1\Pi(v'=9, J') \leftarrow X^1\Sigma^+(v''=0, J'')$ rotational transition lines.

state	intermediate level (v', J')	probe transition energy (cm^{-1})	term energy (cm^{-1})	assignment (v, J)	
$G^1\Delta$	9, 38e	15353.0219	33006.0153	11, 37e	
		15358.0204	33011.0138	38f	(a)
		15363.4839	33016.4773	39e	
	9, 40e	15354.3990	33016.4746	11, 39e	
		15359.8279	33021.9035	40f	(a)
		15365.3731	33027.4487	41e	
	9, 30e	15436.0269	33056.5848	12, 29e	
		15440.0795	33060.6374	30f	(a)
		15444.2800	33064.8379	31e	
	9, 38e	15439.8170	33092.8104	12, 37e	
		15450.2028	33103.1962	39e	
	9, 38f	15440.0167	33092.8088	12, 37f	
		15445.1520	33097.9441	38e	
		15450.4070	33103.1991	39f	
	9, 40e	15441.1216	33103.1972	12, 39e	
		15446.5067	33108.5823	40f	(a)
		15452.0456	33114.1212	41e	
	9, 40f	15446.3074	33108.5874	12, 40e	
	9, 30e	15521.9609	33142.5188	13, 29e	
		15525.9760	33146.5339	30f	(a)
		15530.1486	33150.7065	31e	
	9, 37e	15534.9845	33183.5353	13, 38e	
	9, 38e	15525.4512	33178.4446	13, 37e	
		15535.7584	33188.7518	39e	
	9, 40e	15526.6802	33188.7558	13, 39e	
		15532.0187	33194.0943	40f	(a)
		15537.5135	33199.5891	41e	

($G^1\Delta$)	9, 40f	15526.4673	33188.7473	13, 39f	
		15531.8238	33194.1038	40e	
		15537.2977	33199.5777	41f	
	9, 41e	15538.0376	33205.2009	13, 42e	
	9, 30e	15606.3387	33226.8966	14, 29e	
		15610.3284	33230.8863	30f	(a)
		15614.4471	33235.0050	31e	
	9, 38e	15609.4793	33262.4727	14, 37e	
		15619.6815	33272.6749	39e	
	9, 40e	15610.6017	33272.6773	14, 39e	
		15621.3197	33283.3953	41e	
	9, 40f	15610.3823	33272.6623	14, 39f	
		15615.6916	33277.9716	40e	
		15621.3197	33283.3872	41f	
	9, 30e	15688.7112	33309.2691	15, 29e	
		15692.6520	33313.2099	30f	(a)
		15696.7221	33317.2800	31e	
	9, 30f	15688.7096	33309.2677	15, 29f	
		15692.6568	33313.2149	30e	
		15696.7208	33317.2789	31f	
	9, 32e	15689.2902	33317.2763	15, 31e	
		15697.8139	33325.8000	33e	
	9, 34e	15689.9210	33325.7981	15, 33e	
		15698.9597	33334.8368	35e	
	9, 36e	15690.6196	33334.8351	15, 35e	
		15700.1669	33344.3824	37e	
	9, 38e	15691.3864	33344.3798	15, 37e	
		15701.4361	33354.4295	39e	
	9, 40e	15692.3553	33354.4309	15, 39e	
		15697.5767	33359.6523	40f	(a)
		15702.9073	33364.9829	41e	
	9, 40f	15692.1578	33354.4378	15, 39f	
		15697.3624	33359.6424	40e	
		15702.7173	33364.9973	41f	
	9, 30e	15777.7552	33398.3131	16, 31e	

($G^1\Delta$)	9, 32e	15770.3246	33398.3107	16, 31e	
	9, 34e	15779.5713	33415.4484	16, 35e	
	9, 36e	15780.6161	33424.8316	16, 37e	
	9, 38e	15771.8364	33424.8298	16, 37e	
		15776.5870	33429.5804	38f	(a)
		15781.7531	33434.7465	39e	
	9, 39e	15772.1883	33429.7236	16, 38e	
		15777.0899	33434.6252	39f	(a)
		15782.3673	33439.9026	40e	
	9, 40e	15772.6717	33434.7473	16, 39e	
		15777.7209	33439.7965	40f	(a)
		15783.1063	33445.1819	41e	
	9, 40f	15772.3477	33434.6277	16, 39f	
		15777.6216	33439.9016	40e	
		15782.8299	33445.1099	41f	
	9, 41e	15772.7353	33439.8986	16, 40e	
		15777.9358	33445.0991	41f	(a)
		15783.4068	33450.5701	42e	
	9, 42e	15773.1725	33445.1782	16, 41e	
		15778.5207	33450.5264	42f	(a)
		15784.2402	33456.2459	43e	
	9, 30e	15847.1658	33467.7237	17, 29e	
		15855.0178	33475.5757	31e	
	9, 40e	15849.9798	33512.0554	17, 39e	
		15855.0973	33517.1729	40f	(a)
		15860.3548	33522.4304	41e	
	9, 30e	15923.5925	33544.1504	18, 29e	
		15931.3753	33551.9332	31e	
	9, 40e	15926.0052	33588.0808	18, 39e	
		15931.0761	33593.1517	40f	(a)
		15936.3016	33598.3772	41e	
	9, 40e	16000.7870	33662.8626	19, 39e	
		16010.8899	33672.9655	41e	

(a) These Q lines are dispersion shaped signals.

Table A1(c). Observed lines for the $^{23}Na^{39}K$ $^1\Sigma^+$, $^1\Pi$ and $^1\Delta$ transitions. The pump transition is fixed to one of the $B^1\Pi(v'=9, J') \leftarrow X^1\Sigma^+(v''=0, J'')$ rotational transition lines.

state	intermediate level (v', J')	probe transition energy (cm^{-1})	term energy (cm^{-1})	assignment (v, J)
$H^1\Sigma^+$	9, 30e	15386.8038	33007.3617	v_h , 29e
		15394.5389	33015.0968	31e
	9, 38e	15388.4837	33041.4771	v_h , 37e
		15398.3805	33051.3739	39e
	9, 40e	15389.2935	33051.3691	v_h , 39e
		15399.5013	33061.5769	41e
	9, 30e	15558.1979	33178.7558	v_h+2,[c] 29e
		15565.8527	33186.4106	31e
	9, 40e	15559.8475	33221.9231	v_h+2,[c] 39e
		15569.9117	33231.9873	41e
	9, 28e	15639.9047	33253.4908	v_h+3, 27e
		15647.1825	33260.7686	29e
	9, 30e	15640.1825	33260.7657	v_h+3, 29e
		15647.9608	33268.5187	31e
	9, 30f	15644.0263	33264.5844	v_h+3, 30e
	9, 32e	15640.5293	33268.5154	v_h+3, 31e
		15648.7219	33276.7080	33e
	9, 34e	15640.8344	33276.7062	v_h+3, 33e
		15649.4001	33285.2719	35e
	9, 36e	15641.0578	33285.2733	v_h+3, 35e
		15649.9521	33294.1676	37e
	9, 38e	15641.1762	33294.1696	v_h+3, 37e
		15650.4895	33303.4829	39e
	9, 40e	15641.4077	33303.4833	v_h+3, 39e

$I^1\Sigma^+$	9, 30e	15481.0344	33101.5923	v_i , 29e
		15489.0684	33109.6263	31e
	9, 30f	15484.9871	33105.5452	v_i , 30e
	9, 37e	15483.4499	33132.0007	v_i , 36e
		15492.9867	33141.5375	38e
	9, 38e	15483.9096	33136.9030	v_i , 37e
		15493.6409	33146.6343	39e
	9, 40e	15484.5558	33146.6314	v_i , 39e
		15495.0942	33157.1698	41e
	9, 40f	15489.5657	33151.8457	v_i , 40e
	9, 41e	15484.6790	33151.8423	v_i , 40e
		15495.4453	33162.6086	42e
	9, 30e	15563.6967	33184.2546	$v_i+1;^{(d)}$ 29e
		15571.7411	33192.2990	31e
	9, 40e	15567.7349	33229.8105	$v_i+1;^{(d)}$ 39e
		15578.4063	33240.4819	41e
$J^1\Sigma^+$	9, 30e	15597.7239	33218.2818	v_j , 29e
		15605.8230	33226.3809	31e
	9, 38e	15600.4029	33253.3963	v_j , 37e
		15610.6010	33263.5944	39e
	9, 40e	15601.5173	33263.5929	v_j , 39e
		15612.1987	33274.2743	41e
	9, 40f	15606.5733	33268.8533	v_j , 40e
	9, 30e	15768.7685	33389.3264	v_j+2, 29e
		15776.7628	33397.3207	31e
	9, 32e	15769.3313	33397.3174	v_j+2, 31e
		15777.7626	33405.7487	33e
	9, 36e	15770.0312	33414.2467	v_j+2, 35e
	9, 38e	15770.3285	33423.3219	v_j+2, 37e
		15779.93	33432.92	39e
	9, 39e	15770.5301	33428.0654	v_j+2, 38e

($J^1\Sigma^+$)	9, 40e	15770.8344	33432.9100	v_j+2, 39e
		15780.8704	33442.9460	41e
	9, 40f	15775.5850	33437.8650	v_j+2, 40e
	9, 41e	15770.7051	33437.8684	v_j+2, 40e
	9, 42e	15770.9360	33442.9417	v_j+2, 41e
$R_1{}^1\Delta$	9, 30e	15543.9256	33164.4835	v_1 , 29e
		15551.7733	33172.3312	31e
	9, 32e	15544.3473	33172.3334	v_1 , 31e
		15552.7209	33180.7070	33e
	9, 34e	15544.8316	33180.7034	v_1 , 33e
		15553.7122	33189.5840	35e
	9, 34f	15544.4864	33180.3628	v_1 , 33f
		15549.2058	33185.0822	34e
		15553.3451	33189.2215	35f
	9, 36e	15545.3466	33189.5869	v_1 , 35e
		15554.7551	33198.9707	37e
	9, 38e	15545.9771	33198.9705	v_1 , 37e
		15555.8597	33208.8532	39e
	9, 40e	15546.7779	33208.8535	v_1 , 39e
		15557.1574	33219.2330	41e
	9, 40f	15551.6966	33213.9766	v_1 , 40e
$R_2{}^1\Pi$	9, 28e	15579.2424	33192.8285	v_2 , 27e
		15586.7259	33200.3120	29e
	9, 30e	15579.7503	33200.3082	v_2 , 29e
		15587.7737	33208.3316	31e
	9, 32e	15580.3447	33208.3308	v_2 , 31e
		15588.8727	33216.8588	33e
	9, 34e	15580.9888	33216.8606	v_2 , 33e
		15590.0328	33225.9046	35e
	9, 34f	15580.6951	33216.5715	v_2 , 33f
		15589.6793	33225.5557	35f
	9, 36e	15581.6857	33225.9013	v_2 , 35e
		15591.2550	33235.4706	37e

	9, 38e	15582.4752	33235.4686	v_2 , 37e
		15592.5624	33245.5558	39e
	9, 40e	15583.4816	33245.5572	v_2 , 39e
		15594.0844	33256.1600	41e
$R_3{}^1\Pi$	9, 30e	15717.4594	33338.0173	v_3 , 29e
		15725.3958	33345.9537	31e
	9, 30f	15717.4695	33338.0276	v_3 , 29f
		15725.4096	33345.9677	31f
	9, 32e	15717.9662	33345.9523	v_3 , 31e
		15726.3915	33354.3776	33e
	9, 34e	15718.5028	33354.3799	v_3 , 33e
		15727.4754	33363.3525	35e
	9, 36e	15719.1395	33363.3550	v_3 , 35e
		15728.6068	33372.8223	37e
	9, 38e	15719.8331	33372.8265	v_3 , 37e
		15729.8327	33382.8261	39e
	9, 40e	15720.7526	33382.8282	v_3 , 39e
		15731.1776	33393.2532	41e
	9, 40f	15720.5407	33382.8207	v_3 , 39f
		15730.9705	33393.2505	41f

(c) These $H^1\Sigma^+(v=v_f+2)$ levels are listed in Table A3(b).

(d) These $I^1\Sigma^+(v=v_i+1)$ levels are listed in Table A3(c).

Table A2(a). Observed lines of the $^{23}Na^{39}K$ $K^1\Delta(v, J) \leftarrow B^1\Pi$ $(v'=6, J')$ transitions. The pump transition is fixed to one of the $B^1\Pi(v'=6, J') \leftarrow X^1\Sigma^+(v''=0, J'')$ rotational transition lines.

state	inter-mediate level (v', J')	probe transition energy (cm^{-1})	term energy (cm^{-1})	assignment (v, J)	
$K^1\Delta$	6, 18e	17110.4020	34539.4784	v_k,[b] 17e	
		17115.4562	34544.5326	19e	
	6, 18f	17112.8557	34541.9321	v_k , 18e	
	6, 20e	17110.4775	34544.5313	v_k , 19e	
		17112.9533	34547.0071	20f	(a)
		17116.0726	34550.1264	21e	
	6, 22e	17110.6014	34550.1350	v_k , 21e	
		17116.7348	34556.2684	23e	
	6, 18e	17195.6087	34624.6851	v_k+1, 17e	
		17200.6288	34629.7052	19e	
	6, 18f	17198.0466	34627.1230	v_k+1, 18e	
	6, 20e	17195.6530	34629.7068	v_k+1, 19e	
		17198.3631	34632.4169	20f	(a)
		17201.2132	34635.2670	21e	
	6, 22e	17195.7354	34635.2690	v_k+1, 21e	
		17198.7201	34638.2537	22f	(a)
		17201.8360	34641.3696	23e	
	6, 18e	17280.1620	34709.2384	v_k+2, 17e	
		17282.5956	34711.6720	18f	(a)
		17285.1563	34714.2327	19e	

(a) These Q lines are dispersion shaped signals.

(b) v_k is the lowest observed vibrational level.

Table A2(b). Observed lines for the $^{23}Na^{39}K$ $^1\Sigma^+$, $^1\Pi$ and $^1\Delta$ states. The pump transition is fixed to one of the $B^1\Pi(v'=6, J') \leftarrow X^1\Sigma^+(v''=0, J'')$ rotational transition lines.

state	intermediate level (v', J')	probe transition energy (cm^{-1})	term energy (cm^{-1})	assignment (v, J)
$R_4{}^1\Sigma^+$	6, 18e	17100.9243	34530.0007	v_4 , 17e
		17105.6834	34534.7598	19e
	6, 18f	17103.2408	34532.3172	v_4 , 18e
	6, 20e	17100.7061	34534.7599	v_4 , 19e
		17105.9886	34540.0424	21e
	6, 22e	17100.5114	34540.0450	v_4 , 21e
		17106.3228	34545.8564	23e
$R_5{}^1\Pi$	6, 18e	17120.6353	34549.7117	v_5 , 17e
		17125.5405	34554.6169	19e
	6, 20e	17120.5629	34554.6167	v_5 , 19e
		17126.0098	34560.0636	21e
	6, 22e	17120.5292	34560.0628	v_5 , 21e
		17126.4873	34566.0209	23e
$R_6{}^1\Delta$	6, 18e	17183.4491	34612.5255	v_6 , 17e
		17188.3066	34617.3830	19e
	6, 18f	17185.7898	34614.8662	v_6 , 18f
	6, 20e	17183.3336	34617.3874	v_6 , 19e
		17188.7802	34622.8340	21e
	6, 22e	17183.3056	34622.8392	v_6 , 21e
		17186.2270	34625.7606	22f (a)
		17189.2884	34628.8220	23e

(a) This Q line is dispersion shaped signals.

Table A3(a). Observed lines of the $^{23}Na^{39}K$ $F^1\Delta(v=v_f+3, J) \leftarrow B^1\Pi(v'=9, J')$ transitions. The pump transition is fixed to one of the $B^1\Pi(v'=9, J') \leftarrow X^1\Sigma^+(v''=0, J'')$ rotational transition lines.

	intermediate level (v', J')	probe transition energy (cm^{-1})	term energy (cm^{-1})	assignment (J)
($F^1\Delta$)	9, 1e	15554.4037	33119.8471	2e
	9, 2e	15554.5679	33120.2491	3e
	9, 3e	15554.7484	33120.7864	4e
	9, 6e	15553.6351	33121.4601	5e
		15555.3760	33123.2006	7e
	9, 7e	15553.6043	33122.2627	6e
		15555.6113	33124.2697	8e
	9, 10e	15553.6009	33125.4766	9e
		15556.4102	33128.2859	11e
	9, 11e	15553.6277	33126.8115	10e
		15556.7061	33129.8899	12e
	9, 14e	15553.7964	33131.6290	13e
		15555.6680	33133.5006	14f (a)
		15557.6761	33135.5087	15e
	9, 15e	15553.8815	33133.5038	14e
		15555.8826	33135.5049	15f (a)
		15558.0281	33137.6504	16e
	9, 18e	15554.2282	33139.9231	17e
		15556.6262	33142.3211	18f (a)
		15559.1707	33144.8656	19e
	9, 19e	15554.3679	33142.3267	18e
		15556.9041	33144.8629	19f (a)
		15559.5820	33147.5408	20e
	9, 20e	15554.5297	33144.8673	19e
		15557.1983	33147.5359	20f (a)
		15560.0018	33150.3394	21e
	9, 21e	15554.7053	33147.5402	20e
		15557.5088	33150.3437	21f (a)
		15560.4438	33153.2787	22e

($F^1\Delta$)	9, 22e	15554.8958	33150.3429	21e
		15557.8243	33153.2714	22f (a)
		15560.9015	33156.3486	23e
	9, 23e	15555.1008	33153.2814	22e
		15558.1652	33156.3458	23f (a)
		15561.3680	33159.5486	24e
	9, 24e	15555.3202	33156.3480	23e
		15558.5244	33159.5522	24f (a)
		15561.8560	33162.8838	25e
	9, 25e	15555.5561	33159.5487	24e
		15558.8968	33161.8894	25f (a)
		15562.3496	33166.3422	26e
	9, 26e	15555.8089	33162.8827	25e
		15559.2752	33166.3490	26f (a)
		15562.8595	33169.9333	27e
	9, 27e	15556.0722	33166.3409	26e
		15559.6822	33169.9509	27f (a)
		15563.4453	33173.7140	28e
	9, 28e	15556.3475	33169.9336	27e
		15560.0976	33173.6837	28f (a)
		15563.9459	33177.5320	29e
	9, 29e	15556.6980	33173.7110	28e
		15560.5307	33177.5437	29f (a)
		15564.4965	33181.5095	30e
	9, 29f	15556.6663	33173.6816	28f
		15560.5171	33177.5320	29e
		15564.5273	33181.5426	30f
	9, 30e	15556.9709	33177.5288	29e
		15560.9829	33181.5408	30f (a)
		15565.0515	33185.6094	31e
	9, 31e	15557.2920	33181.5063	30e
		15561.4512	33185.6655	31f (a)
		15565.6244	33189.8387	32e
	9, 32e	15557.6216	33185.6077	31e
		15561.9420	33189.9281	32f (a)
		15566.1592	33194.1453	33e
	9, 33e	15557.9635	33189.8414	32e
		15562.4331	33194.3110	33f (a)
	9, 33f	15558.0486	33189.9272	32f
		15566.9513	33198.8299	34f

($F^1\Delta$)	9, 34e	15558.2713	33194.1431	33e
		15562.9546	33198.8264	34f (a)
		15567.7660	33203.6378	35e
	9, 34f	15558.4351	33194.3115	33f
		15563.1812	33199.0576	34e
		15567.6063	33203.4827	35f
	9, 35e	15563.4881	33203.4777	35f (a)
		15568.3700	33208.3596	36e
	9, 36e	15564.0457	33208.2613	36f (a)
		15569.0723	33213.2879	37e
	9, 37e	15559.8100	33208.3608	36e
		15564.6161	33213.1669	37f (a)
		15569.7683	33218.3191	38e
	9, 38e	15560.2955	33213.2889	37e
		15565.2203	33218.2137	38f (a)
		15570.4829	33223.4763	39e
	9, 39e	15560.7823	33218.3176	38e
		15565.8512	33223.3865	39f (a)
		15571.2402	33228.7755	40e
	9, 40e	15561.4024	33223.4780	39e
		15566.6121	33228.6877	40f (a)
		15572.1289	33234.2045	41e
	9, 40f	15561.1040	33223.3840	39f
		15566.4996	33228.7796	40e
		15571.8423	33234.1223	41f
	9, 41e	15572.5999	33239.7632	42e
	9, 42e	15562.2005	33234.2062	41e
		15573.4491	22245.4548	43e
	9, 42f	15567.8680	33239.7591	42e
		15573.4749	33245.3660	43f
	9, 43e	15562.7629	33239.7618	42e
	9, 43f	15562.6243	33239.6771	42f
		15568.3984	33245.4512	43e
		15574.1389	33251.1917	44f
	9, 44e	15563.3412	33245.4512	43e
		15575.1023	33257.2123	45e
	9, 44f	15563.2379	33245.3653	43f
		15569.1369	33251.2643	44e
		15575.0129	33257.1403	45f

($F^1\Delta$)	9, 45e	15563.9282	33251.2627	44e
		15575.9528	33263.2873	46e
	9, 46e	15564.5416	33257.2129	45e
		15576.8173	33269.4886	47e
	9, 47e	15565.1729	33263.2852	46e
		15577.7083	33275.8206	48e
	9, 47f	15565.0997	33263.2162	46f
		15571.3726	33269.4891	47e
		15577.6361	33275.8169	48f
	9, 48f	15565.7533	33269.4209	47f
		15572.1493	33275.8169	48e
		15578.5607	33282.2283	49f
	9, 49e	15566.4979	33275.8182	48e
	9, 51f	15567.8465	33288.8105	50f
		15574.6462	33295.6102	51e
		15581.3998	33302.3638	52f

(a) These Q lines are dispersed signals.

Table A3(b). Observed lines of the $^{23}Na^{39}K$ $H^1\Sigma^+(v=v_h+2, J) \leftarrow B^1\Pi(v'=9, J')$ transitions. The pump transition is fixed to one of the $B^1\Pi(v'=9, J') \leftarrow X^1\Sigma^+(v''=0, J'')$ rotational transition lines.

	intermediate level (v', J')	probe transition energy (cm^{-1})	term energy (cm^{-1})	assignment (J)
($H^1\Sigma^+$)	9, 2e	15558.1273	33123.8085	1e
		15558.7253	33124.4065	3e
	9, 3e	15558.0087	33124.0467	2e
		15558.8561	33124.8941	4e
	9, 6e	15557.6838	33125.5088	5e
		15559.2806	33127.1056	7e
	9, 7e	15557.5835	33126.2419	6e
		15559.4356	33128.0940	8e
	9, 10e	15557.3369	33129.2126	9e
		15559.9735	33131.8492	11e
	9, 11e	15557.2895	33130.4733	10e
		15560.1628	33133.3466	12e
	9, 14e	15557.1370	33134.9696	13e
		15560.7826	33138.6152	15e
	9, 15e	15557.0966	33136.7189	14e
		15561.0071	33140.6294	16e
	9, 18e	15557.0655	33142.7604	17e
		15561.7191	33147.4140	19e
	9, 19e	15557.0685	33145.0273	18e
		15561.9667	33149.9255	20e
	9, 20e	15557.0759	33147.4135	19e
		15562.2152	33152.5528	21e
	9, 21e	15557.0887	33149.9236	20e
		15562.4548	33155.2897	22e
	9, 22e	15557.1019	33152.5490	21e
		15562.6889	33158.1360	23e
	9, 22f	15559.8392	33155.2904	22e

($H^1\Sigma^+$)	9, 23e	15557.1067	33155.2873	22e
		15562.8974	33161.0780	24e
	9, 24e	15557.1086	33158.1364	23e
		15564.1966	33165.2244	25e
	9, 25e	15557.0857	33161.0786	24e
		15564.3613	33168.3539	26e
	9, 26e	15558.1507	33165.2245	25e
		15564.5883	33171.6621	27e
	9, 27e	15558.0825	33168.3512	26e
		15564.8591	33175.1278	28e
	9, 28e	15558.0744	33171.6605	27e
		15565.1694	33178.7555	29e
	9, 29e	15558.1142	33175.1272	28e
		15565.5008	33182.5135	30e
	9, 29f	15561.7376	33178.7529	29e
	9, 30e	15558.1979	33178.7558	29e
		15565.8527	33186.4106	31e
	9, 31e	15558.2958	33182.5101	30e
		15566.2458	33190.4601	32e
	9, 32e	15558.4219	33186.4080	31e
	9, 33e	15558.5800	33190.4579	32e
		15566.6458	33198.5237	34e
	9, 33f	15562.7839	33194.6625	33e
	9, 34e	15558.7882	33194.6653	33e
		15567.0921	33202.9692	35e
	9, 34f	15562.6455	33198.5219	34e
	9, 35e	15558.5338	33198.5234	34e
		15567.5011	33207.4929	36e
	9, 36e	15558.7534	33202.9689	35e
		15567.8905	33212.1060	37e
	9, 37e	15558.9403	33207.4911	36e
		15568.1893	33216.7401	38e
	9, 38e	15559.1112	33212.1046	37e
		15568.9306	33221.9240	39e
	9, 39e	15559.2040	33216.7393	38e
		15569.3407	33226.8760	40e

($H^1\Sigma^+$)	9, 40e	15559.8475	33221.9231	39e
		15569.9117	33231.9873	41e
	9, 40f	15564.5946	33226.8746	40e
	9, 41e	15559.7098	33226.8731	40e
		15570.0532	33237.2165	42e
	9, 42e	15559.9777	33231.9834	41e
		15570.5723	33242.5779	43e (s)
		15570.5857	33242.5914	43e (s)
	9, 43e	15560.2154	33237.2143	42e
		15570.9240	33247.9229	44e
	9, 44e	15560.4699	33242.5799	43e (s)
		15560.4852	33242.5952	43e (s)
		15571.4169	33253.5269	45e
	9, 45e	15560.5866	33247.9211	44e
		15571.8607	33259.1952	46e
	9, 46e	15560.8593	33253.5306	45e
		15572.5762	33265.2475	47e
	9, 47e	15561.0823	33259.1946	46e
		15573.0527	33271.1650	48e
	9, 48e	15561.5815	33265.2455	47e
		15573.5803	33277.2443	49e
	9, 49e	15561.8463	33271.1666	48e
		15574.1501	33283.4704	50e
	9, 50e	15562.1610	33277.2471	49e
		15574.8691	33289.9552	51e
	9, 51e	15562.5083	33283.4658	50e
		15575.1354	33296.0949	52e
	9, 52e	15563.0166	33289.9517	51e
		15575.7928	33302.7279	53e
	9, 53e	15563.0735	33296.0899	52e
		15576.3675	33309.3839	54e
	9, 54e	15563.5202	33302.7242	53e
		15577.0408	33316.2448	55e
	9, 55e	15563.8882	33309.3818	54e
		15577.7984	33323.2920	56e
	9, 55f	15570.7442	33316.2411	55e

($H^1\Sigma^+$)	9, 56e	15564.3534	33316.2408	55e
		15578.5577	33330.4451	57e
	9, 57e	15564.9061	33323.2886	56e
		15579.4186	33337.8011	58e
	9, 58e	15565.4663	33330.4418	57e
		15580.4596	33345.4351	59e
	9, 59e	15566.1290	33337.7982	58e
		15581.6255	33353.2947	60e
	9, 59f	15573.7313	33345.4341	59e
	9, 60e	15566.9910	33345.4313	59e

(s) These lines are split into two lines. This splitting may be originating from the perturbation.

Table A3(c). Observed lines of the $^{23}Na^{39}K$ $I^1\Sigma^+(v=v_i+1, J) \leftarrow B^1\Pi(v'=9, J')$ transitions. The pump transition is fixed to one of the $B^1\Pi(v'=9, J') \leftarrow X^1\Sigma^+(v''=0, J'')$ rotational transition lines.

	intermediate level (v', J')	probe transition energy (cm^{-1})	term energy (cm^{-1})	assignment (J)
($I^1\Sigma^+$)	9, 18e	15562.0221	33147.7170	17e
	9, 19e	15562.0453	33150.0041	18e
	9, 20e	15562.0862	33152.4238	19e
	9, 21e	15562.1352	33154.9701	20e
	9, 22e	15562.2151	33157.6622	21e
	9, 23e	15562.3054	33160.4860	22e
	9, 24e	15562.4246	33163.4524	23e
	9, 25e	15562.5339	33166.5265	24e
	9, 26e	15562.7706	33169.8444	25e
	9, 28e	15563.1781	33176.7642	27e
		15570.6749	33184.2610	29e
	9, 29e	15563.4249	33180.4379	28e
	9, 30e	15563.7026	33184.2605	29e
		15571.7411	33192.2990	31e
	9, 32e	15564.3094	33192.2955	31e
		15572.9069	33200.8930	33e
	9, 34e	15565.0220	33200.8938	33e
		15574.1275	33209.9993	35e
	9, 34f	15569.5528	33205.4292	34e
	9, 36e	15565.7851	33210.0007	35e
		15575.4529	33219.6685	37e
	9, 38e	15566.6713	33219.6647	37e
		15576.8165	33229.8099	39e
	9, 39e	15567.1361	33224.6714	38e

($I^1\Sigma^+$)	9, 40e	15567.7349	33229.8105	39e
		15578.4063	33240.4819	41e
	9, 41e	15567.9531	33235.1164	40e
	9, 42e	15568.4749	33240.4806	41e
	9, 43e	15569.0076	33246.0065	42e
	9, 44e	15569.5512	33251.6612	43e
	9, 45e	15570.1036	33257.4381	44e
	9, 46e	15570.6791	33263.3504	45e
	9, 47e	15571.2656	33269.3779	46e

Table A4(a). Observed lines of the $^{23}Na^{39}K$ U(v, J) ← $B^1\Pi$ (v'=9, J') transitions. The pump transition is fixed to one of the $B^1\Pi$(v'=9, J') ← $X^1\Sigma^+$(v"=0, J") rotational transition lines.

	inter-mediate level (v', J')	probe transition energy (cm^{-1})	term energy (cm^{-1})	assign-ment (J)
(U)	9, 18e	15560.2393	33145.9342	17e
		15564.2795	33149.9744	19e
	9, 19e	15559.9559	33147.9147	18e
		15564.1939	33152.1527	20e
	9, 20e	15559.6386	33149.9762	19e
		15564.1270	33154.4646	21e
	9, 21e	15559.3175	33152.1524	20e
		15564.0822	33156.9171	22e
	9, 22e	15559.0135	33154.4606	21e
		15564.0653	33159.5124	23e
	9, 22f	15561.4622	33156.9134	22e
	9, 23e	15558.7366	33156.9172	22e
		15564.1007	33162.2813	24e
	9, 24e	15558.4873	33159.5151	23e
		15563.0779	33164.1057	25e
	9, 25e	15558.2857	33162.2783	24e
		15563.1992	33167.1918	26e
	9, 26e	15557.0354	33164.1092	25e
		15563.2959	33170.3697	27e
	9, 27e	15556.9229	33167.1916	26e
		15563.3104	33173.5791	28e
	9, 28e	15556.7806	33170.3667	27e
		15563.4100	33176.9961	29e
	9, 29e	15556.5627	33173.5757	28e
		15563.4749	33180.4879	30e
	9, 29f	15559.9814	33176.9967	29e

(U)	9, 30e	15556.4364	33176.9943	29e
		15563.5488	33184.1067	31e
	9, 31e	15556.2731	33180.4874	30e

Table A4(b). Observed lines of the $^{23}Na^{39}K$ T(v, J) ← $B^1\Pi$ (v'=9, J') transitions. The pump transition is fixed to one of the $B^1\Pi$(v'=9, J') ← $X^1\Sigma^+$(v"=0, J") rotational transition lines.

	inter-mediate level (v', J')	probe transition energy (cm^{-1})	term energy (cm^{-1})	assign-ment (J)
(T)	9, 36e	15568.4750	33212.6906	37e
	9, 37e	15568.4540	33217.0048	38e
	9, 38e	15559.6976	33212.6910	37e
		15568.5860	33221.5794	39e
	9, 39e	15559.4680	33217.0033	38e
		15569.0167	33226.5520	40e
	9, 40e	15559.5024	33221.5780	39e
		15569.6304	33221.7060	41e
	9, 41e	15559.3863	33226.5496	40e
		15569.8280	33236.9913	42e
	9, 42e	15559.6991	33231.7048	41e
		15570.3966	33242.4023	43e
	9, 43e	15559.9886	33236.9875	42e
		15571.1013	33248.1002	44e
	9, 44e	15560.2937	33242.4037	43e
		15571.6769	33253.7869	45e
	9, 45e	15560.7650	33248.0995	44e
		15572.3059	33259.6404	46e
	9, 46e	15561.1171	33253.7884	45e
	9, 47e	15561.5313	33259.6436	46e